Experimental and Numerical Studies of Mode I and Mode II Delamination of Polymer Composites with Embedded Optical Sensors

THÈSE N^{O} 5054 (2011)

PRÉSENTÉE LE 10 JUIN 2011

À LA FACULTÉ SCIENCES ET TECHNIQUES DE L'INGÉNIEUR
LABORATOIRE DE MÉCANIQUE APPLIQUÉE ET D'ANALYSE DE FIABILITÉ
PROGRAMME DOCTORAL EN SCIENCE ET GÉNIE DES MATÉRIAUX

ÉCOLE POLYTECHNIQUE FÉDÉRALE DE LAUSANNE

POUR L'OBTENTION DU GRADE DE DOCTEUR ÈS SCIENCES

PAR

Samuel STUTZ

acceptée sur proposition du jury:

Prof. C. Hébert, présidente du jury
Prof. I. Botsis, directeur de thèse
Prof. A. Benallal, rapporteur
Dr P.-E. Bourban, rapporteur
Dr A. Brunner, rapporteur

ÉCOLE POLYTECHNIQUE
FÉDÉRALE DE LAUSANNE

Suisse
2011

Acknowledgements

First of all I thank Prof. John Botsis for giving me the opportunity to carry out my thesis under his supervision. He guided my work during the past four years, was very available for discussions, and an invaluable help in writing scientific articles. He was also the applicant for the Swiss National Science Foundation grant (No 200020-124397) under which my thesis was carried out.

I am also grateful to my colleagues in the LMAF - Marco Lai with whom I shared the office, Dr. Jeannot Frieden, Milad Maleki, Dr. Matteo Galli, Prof. Thomas Gmür, Marco Piccinini, and our secretary Viviane Mangnenat. A special thank goes to Dr. Joël Cugnoni, for any problem I encountered he had an idea how it could be solved. Thank you all for the great time we had together with interesting scientific (and other) discussions, relaxing coffee breaks, and intense problem solving, you made my working place a nice place to be.

I want to thank Dr. Dragan Coric who helped me with optics related questions, and the LTC laboratory for letting me use some of their equipment and material. I am also very grateful to Marc Jeanneret, Nicolas Favre, and Stéphane Haldner from the machine shop. With their incredible skills they provided me with the best possible moulds grips and perfectly cut samples.

During my thesis I had the chance to supervise student projects which was a very good and enriching experience and I would like to thank Giulia Benvenuti and Alexandra Duron that they have chosen to work with me for their projects.

Among all the people I have met and with which I have shared happy moments during the past four years I thank particularly Dominique Zosso and Anja Kunze for all the lunch breaks and Philipp Kobel for many good times at concerts and in Satellite.

Before or after long office and laboratory hours I often had the chance to enjoy the beauty of the lake together with my rowing partners. Thank you all, especially Julien for getting up so early every week.

My parents have always supported me and I am extremely fortunate that they stood behind me during all these many years of studying - thank you so much. And finally, I thank my fiancèe Stéphanie for all her love and for sharing her life with me. This work is dedicated to you.

Abstract

Over the past decades the use of composite materials has enormously increased, especially in the aeronautical, automotive, and energy production industries. These materials allow to build lighter and larger structures which are more efficient. However, by introducing composite materials into load bearing structures, new modes of failure have to be understood to further improve design and guarantee the safety during the whole life time of such parts.

Since composite materials are often produced in layered structures, they are prone to delamination where a crack propagates between the layers. The mechanical tests which are used today to measure the fracture properties cannot account for all processes associated with delamination. Namely, intact fibres that link the fracture surfaces, so called bridging fibres, can strongly influence the outcome of such tests, however, they cannot be quantitatively measured.

In this work, a semi-experimental method was developed and used to study delamination tests and identify the contribution of bridging to toughness. For this, the strain distribution around the crack tip was measured with embedded optical sensors, so called fibre Bragg gratings (FBG). A new methodology based on multiplexed FBGs was developed and allowed to acquire a quasi-continuous strain distribution at relatively high rates. The results were then used in an inverse identification method to determine parameters which characterise delamination and bridging.

Mode I delamination was studied with the double cantilever beam test in monotonic and fatigue loading. Using the above mentioned method the closing tractions due to bridging fibres were identified and their contribution to the resistance against crack propagation was determined. Compared to the monotonic loading, the contribution of bridging in fatigue was found to be about 30%

higher. With a cohesive zone finite element model which was accounting for the bridging tractions, the onset and propagation of the delamination were correctly predicted. The bridging was found to contribute by 50% to the total energy release rate (ERR).

In a similar way mode II delamination was studied with a four point end notched flexure test and the ERR as well as friction coefficients were identified using the measured strain distribution. While bridging was found negligible, the ERR in mode II was three times higher than the initiation value of mode I delamination.

Finally, in a mixed mode bending test the modes I and II were combined so that each one was contributing by 50% to the delamination. The initiation value was found to be about 15% higher than the one of mode I, although with a large scatter, while the propagation value was only marginally higher. The fibre bridging, which formed during the delamination, was characterised from the changes of strain measured with the embedded optical sensors.

The proposed method of strain measurements with embedded optical sensors and inverse identification offers an interesting alternative to existing methods used to characterise delamination. It was successfully used to identify fibre bridging without assumptions on the length of the bridging zone and opens a new way to study micromechanics of fracture in laminated materials.

Keywords: Delamination, fibre bridging, fibre Bragg grating sensors, cohesive zone elements.

Résumé

Ces dernières décennies, on a pu assister à une forte croissance de l'utilisation des matériaux composites, surtout dans le secteur aéronautique, des automobiles et de la production d'énergie. De par leurs propriétés exceptionnelles, ces matériaux permettent de réaliser des structures bien plus larges et plus légères et donc souvent plus efficaces que celles que l'on a pu réaliser auparavant. Avec l'utilisation des composites dans les structures portantes, l'étude de nouveaux modes de rupture est nécessaire pour garantir la sécurité pendant toute la durée de vie des pièces. Vu qu'ils sont souvent produits sous la forme de stratifiés les composites sont facilement sujet à délamination, où une fissure se propage entre deux couches. Actuellement, on utilise plusieurs tests mécaniques pour mesurer les propriétés de ce mode de rupture. Par contre, ces tests ne peuvent pas, en général, tenir compte des phénomènes micromécaniques comme le pontage de fibres intactes, qui pourtant influencent les résultats.

Dans ce travail, une méthode semi-expérimentale a été développée et utilisée pour étudier les différents tests de délamination et notamment le rle que joue le pontage de fibres dans la résistance à la rupture. Ainsi, les fibres optiques contenant des réseaux de Bragg ont été utilisées pour mesurer la distribution des déformations dans la direction des fibres de renfort. Le développement d'une nouvelle méthode utilisant des réseaux de Bragg multiplexes a conduit à mesurer des déformations quasi distribuées à des vitesses d'acquisition relativement élevées. Ces résultats ont ensuite été utilisés dans une méthode d'identification inverse pour déterminer les paramètres caractérisant la délamination et le pontage de fibres.

La délamination en mode I sous chargement continu et en fatigue a été étudiée au travers d'un test standard DCB (double cantilever beam). Grâce à la nou-

velle méthode décrite plus haut, la distribution des tractions due au pontage de fibres a été identifiée et leur contribution à la résistance à la rupture déterminée. Comparée au chargement continu, cette contribution était de 30% supérieure au cas d'un chargement en fatigue. La relation entre la traction des fibres de pontage et l'ouverture de la fissure ainsi déterminée a été intégrée dans un modèle d'éléments finit cohésifs où ces derniers simulent l'endommagement du composite. Avec ce modèle numérique l'initiation et la propagation de la délamination ont pu être simulées correctement. Le pontage de fibres contribue jusqu'à 50% de la résistance à la rupture dans le matériau étudié.

D'une manière similaire, la délamination en mode II a été étudiée avec le test 4ENF (four point end notched flexure) qui est dérivé d'une flexion quatre points avec un échantillon contenant une délamination. La résistance à la rupture et les coefficients de friction ont pu être identifiés en utilisant les déformations mesurées avec les réseaux de Bragg et une identification inverse. Par contre aucun signe apparent de la présence du pontage de fibres n'a pu être observé. La résistance à la rupture en mode II ainsi trouvée était trois fois supérieure à celle de la délamination en mode I. Enfin, les modes de delamination I et II ont été combinés avec une mixité de 50% dans le test standard MMB (mixed mode bending). La résistance à la rupture au début de la propagation était de 15% plus élevée qu'en mode I pur mais avec une large dispersion des résultats. La valeur stable de propagation était par contre très similaire à celle du mode I. De plus, le pontage de fibres a été caractérisé à partir des mesures avec les réseaux de Bragg.

En conclusion, la méthode proposée ici utilise les réseaux de Bragg multiplexes pour mesurer la déformation dans un composite et une identification inverse pour déterminer les paramètres clés des tests de délamination. Elle offre ainsi une alternative intéressante aux méthodes existantes pour étudier la micromécanique de la rupture dans les matériaux composites.

Mots-clés: Délamination, pontage de fibres, réseau de Bragg, éléments cohésifs

Contents

List of Tables **xiii**

List of Figures **xv**

List of Symbols **xix**

List of Abbreviations **xxi**

1 Introduction **1**

1.1 Motivation 1

1.2 Objectives 3

1.3 Structure of the Thesis 5

2 State of the art **7**

2.1 Delamination in composites 7

2.1.1 Bridging 8

2.1.2 Delamination tests 9

2.2 Optical strain sensors 10

2.2.1 Embedded sensors 11

2.2.2 OLCR based method 11

2.2.3 Multiplexd FBGs 12

2.3 Summary 12

3 Materials and methods **15**

3.1 Manufacturing, material and testing 15

3.1.1 Specimens and test set-up 18

3.1.2 Crack length measurements . . . 19
3.1.3 Testing machines . . . 21
3.2 Optical measurements . . . 21
3.2.1 OLCR measurements . . . 24
3.2.2 Multiplexed FBG sensors . . . 26
3.3 Numerical methods . . . 30
3.3.1 Inverse identification . . . 31
3.3.2 Cohesive element models . . . 33
3.4 Calculation of the energy release rate . . . 34
3.4.1 Compliance methods . . . 36
3.4.2 Crack with bridging . . . 36
3.4.3 Area method . . . 37
3.5 Summary . . . 38

4 Crack - Sensor interaction **41**
4.1 Sub-model . . . 41
4.2 Energy release rate along the crack front . . . 43
4.3 Strain in the glass fibre . . . 45
4.4 Summary . . . 46

5 Mode I delamination **47**
5.1 Test set-up . . . 47
5.1.1 Monotonic loading . . . 48
5.1.2 Fatigue loading . . . 49
5.2 Mechanical test results . . . 50
5.2.1 Monotonic loading . . . 50
5.2.2 Fatigue loading . . . 52
5.3 Strain measurements . . . 54
5.3.1 OLCR based measurements . . . 55
5.3.2 Multiplexed sensors . . . 57
5.4 Numerical modelling . . . 59
5.4.1 Identification of bridging tractions . . . 59
5.4.2 Model for bridging distribution . . . 61
5.4.3 Bridging law . . . 64

5.4.4 Cohesive element simulation 66
5.4.5 Stress intensity factor 69
5.5 Calculation of the energy release rate 71

6 Mode II delamination **75**
6.1 Test set-up 75
6.2 Mechanical test results 77
6.3 Strain measurements 79
6.3.1 OLCR based measurements 79
6.3.2 Multiplexed sensors 80
6.4 Numerical modelling 82
6.4.1 Identification 83
6.4.2 Friction 86

7 Mixed mode I and II delamination **91**
7.1 Test set-up 91
7.2 Mechanical test results 94
7.3 Energy release rate 94
7.4 Strain measurements 96
7.5 Numerical modelling 98
7.5.1 Identification of bridging 99

8 Conclusions **103**
8.1 Optical fibre sensors 103
8.2 Delamination 105
8.3 Future work 107

Bibliography **109**

List of Tables

3.1 Material properties used for simulations. 18
3.2 Pre-crack length for the different delamination tests. 19

5.1 Energy release rate of the bridging fibres. 65
5.2 Identified bridging traction distributions. 66

LIST OF TABLES

List of Figures

1.1 Possible delamination sites. 2
1.2 The three modes of fracture. 3
1.3 Fracture and fibre bridging zone. 4

3.1 Curing cycle of the composite. 16
3.2 A schematic of the lay up of composite manufacturing. 17
3.3 Micrograph with embedded fibre sensor. 17
3.4 Graduation on the side of a delaminated sample. 18
3.5 Fitting of crack length data. 20
3.6 Working principle of an FBG. 22
3.7 Schematic of the OLCR set-up. 25
3.8 Reflection spectrum of an FBG array. 27
3.9 Measured strain during crack propagation. 28
3.10 Wavelength vs. time of a sensor array in mode I. 29
3.11 Shifted strain curves of a mode I delamination. 30
3.12 Flowchart of the inverse identification. 31
3.13 Typical traction separation curves for cohesive elements. 33
3.14 Illustration of the area method 38

4.1 Sub-model with fibre. 42
4.2 Mesh with glass fibre 43
4.3 Energy release rate along the crack front. 44
4.4 Strain in the composite around the fibre. 46

5.1 Schematic of a DCB test set-up 48
5.2 Bridging fibres in a DCB test. 48

5.3 Load decrease in displacement controlled fatigue. 50
5.4 Load-displacement curves in mode I. 51
5.5 Load displacements hysteresis at around 77'000 cycles. 52
5.6 Evolution of crack length during the fatigue test. 53
5.7 Crack speed and ERR in fatigue DCB tests. 54
5.8 OLCR-Measurements in mode I. 55
5.9 OLCR measurements with coinciding crack. 56
5.10 Evolution of strain with increasing crack length. 58
5.11 Strain distribution measured with the FBG sensors. 59
5.12 Model used to identify the bridging tractions. 60
5.13 Measured and optimised strain distributions in mode I. 61
5.14 Convergence of the different bridging models. 62
5.15 Bridging traction distribution 63
5.16 Bridging laws. 65
5.17 Cohesive law in mode I. 67
5.18 Simulated and experimental load displacement curves. 68
5.19 Evolution of the ERR with growing crack length. 71
5.20 ERR with and without bridging as a function of crack length. . . 74

6.1 Schematic of the 4ENF set-up. 76
6.2 Photograph of the 4ENF set-up. 76
6.3 Load displacement curves of 4ENF tests. 78
6.4 Measured strain distribution in mode II delamination. 80
6.5 Evolution of strain during the 4ENF test. 81
6.6 Strain distribution around the crack in a 4ENF test. 82
6.7 Schematic of the numerical model of the 4ENF test. 84
6.8 Measured and simulated strain in a 4ENF test. 85
6.9 Convergence of the optimisation in mode II. 85
6.10 Experimental and simulated load-displacement in 4ENF tests. . . 86
6.11 Simulated load displacement curves for different frictions. 88
6.12 Strain distribution with different applied frictions. 89

7.1 Schematic of the set-up of an MMB test. 92
7.2 Photograph of the MMB test. 93

7.3 Load displacement curves from the MMB tests. 95
7.4 Evolution of the ERR for 50% mode mixture 96
7.5 Strain versus crack length for an MMB test. 97
7.6 Strain distribution measured in the MMB test. 98
7.7 Schematic of the numerical model of the MMB test. 99
7.8 Convergence of the bridging identification in the MMB test. . . . 100
7.9 Measured and simulated strain distribution in MMB test. 101

LIST OF FIGURES

List of Symbols

A	Crack surface
B	Width of the sample
C	Compliance
E	Young's modului in i direction
F	Error vector
G	Shear modulus or energy release rate
K	Stress intensity factor
P	Applied load
U	Strain energy
a	Crack length
a_0	Initial crack length
h	Height of the composite plate
n	Refractive index
Λ	Period of the index change in an FBG
Π	Potential energy
Ψ	Total energy
δ	Displacement/separation of fracture surfaces
ε	Strain
λ_B	Bragg wavelength
$\Delta\lambda_B$	Shift of the Bragg wavelength
ν	Poisson's ratio
σ	Stress

LIST OF SYMBOLS

List of Abbreviations

4ENF	Four point end notched flexure test/specimen type
CC	Compliance calibration
COD	Crack opening displacement
DCB	Double cantilever beam test/specimen type
ERR	Energy release rate
FBG	Fibre Bragg grating
FE	Finite element
FRP	Fibre reinforced polymer
LBW	Local Bragg wavelength
MBT	Modified beam theory
MMB	Mixed mode bending test/specimen type
OLCR	Optical low-coherence reflectometry
PTFE	Poly-tetra-flour-etyhlen
RP	Reference point
SIF	Stress intensity factor
UD	Uni-directional (composite)
WDM	Wavelength-division-multiplexing

LIST OF ABBREVIATIONS

Chapter 1

Introduction

1.1 Motivation

In the past decades, the use of fibre reinforced polymers (FRP), in the following also called composites, has dramatically increased. In sport goods they replaced wood or aluminium. In civil engineering patches of FRP are used to repair damaged concrete structures. Modern wind turbines with their huge blades could simply not be built without composites. And the automotive and aerospace industries try to replace more and more metal parts by composite structures to reduce weight, assembly costs, increase efficiency and reduce maintenance. As an example of these developments, one can consider the newest generation of wide-bodied aircrafts which consists of 50% in weight of composite materials.

The success of composite materials is due to their extraordinary properties and the flexibility in manufacturing. They have a very high specific stiffness and strength which means that they can be designed as stiff and strong as steel but with a five times lower density. The properties can be tailored to meet structural, manufacturing, and cost requirements. The versatility is obtained by combining different types of fibres like carbon, glass, or natural fibres with suitable resins such as epoxy, polyester, or polypropylene and by adding fillers. With the correct choice of constituents, composite parts can also be very resistant to corrosion or transparent to radar signals. Further, the anisotropic properties can help reducing weight by optimised design and allow for innovative solutions by elastic coupling of twist and bending.

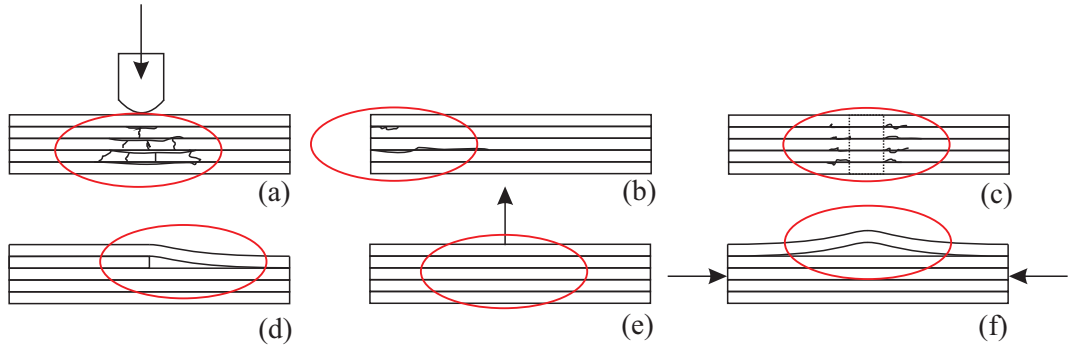

Figure 1.1: Possible delamination sites: (a) after an impact, (b) at a free edge, (c) around a drilled hole or a bolt, (d) at ply drops, (e) at places with out-of-plane loads, (f) under buckling.

Composites can be produced in many different ways [1]. For large series injection moulding, extrusion, or hot press methods with expensive tooling can be used. Mostly manual procedures like resin transfer moulding or hand lay-up allow to produce complicated shapes with cheap moulds which is very interesting for prototypes or small series. For example the manufacturing of the fuselage of a small aircraft or the hull of a sailing boat is possible in one shot which reduces considerably the assembly cost and weight.

The increasing use of composite materials in load bearing structures creates a strong need to understand and quantify damage since their fracture properties must be known to correctly design a part. Because most composite parts are relatively thin layered structures where the reinforcing fibres are oriented in pre-defined directions in the same plane, they are prone to delamination, i.e. cracks that propagate between two of the constitutive layers and separate the laminate into thinner sub-laminates. This inter-laminar fracture leads to an important decrease of stiffness and usually failure of the structure. Figure 1.1 shows typical causes and locations of delaminations [2].

There are three independent modes of fracture as illustrated in Figure 1.2. The opening of the crack (mode I), the in-plane horizontal shearing (mode II), and the out-of-plane tearing (mode III). The stress field around the crack tip is different for each mode and thus also the resistance of the material against crack propagation. Therefore, the fracture properties have to be tested for each mode

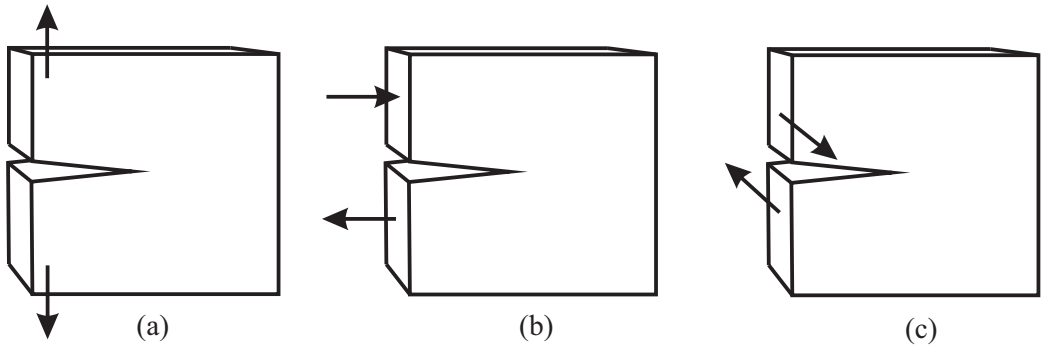

Figure 1.2: Modes of fracture: (a) opening, mode I, (b) shearing, mode II, (c) tearing, mode III

separately as well as for combinations of them.

Delamination tests are performed with unidiretional (UD) samples despite the fact that delamination usually occurs between layers with dissimilar orientation. However, the crack has to be propagated between two zero degree planes because otherwise the sample would have an asymmetric layup causing twist, or, in the case of 90 degree layers, the crack would leave the crack plane. Nesting of fibres which occurs in UD composite, creates a zone with fibre bridging in the wake of the crack while the fracture of the composite is concentrated at the crack tip as shown in Figure 1.3.

Fibre bridging clearly is an artefact of the test and is undesired since it increases the measured resistance of the composite. Therefore, initiation values are usually taken to determine the fracture properties since fibre bridging develops only upon crack propagation and is not present at the initiation. However, these values can be influenced by the way the initial crack was produced. For these reasons a clear understanding of the effects of fibre bridging is desirable, so that propagation values can be used.

1.2 Objectives

In 2006 a special issue of the journal *Composite Science and Technology* appeared following a workshop with the title: *The development of robust design/modelling tools for predicting delamination damage and failure in composite structures.* The

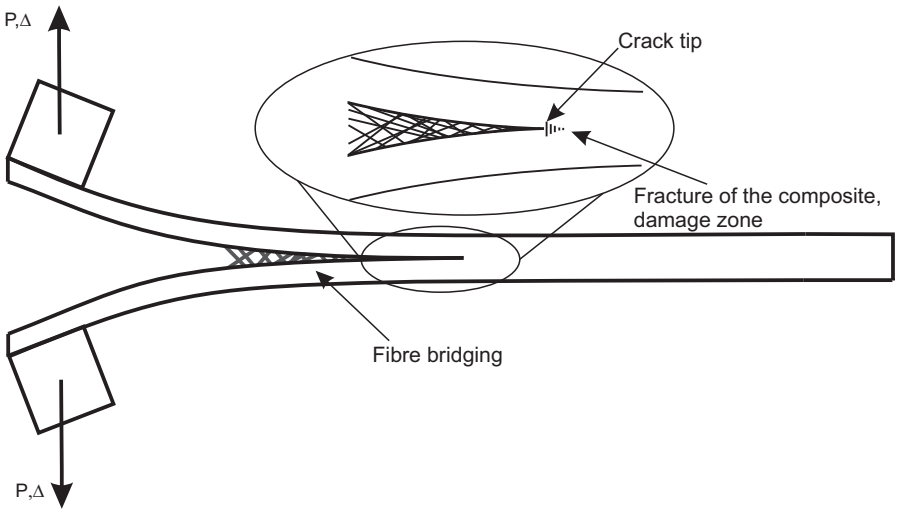

Figure 1.3: The schematic of a mode I delamination test shows zone of the fracture of the composite which is limited to the crack tip and the fibre bridging zone.

workshop was held three years earlier in Cachan, France. In the introduction, a list of current and possible future advances in modelling of delamination in composite materials was presented. For future work, among others the following points were mentioned:

- Built-in sensors to monitor delamination cracks.
- Develop test methods for microscale parameters to support micromechanics models.
- Apply inverse modelling methods and optimisation to determine model parameters from tests.

This work is a contribution to these objectives. It is also a direct continuation of the work of Larissa Sorensen [3–5] where embedded optical fibre sensors, so called fibre Bragg gratings (FBG), were used to detect a delamination crack tip and to measure the strain distribution around it. The measurements were performed in the thermoplastic material AS4/PPS and the results were used to characterise the fibre bridging. The methodology has proven well suited, however, a very specialised equipment was required for the strain measurements and a complete

measurement took several minutes. In the present work, the aim was to measure strains in another material and additional test geometries. Further, a simpler and faster interrogation method for the optical sensors should be developed so that strains can be measured in fatigue tests.

The objectives of this thesis can be summarised in the following points:

- Embed fibre sensors in a carbon fibre reinforced epoxy composite and use them to measure the strain distribution around the delamination crack tip with an optical low-coherence reflectometry (OLCR) based method.
- Analyse the interaction of the fibre sensor with the crack tip with numerical models to verify the applicability of this sensor.
- Identify the fibre bridging traction distribution and compare the results when different analytical expressions are used to describe this distribution.
- Develop a methodology based on multiplexed FBGs to simplify and speed-up the strain measurements.
- Measure the strain in mode I, mode I fatigue, mode II, and mixed mode I/II tests with the new method based on multiplexed FBGs and identify the characteristic parameters for each test from the obtained strain distributions.
- Create a cohesive finite element model which accounts for these findings to predict onset and propagation of the delamination.

1.3 Structure of the Thesis

This thesis is organised thematically. In chapter 2 the available literature in the domains of delamination of composites, fibre bridging and fibre optical strain sensors are summarised according to the best of the author's knowledge.

Chapter 3 first describes the materials and manufacturing techniques that were used to produce the specimens. Then, the optical methods are presented. The focus lies here on the method for strain measurements with the multiplexed

FBG sensor which was developed in this work. It is illustrated with measurements of mode I delamination. Further, the inverse identification method and the cohesive finite elements are described.

Since the embedded fibre sensors constitute an inclusion in the composite, their interaction with the host material and the strain field of the crack was investigated. The results of this analysis are shown in Chapter 4.

In Chapter 5 the results obtained in mode I delamination are shown. Two interrogation systems for fibre sensors were compared in this test configuration, one based on optical low-coherence reflectometry and the other on the multiplexing capability of the FBG sensors. From the obtained strain distributions the fibre bridging law was identified. The stress intensity factor and the contribution of the bridging fibres to the energy release rate were then calculated with these results. Further, the results of fatigue tests are reported.

Chapters 6 and 7 present the results from the mode II tests and the mixed mode I/II tests with a mode mixture of 50%. The measurements from the fibre sensor were similarly treated as in mode I.

Chapter 2

State of the art

Delamination is a very common type of damage in composite materials and a lot of research has been devoted to understand and predict it. The first section of this chapter resumes the literature in the domain of delamination of composites in mode I, mode II, mixed mode I/II, and fatigue as well as fibre bridging. The second section reviews how optical fibre sensors have been used as sensors in composites materials.

2.1 Delamination in composites

The literature on delamination has been reviewed several times [2, 6, 7] and an excellent textbook was recently edited by Sridharan [8] which is entirely devoted to the delamination behaviour of composites. Some authors concentrated their work on the mechanical aspects of delamination [9, 10] while others focussed more on practical issues like methods to estimate damage produced by hole drilling [11] or ways to improve the design of wind turbine blades to resist delamination [12]. A fractographic analysis showed the difference between the different delamination modes [13] and recent advances in high resolution tomography allowed to study damage in notched tensile tested composite specimens showing delamination cracks [14].

Beside the experimental study of delamination, finite element modelling becomes increasingly important. While the virtual crack closure technique [15, 16]

is often used to calculate the strain energy release rate, the onset and propagation of delamination in composite materials is mostly simulated with cohesive zone finite elements [17, 18]. Such elements are placed in the path of the delamination and can be damaged which allows the crack to propagate. The work required to completely damage the cohesive elements is defined by the traction separation curve called *cohesive law*. The shape of this law was found to have a strong influences on the delamination behaviour [19–21]. Beside the simulation of quasi-static delamination tests [22, 23] cohesive elements have also been used to simulate dynamic delamination [24] and high cycle fatigue delamination [25]. A comprehensive summary of the simulation of delamination with cohesive elements is given in the recent textbook of Turon et al. [26]. Since cohesive elements have to be placed in advance at the interfaces some alternative methods are currently under consideration [27].

2.1.1 Bridging

When inspecting delamination specimens, intact fibres that cross the delamination crack from one surface to the other can often be observe. This phenomenon is called *fibre bridging*. Possible causes for fibre bridging are nesting of fibres between adjacent plies during manufacturing or the change of crack plane which might be due to porosity or other defects [28]. If the bridging zone is sufficiently small the delamination can be analysed by fracture mechanics [29]. However, this is usually not the case in FRPs where large scale bridging occurs.

Experimentally it was shown that a small difference of the angle between the plies next to the crack plane can drastically decrease the bridging [28]. However, for standard delamination tests with unidirectional composites fibre bridging has to be characterised. The length of the bridging zone is strongly influenced by the geometry of the specimen [30, 31]. Therefore traction separation relations are preferred where the traction at each point depends on the opening of the crack. Such a bridging law corresponds to an array of non-linear springs which are continuously distributed on the crack surfaces [30, 32].

To determine the bridging law, several authors measured simultaneously the energy release rate (ERR) and crack opening displacement (COD). The derivation

of the ERR with respect to COD results directly in the bridging law [30, 33–36]. Considering bridging fibres as small beams, traction separation curves were derived from micromechanical models [31, 34, 37]. However, many assumptions are required for such models. Alternatively, bridging laws were identified from strains measured in the bridging zone with embedded sensors [3, 4]. Usually, cohesive elements were used to simulate delamination with the determined bridging laws. However, such models do not have a sharp crack tip. A mix between brittle and cohesive fracture as implemented in the so called material point method [38] might be more realistic.

Since fibre bridging increases the crack resistance of a composite material, researchers have aimed to introduce it artificially by introducing fibres that are positioned in the out of plane direction, so called z-pinning [39–41]. A traction separation model based on fibre pull out test and spacing of the z-pins was found in good agreement with experiments [42].

2.1.2 Delamination tests

The current status of delamination testing has recently been reviewed by Brunner et al. [43]. For mode I delamination the double cantilever beam test (DCB) [44, 45] is recognised as standard test method and is widely used. Exact solutions for the stress intensity factor for isotropic materials [46] as well as approximate weight functions for orthotropic material properties [47] are available. Currently a standard method for a mode I fatigue test based on the DCB set-up is under consideration [48].

Beside its purpose to measure quantitatively the ERR in mode I delamination of UD composites, the DCB test was also used to compare, for example, the effect of different fibre sizings [49] and added particles [50] on the fracture toughness of composite materials.

Some work has been done on angle ply delamination [51]. In such tests fibre bridging which depended on the orientation of the plies was observed. However, as a consequence of the non-symmetric layup, the crack front was not straight [52].

The mixed mode bending test [53] is the standard method to determine the energy release rate under mixed mode conditions with different mixtures of mode I&II. However, a recent study has shown that for very high modulus composites this test can no longer be used [54]. MMB test were used to measure mixed mode delamination in fatigue [55], to quantify the effect of moisture [56], and with an angle between the delamination planes [57, 58]. A comparison between mixed mode delamination in complex structures and in MMB test showed the usefulness of this test [59].

In the case of mode II delamination different set-ups like the end load split (ELS) the end notched flexure (ENF) or the four point end notched flexure (4ENF) were proposed [2, 60, 61]. However, there is still no agreement on which one should be used as a standard. Some authors even question if a pure mode II test can be realised [62] and if it is useful for design. Two main difficulties are faced in all test, namely, the correct determination of the crack tip [63, 64] and friction [65]. The ENF is often preferred because it yields lower values for the ERR which are closer to FEM solutions [66, 67], however, the 4ENF test has the advantage of stable crack propagation [61].

2.2 Optical strain sensors

The photo-sensitivity of optical fibres was discovered by Ken Hill in 1978 [68] while looking for a way to filter wavelength-division-multiplexing (WDM) signals in telecommunication. The light of a single-mode argon-ion laser was reflected at the end of a photo-sensitive fibre creating a standing wave pattern which interacted with the glass to form a periodic change of refractive index in the core of the fibre forming a *fibre Bragg grating* (FBG). Such an FBG reflects light of a certain wavelength while all other wavelengths remain unaffected. The real break through came with the discovery of Meltz et al. [69] who found a way to write any desired pattern of gratings from the outside of the fibre using a phase mask.

Soon it was recognized that FBGs are not only useful in telecommunication, but can also serve as sensors since the reflected wavelength depends on temperature and strain. FBG sensors were used to study the curing of a thermoset matrix [70, 71], to measure thermal expansion coefficients [72], to detect impact

damage [73] or monitor structures [74]. Detailed descriptions of FBG sensors can be found in the review article of Kersey [75] and in the textbooks of Kashyap [76] and Measures [77].

2.2.1 Embedded sensors

When optical fibre sensors are embedded in composite structure they form an inclusion that may be the cause of damage initiation. Experiments have shown that in certain configurations the presence of optical fibres can degrade the fatigue performance of the host material [78–80]. The influence of optical fibres on other mechanical properties were reviewed by Kuang and Cantwell [81] and found only marginal if the fibres were smaller than the ply thickness and placed in the direction of the reinforcing fibres. To further decrease the the risk of negative effects from embedded fibres some researchers reduced its diameter [82–84].

A study of the interface between an uncoated optical fibre and an epoxy matrix [85, 86] has shown no indications of debonding of the interface. However, the presence of a coated fibre influences locally the strain field in a composite [87] up to a distance of about one fibre diameter

Long embedded FBGs were used to measure the strain distribution in epoxy samples [88] and localise the crack front of mode I and mode II delamination [89–91]. Since only the change in the reflection spectra was used an a priori knowledge about the measured strain distribution was necessary. Another method to detect the position of a delamination crack tip is to use chirped FBGs [92–94].

2.2.2 OLCR based method

Optical low-coherence reflectometry (OLCR) allows to measure the length, position, and index modulation of FBGs [95]. Based on this technique Giaccari et al. [96] developed a method to determine the local Bragg wavelength. It combines OLCR measurements and reconstruction of local grating parameters by a layer peeling technique. Determining the local parameters was useful to improve the production of FBGs and it became rapidly clear that it would also open new perspectives for FBGs as strain sensors. Namely micro-mechanical measurements in non-homogeneous strain fields could benefit from this new method [97]

since it allows to measure distributed strains with a long FBG sensor without any prior knowledge of the strain field. With this method, strains caused by moisture absorption [98] and residual strains from curing shrinkage or thermal expansion mismatch [99] were measured. It was also used in fracture mechanics to determine strains around cracks in pure epoxy [100] and composites [101] and to measure changes of strain fields that are influenced by fibre bridging in composite materials [3, 4].

2.2.3 Multiplexd FBGs

Since a uniform FBG reflects only the light of a given wavelength, any other light can pass through the grating without being affected. Therefore, it is possible to write multiple FBGs with different Bragg wavelengths into the same fibre and interrogate them individually with the same device. This is called wavelength division multiplexing (WDM) and very important for filtering in telecommunication. In structural health monitoring WDM is attractive because it allows sensing in very remote places without adding much weight [74]. Not only measurements with remote sensors are possible with WDM, but also quasi distributed sensing [102]. For this, the FBGs are written very close to each other into the same fibre to form a sensor array. A strain distribution can thus be measured pointwise. The technique has been successfully used to monitor crack propagation and measure strain fields around crack tips in FRPs [103].

2.3 Summary

In this chapter the state of the art in the domain of delamination of long fibre reinforced composites and fibre optical strain sensors was described. Despite the fact that several standardized tests exist to measure delamination resistance of composites there is still ongoing research on certain related topics, namely, simulation of delamination, fibre bridging, friction, delamination between plies with different angles, fatigue delamination and mixed mode delamination.

The usefulness of fibre Bragg gratings as embedded strain sensors has been recognised very soon after their discovery, However, it's only in recent years that

researchers have started to use them to sense non-homogeneous strain fields and monitor cracks in fracture specimens and there is currently a lot of ongoing research in this field.

Chapter 3

Materials and methods

In the first section of this chapter, details of the sample preparation and the properties of the materials used in this work are given. The following sections describe the mechanical testing, the optical techniques for the strain measurements, the numerical methods, and the elements of fracture mechanics used to calculate the energy release rate. Descriptions of each test can be found in the respective chapters.

3.1 Manufacturing, material and testing

The samples tested in this work were manufactured with the carbon fibre - epoxy composite *SP 70* from *Gurit SP*^{TM}. This composite is mainly used in marine applications. The epoxy resin being a thermoset plastic, it can be in non-reacted or monomeric state which is usually liquid at room temperature, in partially reacted or sticky state, or in its fully cured state. A common way to produce high quality carbon-epoxy composites is to use *preprегs* which means prefabricated sheets of composite where the resin is in a partially reacted state. The use of prepregs ensures a good reproducibility of the fibre volume fraction and thus properties of the composite. Additionally, the process is not involving liquid resins which is simplifying the handling. The aforementioned composite was supplied in rolls of UD prepregs which were stored at $-18°C$.

The prepregs were cut into sheets of 200x150mm (fibre direction x transverse direction) and the individual sheets were stacked on an aluminium base plate.

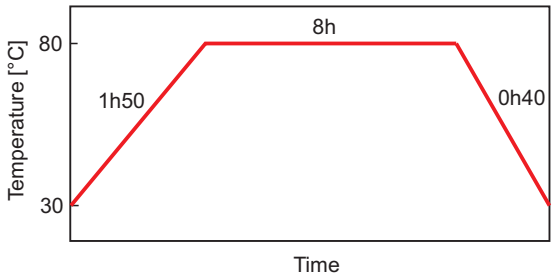

Figure 3.1: Curing cycle of the composite. Vacuum was applied during the whole cycle.

To reach a cured thickness of approximatively $4mm$, a total number of 20 plies with 0° orientation were stacked, forming a $[0_{20}]$ composite plate. Every five layers the stacking procedure was interrupted and a vacuum bag was placed over the lay-up to evacuate air bubbles that could form porosity later on. Once the final number of plies was reached, the composite was placed under vacuum in an autoclave oven and heated to the curing temperature of the resin. The complete curing cycle is shown in Figure 3.1. While the vacuum was maintained during the complete cycle, no additional external pressure was applied.

Since the delamination tests imply beam bending, a precise geometry of the samples, especially in thickness, was of great importance. For this reason the stacked composite was surrounded by an aluminium frame, shown in Figure 3.2(a), and covered with an aluminium plate. During manufacturing, a 60 mm long sheet of PTFE was placed between layers 10 and 11 over the whole width of the plate to form the initial crack. The sheet had been cut from $20\mu m$ thick release film A6000 from *Aerovac*®.

During the curing cycle the viscosity of the resin decreased which allowed it to fill out the frame. To prevent the resin from flowing out of the frame, the composite plate was backed with release film. The complete lay-up with the covering plate and a bleeder to achieve a good vacuum can be seen on the photograph in Figure 3.2(b). The connectors of the fibre sensors were protected with an L-shaped aluminium profile.

Fibre sensors (up to 4 fibres per plate) were placed one layer above the crack initiator, i.e. between layers 11 and 12 and grooves in the frame were used to guide them to the base plate where they were fixed with adhesive tape. Heat shrinkable

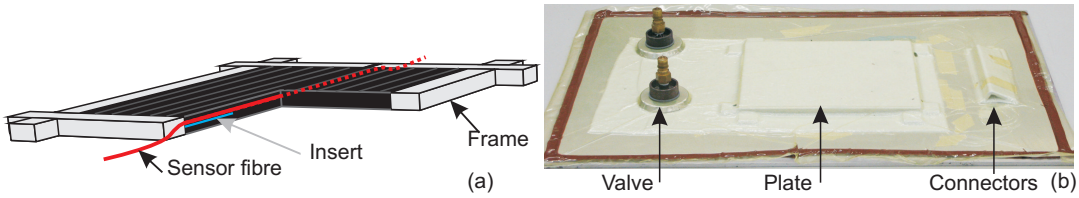

Figure 3.2: (a) A schematic of the lay up with the aluminium frame and the placement of the insert and the sensor fibre. (b) The photograph shows the lay-up as it went into the autoclave.

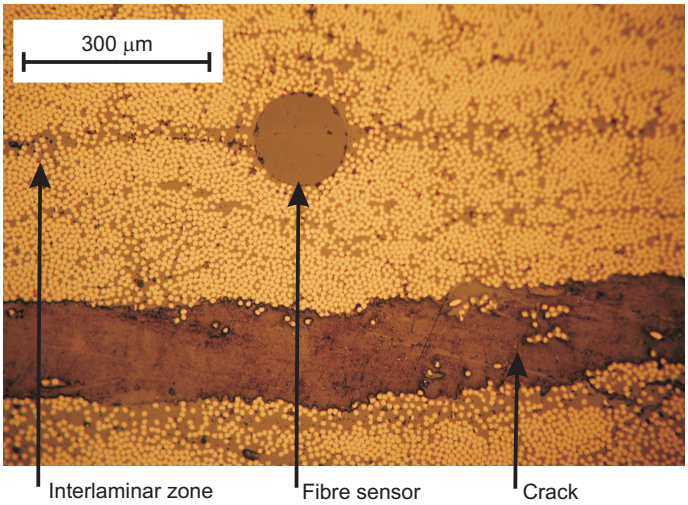

Figure 3.3: Micrograph of a delaminated specimen with the crack and an embedded fibre sensor.

PTFE tubes protected the fibres in the grooves and made un-moulding easier. To avoid resin flowing into the grooves the remaining space was filled with mastic.

In the FBG zone plus a few millimetres on each side of it the coating of the optical fibre was removed with sulphuric acid. A micrograph of a delaminated beam with such an embedded sensor is shown in Figure 3.3. Note, that it is very well surrounded by the carbon fibres (white in the reflected light) and that its position in the interlaminar layer has not changed during the curing.

The composite material was tested in three and four point bending as well as in tensile tests in fibre and transverse directions. From those tests the elastic moduli E_1 and E_2 as well as Poisson's ratio ν_{12} could be determined. The elastic modulus E_3 was supposed to be identical to E_2 and ν_{13} was supposed to be

Composite	E_1[GPa]	E_2[GPa]	E_3[GPa]	ν_{12}	ν_{13}	ν_{23}	G[GPa]
	98	9	9	0.3	0.3	0.45	5.2
Fibre sensor	E [GPa]	ν					
	70	0.16					

Table 3.1: Material properties used for simulations.

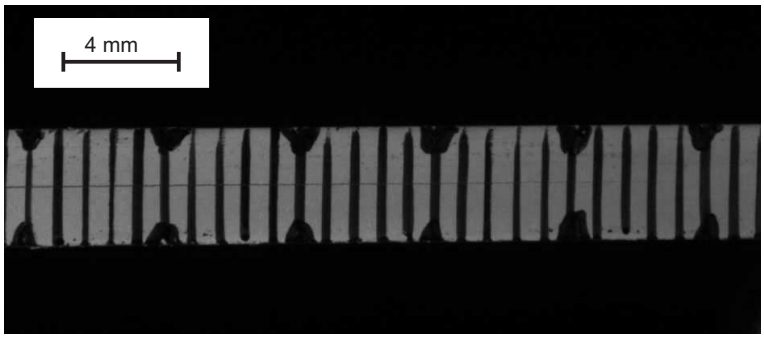

Figure 3.4: Graduation on the side of a delaminated sample.

identical to ν_{12}. The Shear moduli G (all supposed to be identical) and ν_{23} and the properties of the fibre sensor were taken from the literature [87]. A summary of the material properties as they were used in subsequent numerical simulations is given in Table 3.1

3.1.1 Specimens and test set-up

The $25mm$ wide test specimens were cut from the cured composite plates with a diamond saw. The cut sides of the beams were sanded and painted white on one side with a thin layer of acrylic spray. Starting at the end of the crack initiator, a graduation was drawn on the white painting with lines every millimetre and a triangular mark at the upper and lower edge every five millimetres as shown in Figure 3.4. This graduation was used during the test to determine the position of the crack tip. An inspection of the fracture surfaces showed that the crack tip was slightly curved but symmetric to the middle of the beam. Therefore, the crack length was determined from the graduation on one side of the specimen only.

Test	DCB monotonic	DCB fatigue	4ENF	MMB
Pre-crack length [mm]	30/60	30	60	50

Table 3.2: Pre-crack length for the different delamination tests.

While cutting the plate, care was taken that the fibre sensors were in the middle of the final specimen width. From each beam a few millimetres of the pre-cracked end were cut. This was necessary to eliminate potential defects from the side of the plate. Additionally, the cutting ensured that the sensor end coincided with the sample end. The position of the FBGs in the fibre sensor was then determined with respect to the sample end by an OLCR measurement (see section 3.2.1). For the fatigue DCB tests, the samples were further cut to a pre-crack length of $30mm$. Such short crack samples were also tested in monotonic loading. For mixed mode tests the pre-crack had a length of $50mm$ and for mode I and mode II it was $60mm$. Table 3.2 shows a summary of the pre-crack lengths for each delamination test.

For the DCB and the MMB tests, steel loading blocks with a dimension of 10x10x25mm were glued to the upper and lower surface of the specimens with a two component rapid epoxy. For the 4ENF tests, a steel cylinder of $10mm$ diameter was cut $2mm$ above the axis and glued to the cracked end of the specimens. This half cylinder replaced the roller and prevented the sample from horizontal sliding. Since the axis of the half cylinder lied on the load line, the crack length was clearly defined.

The different grips for the test set-ups are described in the respective sections: Section 5.1 for the DCB test (including fatigue), section 6.1 for the 4ENF test and section 7.1 for the MMB test.

3.1.2 Crack length measurements

Crack length is a key parameter to monitor the propagation of delamination. However, it is more difficult to measure as compared to load and displacement. In this work, the crack length was determined by inspection of photographs taken at regular intervals from one side of the sample using the graduation painted on the surface (see Figure 3.4). For every millimetre of visible crack propagation there

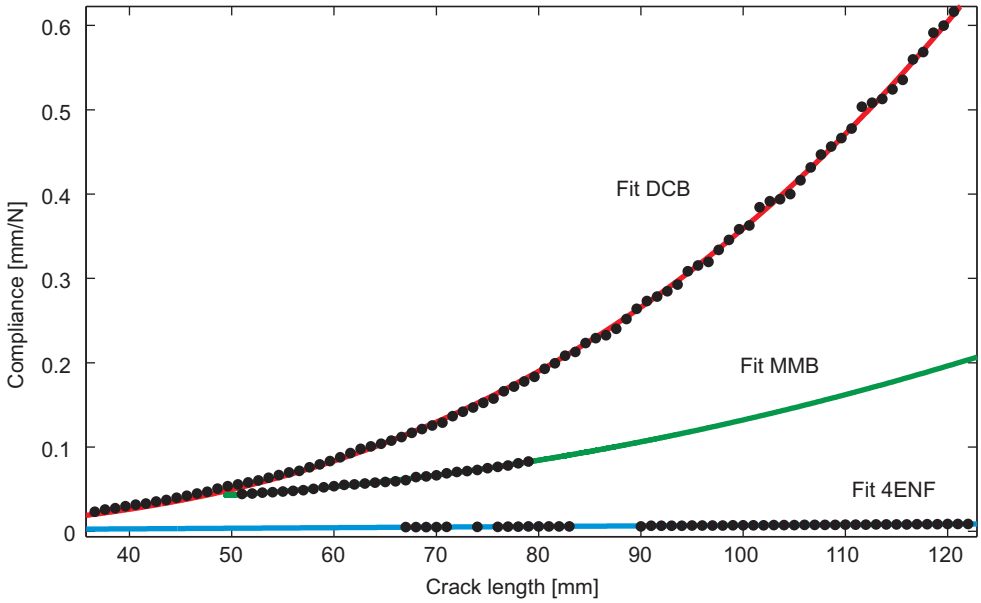

Figure 3.5: Fitting of the crack length versus compliance curves for DCB, 4ENF and MMB tests.

were at least four photographs. The precision of the crack length measurements can thus be estimated to $\pm 0.25mm$ for a stable growing crack.

For subsequent use in the compliance calibration method (Subsection 3.4.1), the crack length versus compliance data were fitted with an analytical curve. Since the compliance changes monotonically with crack length, any jumps occurring in curves of crack length versus compliance had to be due to errors in the measurement of crack length and were corrected by the fit. The analytical curves for the DCB were exponentials of the form:

$$C = Ba^m \tag{3.1}$$

where B and m are fitting parameters and C and a are the compliance and the crack length respectively. For the 4ENF test, the crack length versus compliance was well fitted with a first order polynomial and for the MMB test a second order polynomial offered a very good description. Figure 3.5 shows the measured data (points) and the fitted curves for all three test set-ups.

3.1.3 Testing machines

The delamination tests were performed with two different testing machines. For all monotonic tests a custom-built serve electric test machine from *Walter+Bai AG*, type EC80-MS® was used. The load was measured with a $1kN$ load cell in the DCB and MMB tests and with a $10kN$ load cell in the 4ENF tests. The machine was displacement controlled and set to a cross-head speed of $0.04mm/s$. The displacement was measured with the built-in LVDT.

For the fatigue tests on DCB specimens, an ElectroForce 3400 test machine from *BOSE*® was used. This testing machine is designed for fatigue tests and has a linear electric motor that allows for frequencies up to $200Hz$. Since the core of the motor is retained by two springs (one above and one below) the zero position of the cross head is in the middle of the total possible course. The samples were fixed to the cross head in the zero position, which means without current on the motor, thus the displacement was limited to $13mm$ corresponding to half the maximum cross head displacement of the machine. The displacement was measured with a built-in LVDT and the load with a $3kN$ load cell.

The samples were fatigued in load control at a frequency of $1Hz$ and a minimum to maximum load ratio of $R = 0.5$. The choice of these parameters is described in section 5.1.2.

3.2 Optical measurements

In this work optical glass fibres were used as strain sensors, more precisely, fibre Bragg gratings (FBG) that were written into a single mode optical fibre SM28. The glass fibres had a diameter of $125\mu m$ and were coated with polyacrylate or polyimide. Such single mode optical fibres are made of pure silica with a germanium dioxide doped core of $9\mu m$ in diameter which guides the light.

An FBG consists of a periodic change of the refractive index, n, in the core of the glass fibre created with a UV-laser. When light is guided through, it is partially reflected at each change of n and interferes with the incident one. The reflectivity of an FBG is controlled by the exposure time to the UV-laser and depends on the difference between the refractive index of the core and the altered

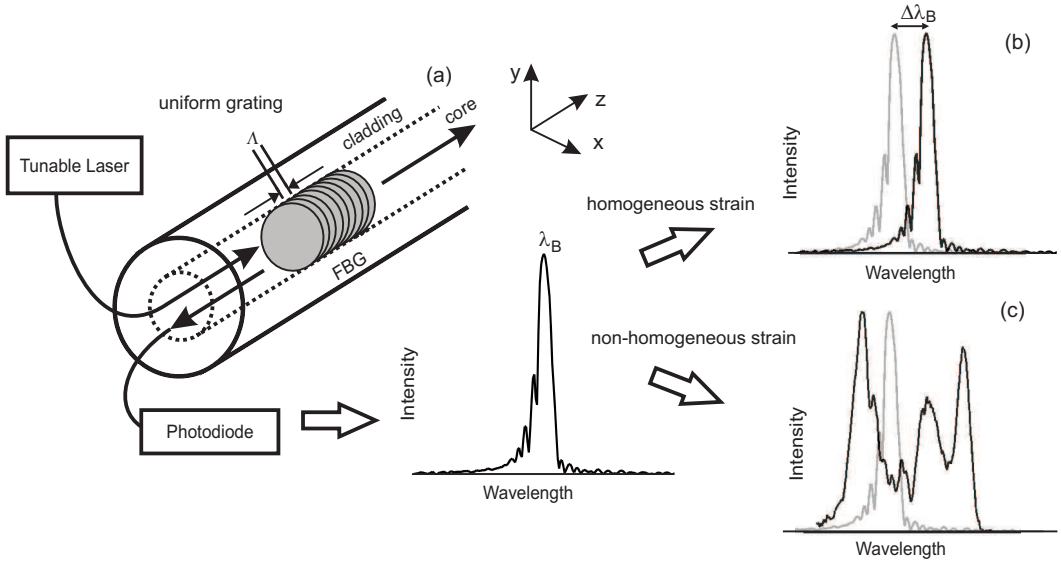

Figure 3.6: Working principle of an FBG: (a) Schematic of an FBG, (b) peak shift in homogeneous strain and (c) spectrum in non-homogeneous strain.

refractive index. FBGs with 50 to 70% reflectivity have proven to be well suited for sensing applications.

A schematic of a glass fibre containing an FBG is shown in Figure 3.6(a). The period, $\Lambda(z)$, of the index change is designed such that a specific wavelength, the Bragg wavelength λ_B, has a constructive interference and is thus reflected at the grating. The period and the reflected wavelength are related to each other by the Bragg condition:

$$\lambda_B(z) = 2n\Lambda(z) \tag{3.2}$$

If an FBG is uniform, i.e. Λ is constant, a narrow peak centred on the Bragg wavelength appears in the reflected spectrum. For a chirped grating where the period changes along the axis of the fibre, a band is reflected instead of a single peak.

It becomes clear from Equation (3.2) that any environmental factors that alter either the refractive index or the period of an FBG lead to a shift of λ_B. Namely, this applies to load and temperature changes. If a glass fibre is axially loaded, the period of the FBG changes proportional to the load. Additionally, the load leads to a change of the refractive index. In the same way, a variation in temperature

changes the refractive index and, because of the thermal expansion, the period of the grating. Figure 3.6(b) shows the peak shift, $\Delta\lambda_B$, in the spectrum resulting from a homogeneous strain.

When unequal transverse loads (in x- and y-direction) are applied to the fibre, its circular section changes to an ellipse and two zones of different stresses form. This leads to two different refractive indexes, and the fibre becomes *birefringent*. In such a case the Bragg peak is split up into two identical peaks which are designated according to the direction of the principle load, x and y. The generalised relation between $\Delta\lambda_B$ and strain in the fibre, ε, as well as temperature is thus given by the following equations where the loads are assumed constant along the fibre axis:

$$\frac{\Delta\lambda_{B,x}}{\lambda_{B0}} = \varepsilon_z - \frac{n^2}{2}[(p_{11}\varepsilon_x + p_{12}(\varepsilon_z + \varepsilon_y)] + \kappa\Delta T \tag{3.3a}$$

$$\frac{\Delta\lambda_{B,y}}{\lambda_{B0}} = \varepsilon_z - \frac{n^2}{2}[(p_{11}\varepsilon_y + p_{12}(\varepsilon_z + \varepsilon_x)] + \kappa\Delta T \tag{3.3b}$$

where p_{11} and p_{12} are the photoelastic coefficients in the direction of the considered transverse strain and in its orthogonal directions respectively. λ_{B0} is the initial Bragg wavelength and κ is the thermo-optic coefficient. The first term of Equations 3.3 accounts for the geometrical change of the grating whereas the second term describes the photoelastic effect and the third term accounts for changes in temperature. Often, the assumption can be made that ε_x and ε_y are the same. Furthermore, in many cases the transverse load is very small compared to the load in axial direction of the fibre and it can be assumed that the transverse strain is solely caused by Poisson's ratio. With these simplifications Equations (3.3) can be rewritten as:

$$\frac{\lambda_B(z) - \lambda_{B0}}{\lambda_{B0}} = \frac{\Delta\lambda(z)}{\lambda_{B0}} = (1 - p_e)\varepsilon(z) + \Delta T(z)\kappa \tag{3.4}$$

where p_e is the effective photoelastic coefficient and was deduced from:

$$p_e = \frac{n^2}{2}\left((1 - \nu_f)p_{12} - \nu_f p_{11}\right)$$

with ν_f being Poisson's ratio of the glass fibre. This coefficient was determined by suspending weights on a fibre containing an FBG and measuring the resulting wavelength shift it was found to be $p_e = 0.2148$ [104].

A distinction between the wavelength shift caused by an applied load and a change of temperature is not possible. Therefore, it is important to measure the temperature or to perform experiments at constant temperature. All experiments in this work were performed at constant temperature and thus the second term of Equation (3.4) was zero. The resulting relationship was used throughout this work to convert measured wavelength shifts into strain:

$$\frac{\Delta\lambda(z)}{\lambda_{B0}} = (1 - p_e)\varepsilon(z) \tag{3.5}$$

If the strain is homogeneous over the whole grating length, the reflected peak simply shifts as shown in Figure 3.6(b) and the strain in the fibre can easily be determined with Equation (3.5). However, when the strain is non-homogeneous along (z), as for example in an FBG which is embedded close to a crack tip, the peak flattens and splits in multiple peaks as shown in Figure 3.6(c). Despite the obvious influence of the non-homogeneous strain on the reflection spectrum, it is not possible to extract the distribution of strain $\varepsilon_z(z)$ directly from this spectrum.

To determine the strain distribution one needs to measure the local Bragg wavelength $\lambda_B(z)$. Two possible approaches were used in this work and will be described in the next subsections: a method which is based on optical low-coherence reflectometry (OLCR) and the use of wavelength division multiplexed FBGs.

3.2.1 OLCR measurements

This method was developed by Giaccari et al. [96] and combines the measurements of optical low-coherence reflectometry (OLCR) and the reconstruction of the Bragg wavelength by layer peeling. A schematic of the OLCR set-up is shown in Figure 3.7 [104]. The OLCR based method uses a Michelson interferometer which is time multiplexed. An optical switch changes between a broad band source with a coherency length of about $20\mu m$ and a tunable laser source. The light is then split into two arms with a coupler. At the end of the reference arm it is coupled out of the fibre into the air and reflected by a mirror mounted on a translation stage. In the test arm an FBG is reflecting the light.

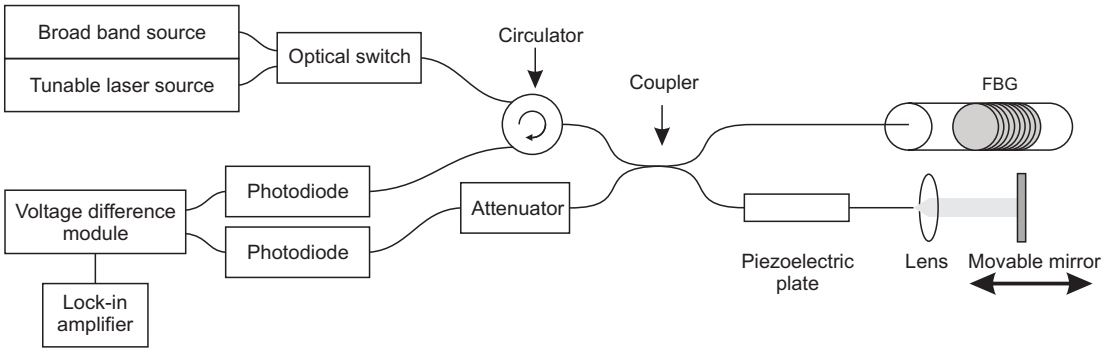

Figure 3.7: Schematic of the OLCR set-up using time multiplexing (see text for details).

A piezoelectric plate is ramp modulating the light at $178Hz$ in the reference arm to scan the interference pattern over 4π. The reflected light is then guided from the coupler to the photo diodes via two arms whereof one contains an attenuator. With the balanced detection by the voltage difference module the oscillating signal is enhanced and noise suppressed. The lock-in amplifier then detects the amplitude and phase of the signal from which the local Bragg wavelength is reconstructed by layer peeling [105, 106].

The time multiplexing between the tunable laser and the broad band source improves drastically the precision of the phase measurement. Indeed, instead of measuring directly the phase of the broad band source which changes thousands of radians over a few micrometers, the phase difference between the laser signal and the broad band signal is measured. This difference is varying very slowly with the changing wavelength of the reflected broad band light.

Before an experiment was started, the laser had to be tuned to a wavelength that was reflected by the considered FBG. For this, any of the peaks of the reflection spectrum (see Figure 3.6 c) could be chosen. Then, the optical switch was manually put to the broad band source and the mirror moved until a reflection signal was measured. To have a constructive interference, the optical path length of the reference arm must correspond to the optical distance of the FBG to the coupler within the coherence length of the broad band light. By moving the mirror, one can scan along the FBG, interrogating only that part of the FBG that is within the coherence length.

Using the broad band source only and controlling the position of the mirror, the beginning and end of an FBG can be determined. Since a cut fibre end is reflecting light and therefore leads to a peak in the OLCR spectrum the position of the FBG relative to the fibre end can be measured (see Figure 3.8 b). Because in this work the fibre end usually corresponded to one end of the specimen, this was an efficient way to precisely position the FBG in the sample.

Once the FBG was located and the laser tuned to a reflected wavelength, the measurement of the complex impulse response of the broad band source was initiated. Choosing a step length of $20\mu m$, the scan of a $25mm$ long FGB took about 30 minutes. From these measurements the local Bragg wavelength was reconstructed by layer peeling.

The drawbacks of this method are its limited speed, the complex apparatus and its sensitivity to movements. The latter is due to the sensitivity of the phase to any vibrations. The OLCR based method can therefore be used to measure static deformation states in a controlled environment. However, it is not possible to perform any measurements in moving parts such as in fatigue. Measurements of samples with relaxation are only possible if the relaxation time is much longer than the measurement time. To overcome these limitations, an alternative approach is needed.

3.2.2 Multiplexed FBG sensors

The FBG sensors used for the OLCR based technique were uniform and of a length of about $25mm$. When subjected to a non-homogeneous strain, the reflection signal was split up in several peaks. In contrast, the method presented hereafter used an array of wavelength division multiplexed short FBGs of only $1mm$ in length. These short gratings did not show peak splitting in non-homogeneous strain fields suggesting that over the length of $1mm$ the strains can be considered constant.

Figure 3.8 (a) shows the measured reflection spectra of an embedded FBG array in an unloaded sample (dotted line) and the same grating when a delamination crack tip is located between grating 3 and 4 (solid line). Note that the array was placed such that the FBG with the longest wavelength was in tension

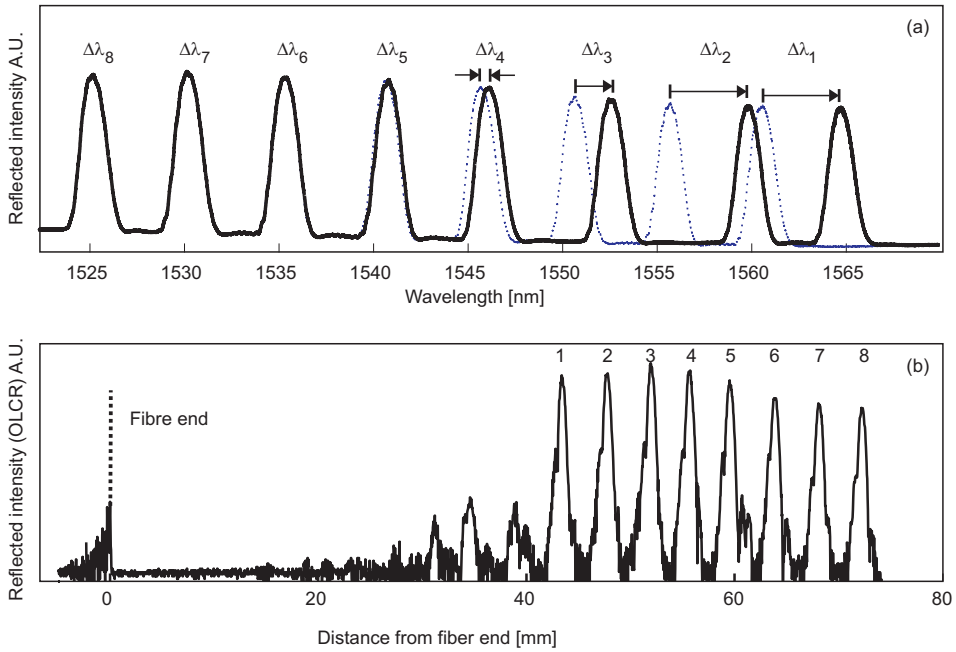

Figure 3.8: (a) Reflection spectra measured with the *SM130* device before testing (dotted line) and when the crack is between FBG 3 and 4 (solid line). (b) OLCR amplitude measurement of the same sensor array

first. This way, an overlap of the peaks was avoided. The sensor was embedded one layer above the crack plane and connected to an acquisition device *SM130* from *Micron Optics*®. Each of the four channels of the *SM130* can interrogate up to 16 gratings at the same time at an acquisition rate of $1000Hz$. The position of each FBG with respect to the fibre end (corresponding to the sample end) was measured by OLCR as shown in Figure 3.8(b).

The multiplexed sensors used in this work consisted of an array of eight FBGs. Figure 3.9 illustrates how such a sensor array is used for quasi-distributed strain sensing taking as example delamination in a DCB test. (a) As long as the crack tip and its associated strain field is far away from the sensors, the Bragg peak of each FBG does not change. Note that bending of the sample (e.g. in mode II and mixed mode tests) cause a small shift if the sensor is embedded away from the neutral axis. (b) When the crack further propagates, the Bragg peaks shift as the strain field ahead of the crack tip reaches the FBGs. (c) When the crack has passed the array, all sensors are in the zone where bridging can occur.

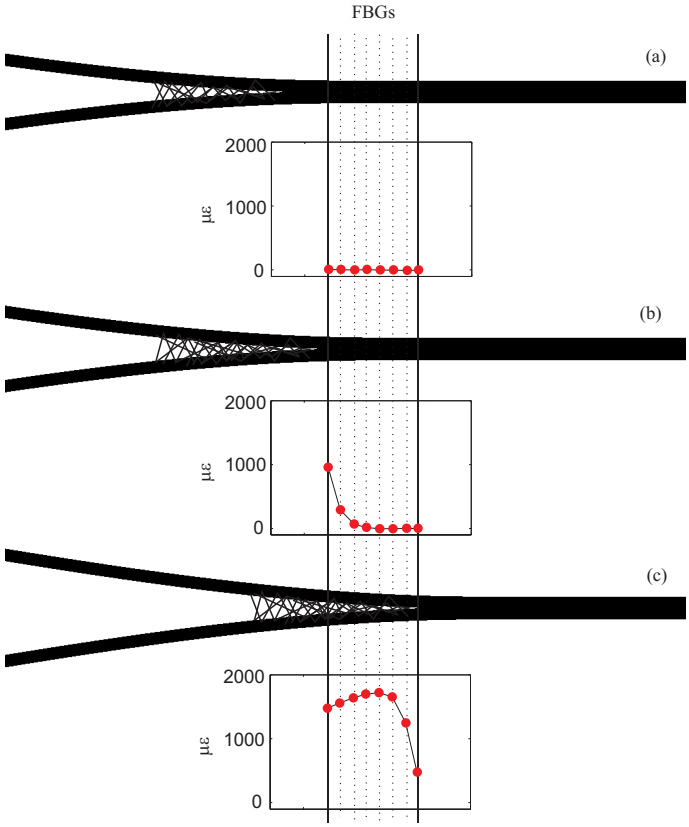

Figure 3.9: (a) The crack is far away from the FBGs. (b) The strain field associated to the crack tip reaches the FBGs. (c) The FBGs are in the bridging zone. Note that the DCB is a schematic and the strains, as measured experimentally, are superimposed on the appropriate crack length.

It is important to note that there are two ways to consider these measurements:

1. At each crack length (or time of the test) one obtains a point-wise strain measurement of as many points as the array has FBGs. Such a measurement is shown in Figure 3.9 at three different crack lengths for an array with eight FBGs. The strain was calculated from the measured wavelength shift using Equation (3.5) for each of the three crack lengths.

2. The signal of each FBG versus time gives the evolution of strain at a given point in the structure as a crack passes nearby. Figure 3.10 shows the

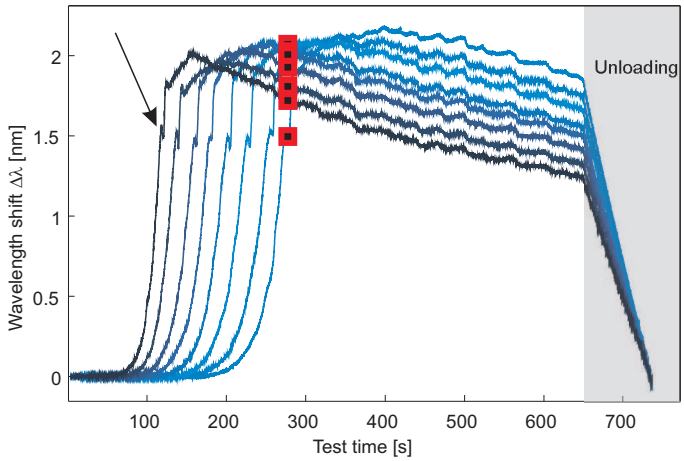

Figure 3.10: Measurements of an array with eight gratings during a DCB crack propagation. The arrow indicates the position of the crack tip, characterized by a v-shaped dip. The data points when the crack tip reaches the last FBG are marked by squares.

wavelength shift in a DCB test measured with an array of eight FBGs. The squares show the data points corresponding to Figure 3.9(c), i.e. the strain for each sensor at this given time (crack length).

The first case gives directly a point-wise strain distribution at a given time. Knowing the crack length versus time, the strain at the FBG positions is obtained for any crack length. This can be considered as being the best possible way of measurement since there is no approximation used. However, for the further use in identification (see section 3.3.1) the small number of data points increase the sensitivity to measurement noise and material irregularities. Therefore a continuous curve would be preferable.

Clearly, if the strain field was identical at different crack lengths, the eight curves in Figure 3.10 (transformed to strain versus crack length) were equal and each of them would represent the axial strain distribution at any crack length. However, the strain field changes as the crack advances because of the change of the geometry of the sample and of bridging. This can be seen clearly when the curves are shifted to the same origin (taken as the position of the last FBG in the array) as shown in Figure 3.11. The squares are the same as in Figure 3.10 and show the strain as it is measured by the array when the crack tip is at

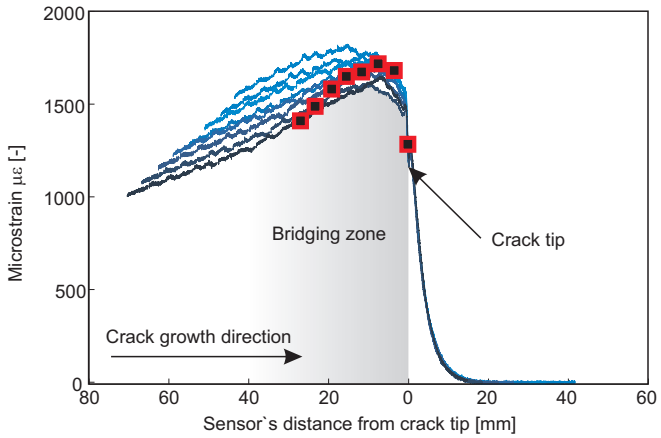

Figure 3.11: Strain measurements in a mode I delamination shifted to a common origin. The squares correspond to those in Figure 3.10

the position of the last FBG corresponding to the point-wise strain distribution shown in Figure 3.9(c).

It becomes clear from Figure 3.11 that not all acquired data can be used. However, it is possible to use more than just one data point per FBG of the array. For this, one has to assume that the curvature of the sample and the bridging does not change significantly when the crack propagates by a small distance. Namely, a crack propagation of $\pm 2mm$ is used which can be considered as the characteristic length of the sensor since the distance between the centres of two FBGs is $4mm$. In that way, the number of data points can be drastically increased and a quasi-continuous strain curve is obtained. Note that the resulting strain distribution is discontinuous if the above mentioned assumptions are not verified.

3.3 Numerical methods

In this work finite element models were used for two purposes: i) with a parametric FE-model material properties such as fibre bridging and ERR were identified and ii) the identified parameters were implemented in cohesive element models and the resulting load-displacement curves were compared to the experimental ones to verify the findings. In this section, the inverse identification method and

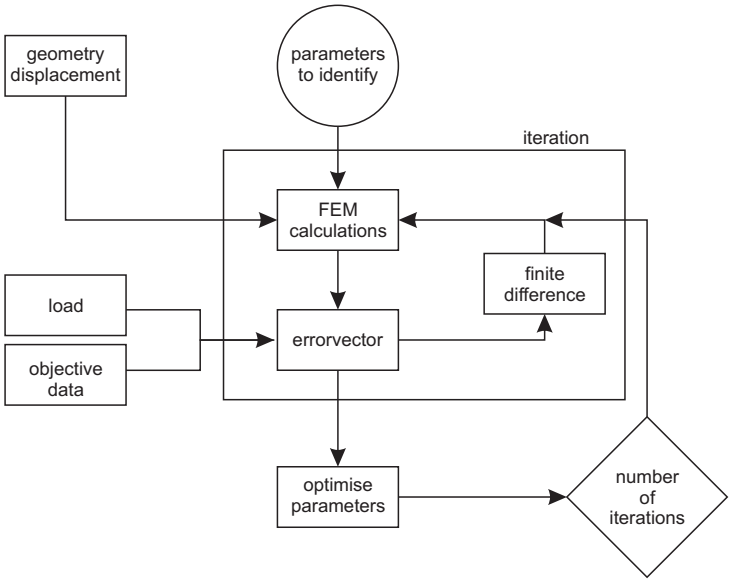

Figure 3.12: Flowchart of the inverse identification.

the cohesive elements are described.

3.3.1 Inverse identification

The axial strain distribution, ε_{FBG}, which was measured with the FBG sensors was used as objective data set in an inverse identification method [3, 107] which is based on a parametric FE-model and a *Matlab*® routine for optimisation. A flowchart of the inverse identification is shown in Figure 3.12.

First, a numerical model of the experiment was created. It was important that the model represented the experiment as close as possible at the time when the strain distribution was measured, namely the imposed displacement and the sample geometry. The specific problem dictated the choice of parameters to identify. In the case of mode I and mixed mode delamination this were the parameters defining the bridging traction distribution and for mode II delamination the friction coefficients and the cohesive law. It was usually useful to introduce bounds for the parameters to guarantee the convergence of the numerical model during the whole identification process.

The numerical model was then solved and the axial strain at the position of the FBG, ε_{FEM} extracted. From the two strain distributions, ε_{FEM} and ε_{FBG},

an error vector $F(x_1, x_2, x_3 \ldots)$ was calculated according to:

$$F(x_1, x_2, x_3, ...) = \frac{1}{2} \left\| \frac{\varepsilon_{FEM} - \varepsilon_{FBG}}{\langle \varepsilon_{FBG} \rangle} \right\|^2 \tag{3.6}$$

where $\langle \varepsilon_{FBG} \rangle$ designates the average value of the simulated axial strains at the FBG position. Since the number and position of measured strain points, ε_{FBG}, did not correspond to the number of the simulated strain points, ε_{FEM}, the latter ones were projected onto the coordinates of the first ones by a linear interpolation. Thus, the dimension of the error vector was as large as the one of the vector containing the measured strain data points. To guarantee the correct energy of the system, the load was included into the optimization. For this, a penalty value depending on the simulated load P_{FEM} was appended to the error vector. This value was calculated as:

$$\frac{dim(F)}{2} \frac{P_{FEM} - P_{exp}}{P_{exp}}$$

where $dim(F)$ is the dimension of the error vector as described in Equation (3.6) and P_{exp} is the load measured during the experiment at the simulated crack length. The weight attributed to the load in the optimization was thus half the weight of all strain data points. This was an arbitrary choice and could be changed by changing the value of the first denominator.

For a complete iteration, the numerical model was calculated once with the initial parameters and then again for each parameter varied by 1% of its current value while keeping the others unchanged. Using the resulting differences the error vector was minimized. Without bounds, a Levenberg-Marquardt algorithm was used and if bounds were applied, a trust-region-reflective algorithm was used, both built-in in *Matlab*®. At the optimum, the difference between the measured strain and the simulated strain at the position of the FBG as well as the difference between the measured load and the simulated load was smallest.

The optimization was first run for 15 iterations and then the evolution of each parameter and the residual as a function of iteration steps were analysed. When the value of all parameters reached a plateau, convergence was obtained. The optimization was then repeated for different sets of initial values, reducing the number of iterations to the number where the convergence had been found.

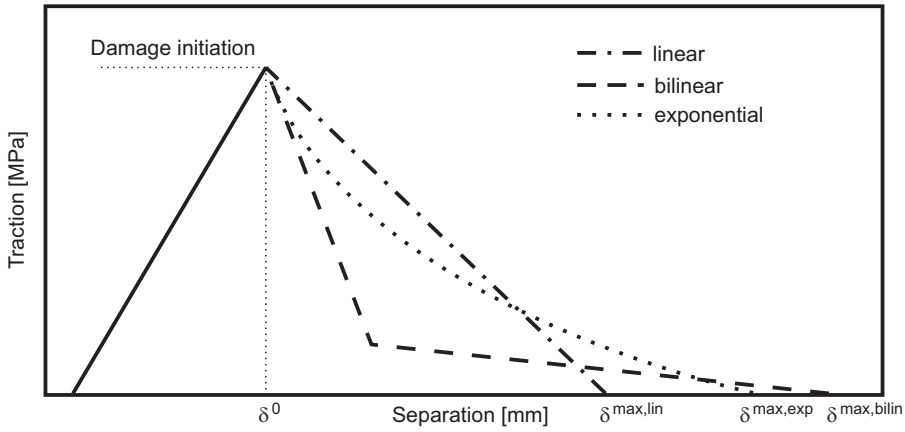

Figure 3.13: Typical traction separation curves for cohesive elements.

3.3.2 Cohesive element models

Cohesive elements are special purpose finite elements which are very well suited to model delamination. They are placed in a thin layer of one element thickness in the crack plane. Clearly, the path of the crack needs to be known in advance which is usually the case for delamination cracks since they propagate in an interlaminar layer.

The material behaviour of cohesive elements is defined by a traction separation curve also called *cohesive law*. It is initially linear elastic until the predefined damage criterion is met. From then on, the stiffness is multiplied with a damage parameter and decreases progressively to zero. Figure 3.13 shows three different cohesive laws where the reduction in stiffness of the element is linear, bilinear, and exponential.

The parameters defining the cohesive law are the initial stiffness, the damage initiation criterion, the form of the decrease of the stiffness, and the total energy under the curve or equivalently the maximum separation δ^{max}. For this work, the following guidelines were used to chose these parameters: The initial stiffness had to be chosen in a way that the cohesive elements did not influence the global stiffness of the model. For this, either a very high stiffness was chosen or the mesh was modified to reduce the thickness of the cohesive elements to zero. The damage initiation criterion was chosen to be in the range of the maximum transverse stress

of the composite for mode I. In the mode II models, the damage initiation criterion was identified.

The surface under the traction separation curve corresponds to the fracture energy needed to propagate the delamination. For mode II this was a parameter to identify and the reduction of stiffness was chosen to be linear. In the case of mode I, one part of the energy was determined by experiments and the other by the identified bridging law as detailed in Subsection 5.4.4.

3.4 Calculation of the energy release rate

In the following paragraphs the derivation of some key expressions in linear elastic fracture mechanics is presented. The description is based on the energy approach of Griffith [108] as described in the textbooks of Kanninen and Popelar [109] and Anderson [110].

The total energy of a brittle linear elastic material with a crack which is loaded with the remote stress σ is given by:

$$\Psi = \Pi + W_s \tag{3.7}$$

where Ψ is the total energy of the system W_s is the work required to create new crack surfaces and Π is the potential energy which is given by the difference between the strain energy U and the work done by the applied load, F_P:

$$\Pi = U - F_P \tag{3.8}$$

where F_P is:

$$F_P = P\delta$$

with P the applied load and δ the displacement of the load application point. In the case of a linear elastic material, the strain energy is given by:

$$U = \frac{1}{2}P\delta$$

which, replaced in Equation 3.8, gives for the potential energy of the system:

$$\Pi = -\frac{1}{2}P\delta \tag{3.9}$$

Using the result in Equation 3.9, the total energy of the system in Equation 3.7 can now be written as:

$$\Psi = -\frac{1}{2}P\delta + W_s \tag{3.10}$$

The necessary condition for the crack to propagate is given by the first derivative of Equation 3.10 with respect to A which is the crack surface:

$$\frac{\partial \Psi}{\partial A} = \frac{\partial \Pi}{\partial A} + \frac{\partial W_s}{\partial A} = 0 \tag{3.11}$$

For a through the thickness crack, A corresponds to the crack length a times the width of the cracked specimen B. When this condition is fulfilled, the crack propagates. To find out if the crack growth is stable or not, one needs to investigate the stability of the system which is determined by the second derivative of Equation 3.10. Since $\partial W_s/\partial A$ is constant, the sufficient condition for an unstable crack propagation is given as:

$$\frac{\partial^2 \Psi}{\partial^2 A} = \frac{\partial^2 \Pi}{\partial^2 A} < 0 \tag{3.12}$$

The term $\partial\Pi/\partial A$ in Equation 3.11 is defined as *energy release rate* ERR, also abbreviated as G so that:

$$G = -\frac{\partial \Pi}{\partial A} \tag{3.13}$$

In a load controlled test, the combination of Equations 3.9 and 3.13 yields:

$$G = \frac{P}{2B}\left(\frac{\partial \delta}{\partial a}\right)_P \tag{3.14}$$

Introducing the compliance C of the considered cracked body which is defined as:

$$C = \frac{\delta}{P} \tag{3.15}$$

Equation (3.14) becomes:

$$G = \frac{P^2}{2b}\frac{dC}{da} = \frac{1}{2b}\frac{\Delta^2}{C^2}\frac{dC}{da} \tag{3.16}$$

Note that Equation 3.16 can also obtained for a cracked body in displacement control.

Equation 3.16 is very important, since it shows a way to determine G experimentally by measuring crack length, the applied load, and displacement. Clearly, an analytical expression for compliance as a function of crack length is preferable to simplify the derivation and eliminate scatter.

3.4.1 Compliance methods

A very popular way to measure the ERR, also suggested in the available standards for delamination tests, is to derive a description of the compliance $C(a)$ by simple beam theory. This expression can then be introduced in Equation (3.16) and G is easily found. Corrections for the rotation of the laminate at the crack tip are usually given in the standard. However, the beam theory is a large simplification and may introduce errors, especially if fibre bridging or friction is present.

A similar approach is to fit an analytical expression on a compliance versus crack length curve. Since in this work the crack length data were fitted by a polynomial or exponential to improve precision (see 3.1.2), this same expressions were used in Equation (3.16) to find the ERR as a function of crack length. The advantage of this approach is that the global compliance of the specimens is measured and local phenomena like bridging are automatically taken into account.

3.4.2 Crack with bridging

Equation (3.16) was derived for linear elastic, brittle materials. For the composites treated in this work this is a reasonable assumption. However, during crack propagation the creation of new surface is not the only mechanism that requires energy, namely, fibre bridging can also occur. For further crack propagation, the bridging fibres have either to be broken or pulled out of the matrix. While the surface energy contribution to ERR is constant during crack propagation, the contribution of fibre bridging is initially absent and increases when the crack propagates. One can write:

$$G(a) = G^i + G^b(a) \tag{3.17}$$

where G^i is the initial ERR corresponding to the energy required to create a unit surface of crack in the absence of bridging, and $G^b(a)$ is the contribution of the bridging fibres which is a function of crack length. From Equation (3.17) we have the total energy release rate $G(a)$ starting at G^i when the crack is initiating. During propagation, the contribution of $G^b(a)$ increases until the bridging zone is fully developed. The ERR becomes constant and is called *propagation value* or G^p. This increase in ERR is usually referred to as *R-curve* behaviour.

The work that is needed to overcome the resistance of the bridging fibres, $G^b(a)$, is obtained by integrating the bridging traction $\sigma_b(\delta)$ over the separation of the two crack surfaces δ. It can be written as follows:

$$G^b(a) = \int_0^{\delta^*(a)} \sigma_b(\delta)\,\mathrm{d}\delta \tag{3.18}$$

where $\delta^*(a)$ is the displacement at the end of the bridging zone. The traction separation behaviour, also called *bridging law*, $\sigma_b(\delta)$, is supposed to be independent of the crack length. It can be experimentally obtained [36] by deriving the measured $G(a)$ with respect to δ^* according to:

$$\sigma_b(\delta) = \frac{\mathrm{d}G^b(a)}{\mathrm{d}\delta^*} \tag{3.19}$$

The difficulty of this method is the determination of the end of the bridging zone and therefore the measurement of a correct δ^*. Also, because of the derivative, the measured ERR values have to be fitted by an analytical expression.

3.4.3 Area method

Another, straight forward way to measure the ERR of a material is to determine the strain energy directly from the load-displacement curve [111]. For this, the sample is unloaded and reloaded at several crack lengths. Or, for a truly linear elastic material equivalently, straight lines are drawn from several points on the load-displacement curve to zero as it is shown in Figure 3.14 for a load displacement curve of a DCB test. The area ΔA_i, delimited by two unloading-loading lines and the load displacement curve, corresponds to the energy that was required to propagate the crack from crack length $a_{(i-1)}$ to a_i. This energy is then divided by the created crack surface to obtain G according to:

$$G(a_1) = \frac{\Delta A_1}{B(a_1 - a_0)} \quad , \quad G(a_2) = \frac{\Delta A_2}{B(a_2 - a_1)} \quad , \ldots \tag{3.20}$$

This method is clearly the closest to the definition of energy release rate (see Equation (3.13)). However, there are some limitations in its use. Namely, when the crack is propagating with jumps, there is also kinetic energy that needs to be

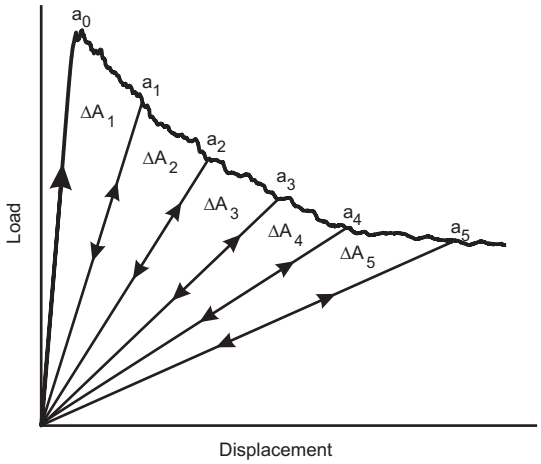

Figure 3.14: Illustration of the area method on a mode I delamination load-displacement curve.

taken into account. Also, it is necessary to allow for a certain crack propagation and thus the measured ERR is an average over this crack propagation which is not desirable - especially at the beginning of the R-curve when $G(a)$ changes rapidly with crack length.

3.5 Summary

In this chapter the fabrication of the composite material and the test specimens was described. The way of placing the sensor fibre and guiding it out of the composite has worked properly for this simple geometry. However, there is no standard or *best practice* of including an FBG as strain sensor in composite parts. This is clearly a field for future improvements.

Further, two methods for distributed strain sensing with FBGs were described. Even though the OLCR-based method has produced very good results, the complexity of the instrumentation and the low measurement speed limit its application. The multiplex method is a good alternative. Even if the direct measurements of the strain are only point-wise, it is possible to deduce a quasi-continuous strain distribution. Additionally, this method is much faster, can be used in fatigue, and commercial interrogators are available.

Finally, a description of the inverse identification method using the measured strain distributions and different experimental approaches to measure the energy release rate of a delamination crack based on fracture mechanics was given.

Chapter 4

Crack - Sensor interaction

Throughout this work, embedded optical fibres were used to measure strain in the vicinity of a crack tip. Despite the small diameter of only $125\mu m$, the fibre sensors were an order of magnitude larger than the carbon fibres of the surrounding composite material and thus formed a considerable inclusion. Two questions needed to be addressed: i) is the behaviour of the crack influenced by the presence of such a sensor and ii) does the sensor measure the strains due to the crack tip. The latter was necessary since the sensor fibre could potentially influence the strain field it was intended to measure by its own presence.

There is no analytical solution available to calculate the stress field around a crack with a long inclusion in its vicinity for an anisotropic material. Therefore, an FE-simulation of a DCB test was performed to examine the stress-strain field in and around the glass fibre. Further, the energy release rate along the crack front was determined to reveal an eventual influence of the glass fibre on the crack propagation. Since all three performed tests (mode I, mode II, and mixed mode bending) involved bending of the composite, the presence of a fibre sensor can be expected to have a similar influence for each of these tests. Therefore only mode I was investigated.

4.1 Sub-model

The glass fibre being very small, a numerical model with two scales was created to study its interaction with the crack. First, a three dimensional model of a DCB

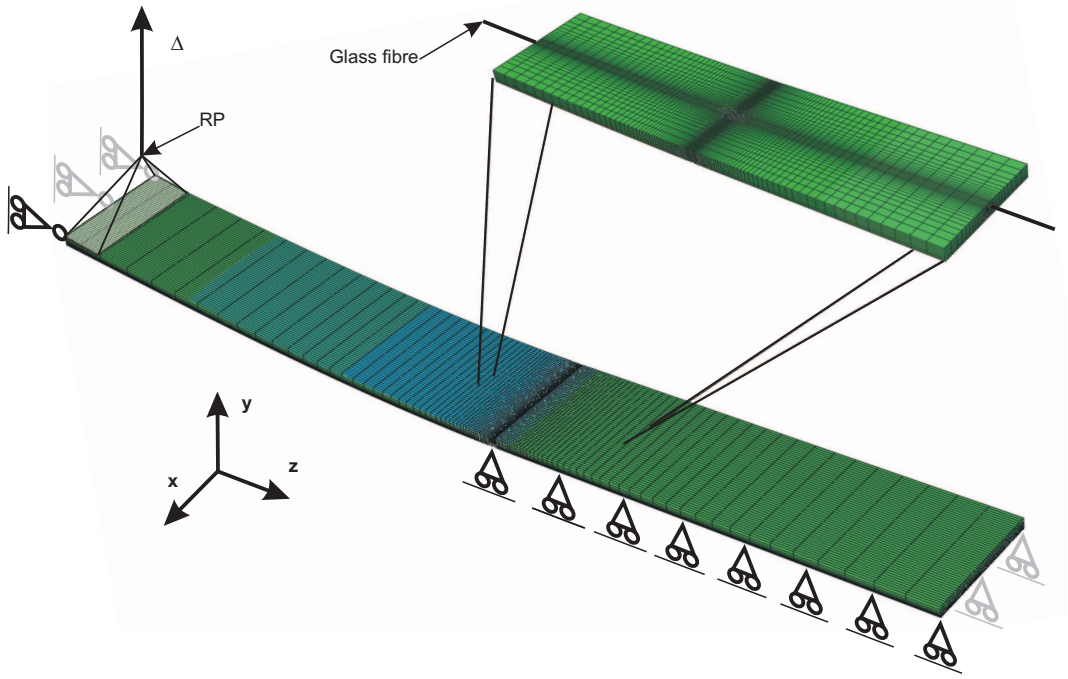

Figure 4.1: 3D model and the sub-model that was cut out to simulate the influence of the fibre.

specimen (see section 5.1) with a crack length of $105mm$ was created. Hereby, the symmetry of the sample allowed to simulate only the upper half. Even though the DCB specimen has also a symmetry in the width direction, the full width of the sample was simulated, otherwise, the glass fibre (being in the middle of the sample) would have been on the boundary. The crack was simulated without bridging tractions and symmetry boundary conditions were applied to the part of the beam which was ahead of the crack tip as shown in Figure 4.1. From this global model, a small part of $(20x4.5x0.5)mm$ in the centre around the crack tip was isolated and meshed with a much finer mesh. In this so called *sub-model* the glass fibre was modelled at a distance of $270\mu m$ from the crack plane. The global model and the sub-model are shown in Figure 4.1 and a zoom on the crack tip zone of the sub-model including the glass fibre is shown in Figure 4.2.

First, a displacement of $\Delta = 10mm$ was applied at the reference point (RP) to deform the global model and the displacement field at the boundary to the sub-model was extracted from the results. This displacement field served then as

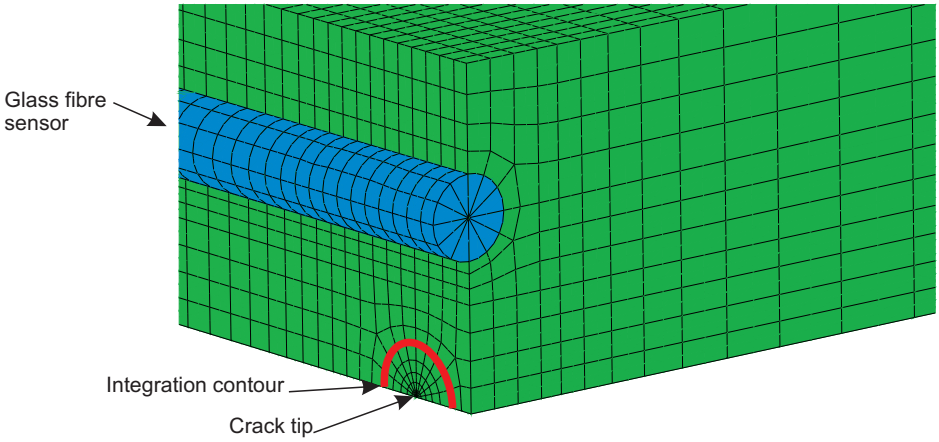

Figure 4.2: Mesh of the sub-model in the region of the crack tip and the glass fibre.

boundary condition for the sub-model.

The fibre sensor was meshed with quadratic wedge elements (Abaqus C3D15) and for the rest of the sub-model as well as the global model quadratic brick elements (Abaqus C3D20R) with reduced integration were used. A $1/\sqrt{r}$ stress singularity at the crack tip was obtained by collapsing one edge of the elements next to the crack tip to form wedges and by shifting the mid-points on the adjacent edges to one quarter of the edge length.

The fracture surface of all tested DCB specimens showed that the crack front was slightly curved towards the edges, the so called *crack bowing shape*. This is due to the plane stress condition that prevails at the sample surface compared to the plane strain condition in the middle. Despite these experimental observations, the crack front was modelled straight for simplicity. However, this simplification has to be kept in mind when considering the energy release rate along the crack front.

4.2 Energy release rate along the crack front

To evaluate the influence of the fibre sensor on the crack propagation, the energy release rate along the crack front was determined with the domain integral method [112] implemented in Abaqus®. The contour, as indicated in Figure 4.2, was taken

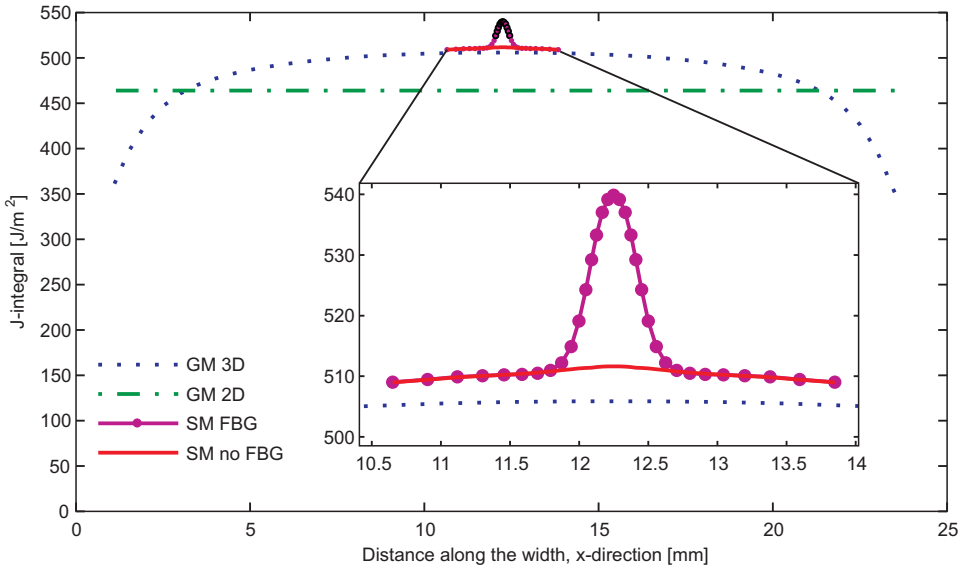

Figure 4.3: Energy release rate along the crack front for the global model (GM) and the sub-model (SM).

at a distance of five elements from the crack front which corresponded to $75\mu m$. The results for both, the global and the sub-model are shown in Figure 4.3. For comparison the value of a global 2D model with plane strain elements is shown as well.

The drop of the ERR towards the surface of the sample is due to the plane stress condition that prevails together with the straight crack front in the model. In the centre of the sample, the simulated ERR is almost constant which indicates that plane strain conditions can realistically be assumed for a 2D model simulating the centre of such a specimen. However, the integral over elements at the end of the crack front, i.e. at the surface of the beam, were not accurate. This is due to the skewness of the surface elements giving wrong results in the domain integral method (Abaqus handbook). Also, the singularity there is unknown and not accounted for.

The insert in Figure 4.3 shows a zoom on the part with the sub-model. The effect of the fibre sensor is clearly distinguishable as a peak appearing right below it. However, this peak is highly local with an increase of the calculated ERR of 7%. Its influence on the overall fracture behaviour of the specimen was considered

negligable. A comparison of load displacement curves of specimens with and without fibre sensors [3] confirmed that they can not be distinguished. To check that the reported local increase of the ERR was caused by the presence of the fibre sensor and was not an artifact of the mesh, the model was calculated twice. In the first case, material properties of glass fibres as reported in Table 3.1 were assigned to the model fibre and in the second case the material properties of the surrounding host material. In the second simulation, the peak was not present confirming that it was caused by the presence of the glass fibre.

4.3 Strain in the glass fibre

As the fibre sensor was placed close to the crack plane it was exposed to high strain gradients, especially in the proximity of the crack tip. Because of the difference in modulus of the glass fibre and the composite material, the strain field was disturbed. The sub-model was used to check that the presence of the fibre sensor did not change the strain in the centre of the fibre where the FBG is located.

For this, the strain in the axis direction of the fibre was extracted along a path in y-direction. The path started at the crack tip and finished at the surface of the sub-model passing across the fibre sensor. Figure 4.4 shows the strain distribution along this path. The two curves stem from models with identical meshes but one with glass properties for the fibre sensor and the other with composite properties (called no fibre in the figure). As expected, the fibre sensor, which is indicated as shadow in the figure, disturbed the strain field. However, in the centre of the fibre the strains were identical for the two cases. Since the sensing part of the fibre is located in the core of a diameter of $9\mu m$, it can be concluded that the correct strain was measured with the embedded fibre sensors.

The analysis described above shows a strong influence of the fibre sensor on the strain distribution in the surrounding material. It is therefore important to check the validity of the strain measurements for each new loading case.

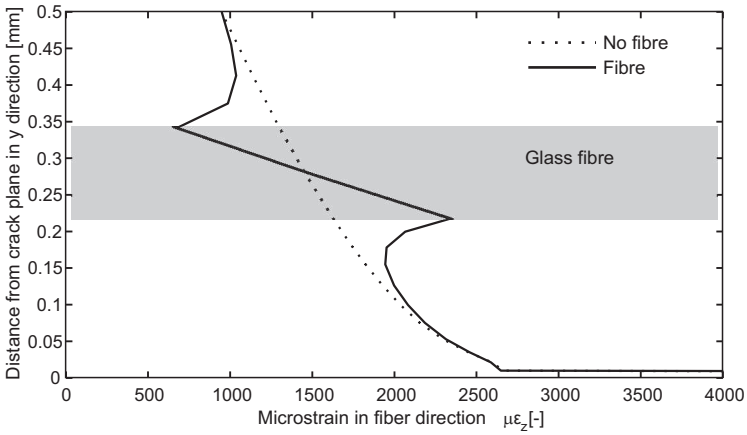

Figure 4.4: Simulated strain in fibre direction along an out of plane path.

4.4 Summary

In this chapter the interaction of a fibre sensor with a crack in its vicinity was analysed. For this purpose, a two-scale 3D model of a DCB sample was created with the sub-model sufficiently refined to model the fibre sensor. The energy release rate along the crack front showed that the influence of the fibre is local and small enough that it should not affect the crack propagation behaviour of the sample. Despite the influence of the fibre on the strain field close to the crack tip, the strain in the centre was found to be equal to a model without glass fibre. This shows that the fibre sensor can be used to measure the strain close to a crack tip in a delamination test.

Chapter 5

Mode I delamination

In the beginning of this chapter the test set-up and the results of the mode I tests with double cantilever beams are discussed. Then, the strains measured with the embedded fibre sensors using both, the OLCR based method and the multiplexed method are presented. These measurements were used to identify the bridging tractions. The results of the identification were then analysed with a cohesive element model and in terms of stress intensity factor.

5.1 Test set-up

The composite samples were tested in mode I with a double cantilever beam test. Figure 5.1 shows the set-up of the test according to the ASTM standard D5528 [44]. The loading blocks were connected to the test machine with ball joints and therefore with five degrees of freedom so that the only load was in the opening direction of the crack. To keep the specimen in a horizontal position, the free end was supported before the test started. In this test, the crack propagates in the central plane where the crack initiator had been placed due to the layered structure of the composite material.

Because of a resin rich zone behind the PTFE insert, the crack propagation started for most experiments with a jump. After this jump, the samples were unloaded and reloaded to propagate the delamination from a sharp natural crack. In the wake of the crack, fibre bridging was clearly visible as shown in Figure 5.2 and the breaking of fibres was clearly heard during crack propagation.

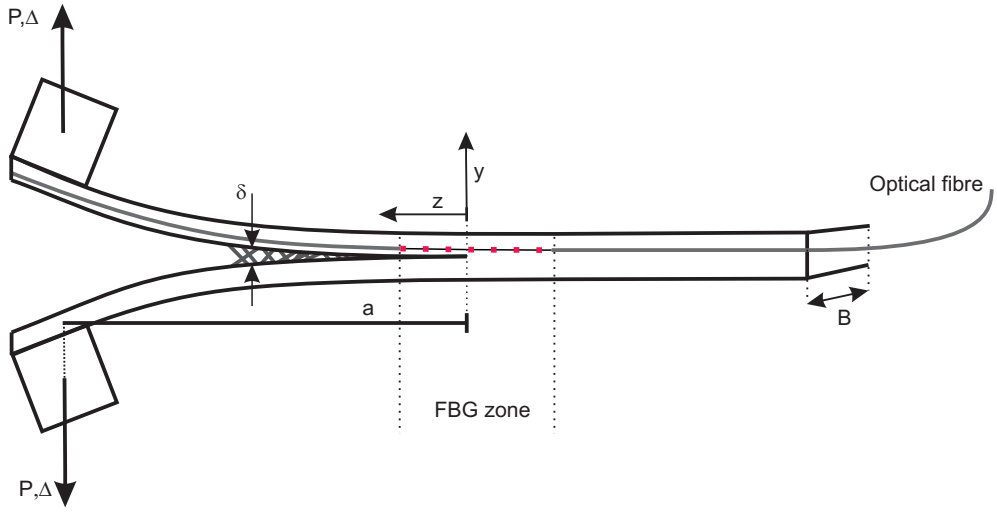

Figure 5.1: Schematic of a DCB set-up with an embedded optical fibre sensor.

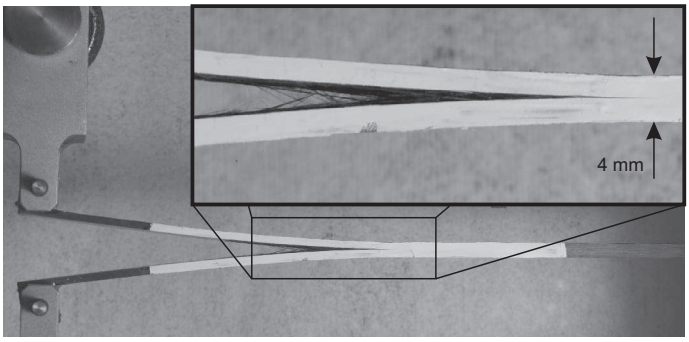

Figure 5.2: Bridging fibres in a DCB test.

5.1.1 Monotonic loading

As proposed by the ASTM standard, the samples were loaded in displacement control at a rate of $0.04mm/s$ which leads to a stable crack propagation. Three different types of samples were tested:

- with an initial crack of $60mm$, referred to as *OLCR samples* containing a long FBG of about $25mm$ length
- with an initial crack of $60mm$ and an array of eight FBGs referred to as *multiplexed samples*

- without any sensors and either a $60mm$ initial crack length called *long crack* or a $30mm$ initial crack length called *short crack*

The OLCR and multiplexed samples could be directly compared to each other and to the long crack samples. The short crack samples were tested for comparison to the fatigue data where only the short crack geometry was used.

For the OLCR measurements the sample had to be motionless and therefore the test had to be stopped. The measurements were started after a dwell of one hour which allowed the crack to stabilize and avoided any disturbance. Upon reloading, a slight overshoot of the load eventually occurred. The multiplexed samples as well as the samples without sensors were tested in continuous ramp loading.

5.1.2 Fatigue loading

There is a number of parameters that can affect drastically the outcome of a fatigue test. However, the main goal of the fatigue tests performed in this work was to show that the strain measurement method with multiplexed FBGs can be applied to a moving sample and to compare the fibre bridging in monotonic and fatigue loading. Therefore only one set of testing parameters was used.

To be comparable with the monotonic loading, the crack had to grow over a sufficiently long distance to allow a bridging zone to develop. Therefore, the fatigue tests needed to be performed in load control. In a displacement controlled test, the crack speed typically decreases and the propagation eventually even stops. Compared to this, in a load controlled test, the crack driving force increases with increasing crack length before it becomes critical and the sample breaks.

The ratio of minimal to maximal load was chosen $R = 0.5$. At this ratio, the crack remains sufficiently open so that the bridging fibres are not crushed. At the same time the test is severe enough to cause rapid crack propagation. Note that this parameter has not been changed or further investigated.

The frequency of test was set to $1Hz$. A higher frequency did not allow an accurate control of the loading during the whole test. The reason for this was that the compliance of the sample was changing by one order of magnitude during the test. The stability of the system was thus easier to maintain at lower frequencies.

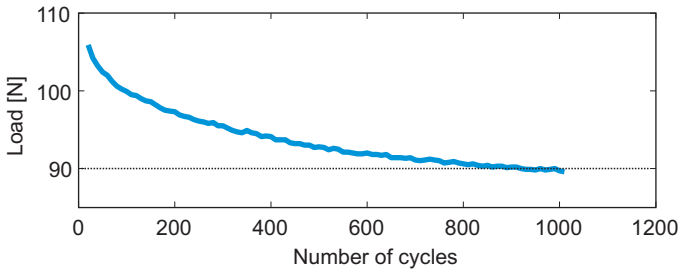

Figure 5.3: Decrease of the load during the first 1000 cycles of a displacement controlled fatigue test.

The maximum load was determined by a pilot test. This test was conducted in displacement control with $R = 0.5$ and a maximum displacement corresponding to the displacement at crack initiation of a monotonic test. The sample was then fatigued for one thousand cycles. Clearly, the crack driving force was just about critical at the beginning but decreased as the crack grew. When looking at the maximum load versus number of cycles shown in Figure 5.3 one can see a rapid decrease to an almost horizontal line. Based on these results the maximum load for the load controlled test was chosen at 80% of the displacement at crack initiation in the monotonic loading. This value was determined by a monotonic loading up to crack initiation for each fatigue test sample. The initial loading had also the advantage to start fatigue at a natually sharp crack.

5.2 Mechanical test results

In this section the results of the monotonic and fatigue test are shown. The results of the strain measurements with the FBGs are reported in Section 5.3.

5.2.1 Monotonic loading

During the tests, load and displacement were recorded with a rate of $10Hz$. Additionally grey scale images of the crack tip were acquired approximatively every $2s$ and the exact time of the acquisition was stored. From these data the crack length, load, and displacement at every millimetre of crack advance were determined. The measured crack length data and the corresponding load and

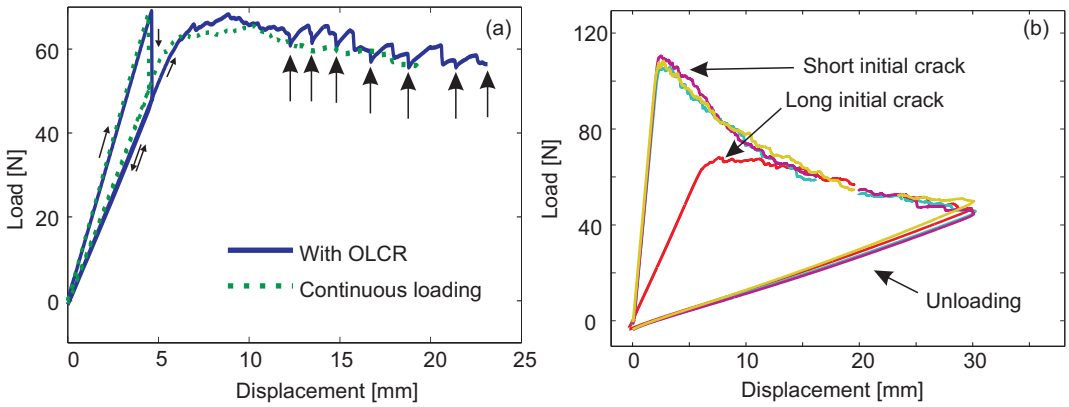

Figure 5.4: Experimental load-displacement curves for DCB tests. (a) for an OLCR specimen with the loading interruptions marked by arrows and (b) with short and long initial crack lengths.

displacement were used to find the fitting parameters as described by Equation 3.1. With the obtained fitting parameters the crack length corresponding to each load and displacement was then calculated.

Figure 5.4(a) shows the load displacement curve of an OLCR sample and for comparison of a sample with a long initial crack without sensor which was continuously loaded. At the beginning, one can see the initial jump of the crack upon which the samples were unloaded and reloaded. The OLCR sample was stopped at seven different crack length positions, marked with arrows, to measure the local Bragg wavelength. One can see that the curve of the OLCR sample fluctuates around the one of the continuously loaded sample when the loading was stopped. Otherwise, the difference between the two curves is very small.

A comparison of load displacement curves for samples with long and short initial cracks is shown in Figure 5.4(b). For clarity the initial crack jump has been omitted. The short crack samples have initially a much higher stiffness. However, when the crack has propagated sufficiently, the two sets of curves overlap. This means that all samples could reach the same stiffness independently of the initial crack length provided the crack had grown long enough.

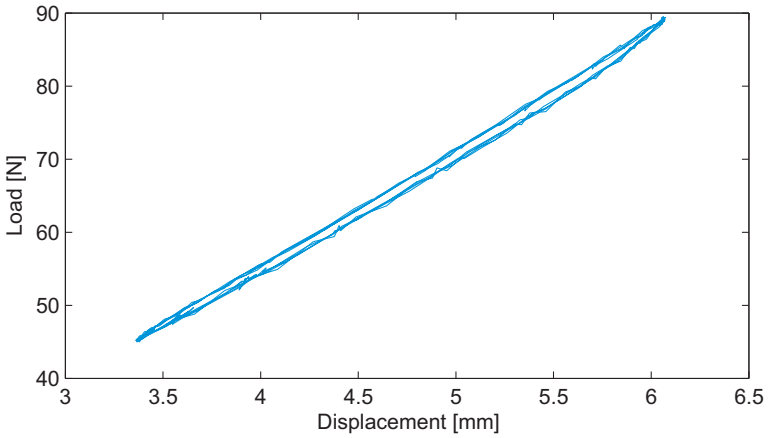

Figure 5.5: Load displacements hysteresis at around 77'000 cycles.

5.2.2 Fatigue loading

The fatigue tests were performed on short crack samples and short crack multiplexed samples and took between 80′000 and 160′000 cycles to finish. At the end of the test, the crack propagation speed had reached about a millimetre per cycle. During the tests, the load and displacement were acquired every tenth cycle during a whole period with a resolution of 100 points. The advantage of such an acquisition is that it allows to observe the hysteresis of the load displacement curve. A large hysteresis would indicate that considerable energy is dissipated. Since this may rise the temperature of the samples it would also affect the reflection peak of the embedded FBGs according to Equation 3.4. Figure 5.5 shows several hysteresis loops after about 77′000 cycles. One can see that the sample behaved linear elastic and almost no energy was dissipated despite the large displacements.

The maximum load and displacement were extracted from the measured data. The crack length was measured on pictures taken every 10 cycles at maximum load using the graduation on the surface of the specimens. Then, the fitting parameters for Equation 3.1 were determined. Using these parameters the crack length was calculated for all load displacement data and was thus known for every tenth cycle as shown in Figure 5.6. One can clearly distinguish three phases during the crack propagation characterised by different slopes of the curve corresponding to the crack speed. In phase (I) the crack speed decreases and reaches the constant

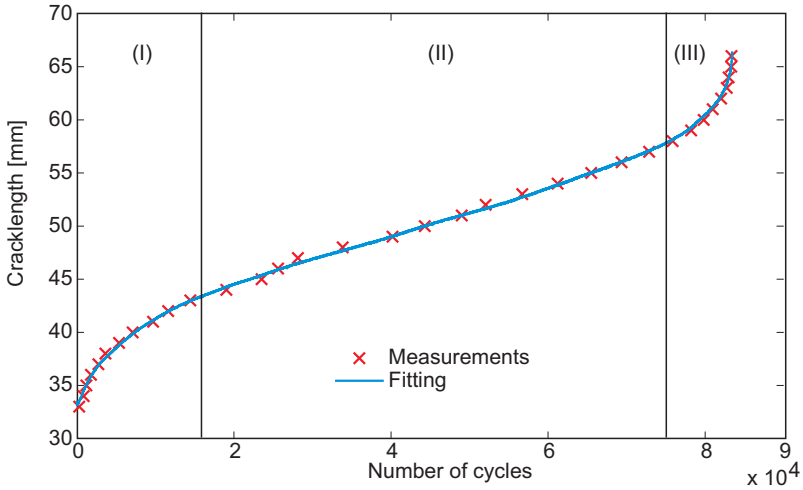

Figure 5.6: Evolution of crack length during the fatigue test. Three phases can be distinguished: (I) An initial decrease of the crack speed (II) a constant crack speed (III) an increase of the crack speed

propagation speed in phase (II). This constant propagation speed lasts for about 2/3 of the total test. Then the crack speed increases in phase (III) until the final failure of the sample is reached.

The energy release rate was obtained by derivation of the analytical form of the crack length versus compliance curve with respect to the crack length and using Equation 3.16. The obtained results from different tests are shown in Figure 5.7 where the same three phases as in Figure 5.6 can be distinguished.

A similar initial decrease of crack speed as observed in phase (I) was reported for another geometry and a different material which also shows fibre bridging [103]. This behaviour is attributed to the development of the fibre bridging zone. Actually, the crack speed is expected to increase with growing crack length because the crack driving force increases. However, at the beginning of the test, the crack front is located at the end of the PTFE insert and no fibre bridging is present. When the crack grows, the bridging zone develops and the resistance of the material towards crack propagation increases. Thus, the crack speed decreases. In phase (II) the increased resistance due to additional bridging is counterbalanced by the increase of crack driving force and the crack speed is approximatively constant. In the last phase (III) the contribution of additional

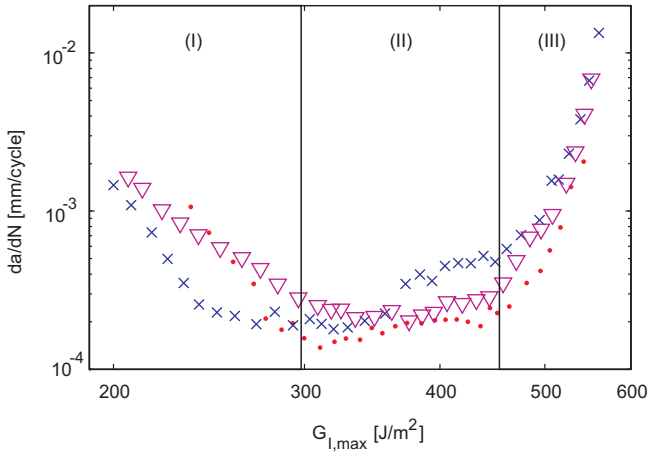

Figure 5.7: Evolution of crack speed for three DCB fatigue tests. The same three phases as in Figure 5.6 can be distinguished.

bridging is marginal and the increasing crack driving force leads to higher crack speed and eventual fracture of the specimen.

Clearly, it would be of great interest to investigate if fibre bridging can lead to an arrest of the crack. However, this would have been beyond the scope of this work and no effort in this direction was undertaken. The results showed that fibre bridging has a considerable influence on the crack propagation and it is important to keep this in mind when dealing with DCB fatigue tests of material where bridging can occur.

5.3 Strain measurements

The results from a DCB test are usually load, displacement and crack length. This is sufficient to calculate the ERR. In this work, however, the embedded FBG sensors were used to measure additional data which served then to identify further material properties, namely fibre bridging tractions. The FBG zone was placed such that the strain distribution $\varepsilon_z(z)$ in the close vicinity of the crack tip and in the bridging zone could be measured.

While the OLCR based method allowed to measure the strain distribution with a spatial resolution of $20\mu m$ along the $25mm$ long FBG, the multiplexed method resulted in a point-wise strain distribution. However, by post-treating the

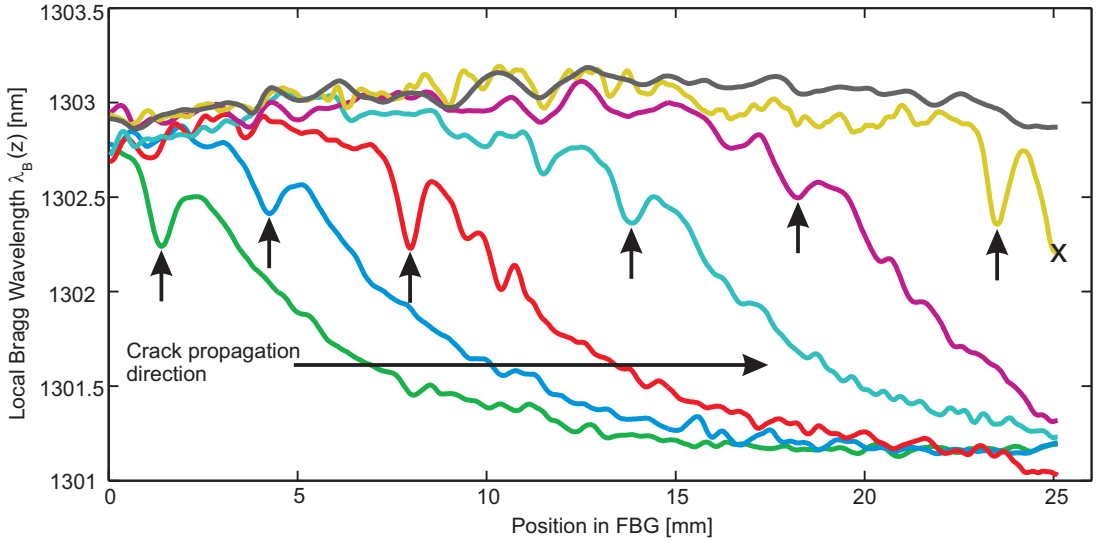

Figure 5.8: OLCR-Measurements of local Bragg wavelengths at seven different crack lengths. The arrows indicate the crack tip position. The curve which was used for the identification is marked with 'x'.

data, a continuous curve could be obtained as well. The main difference between the two methods was the acquisition speed. For the OLCR based method the loading of the sample had to be interrupted and a small decrease of the load was observed during the dwell. This led to a decrease of the stress concentration at the crack tip and thus to a change in the strain distribution. Contrary to this, the multiplexed method allowed for continuous loading, and the strain distribution was measured around a sharp crack. The strain distributions measured with these two methods are shown in the following subsections.

5.3.1 OLCR based measurements

Before starting the tests with the OLCR samples, the precise location of the FBG in the specimen was determined and marked on the surface. The crack was then propagated until it reached this marking. Because of the bowed crack front, the crack length at the surface was about $3mm$ shorter than in the centre of the specimen where the fibre sensor was placed. After the dwell and the OLCR measurement the loading was continued. Once the crack had propagated about $5mm$ the procedure was repeated.

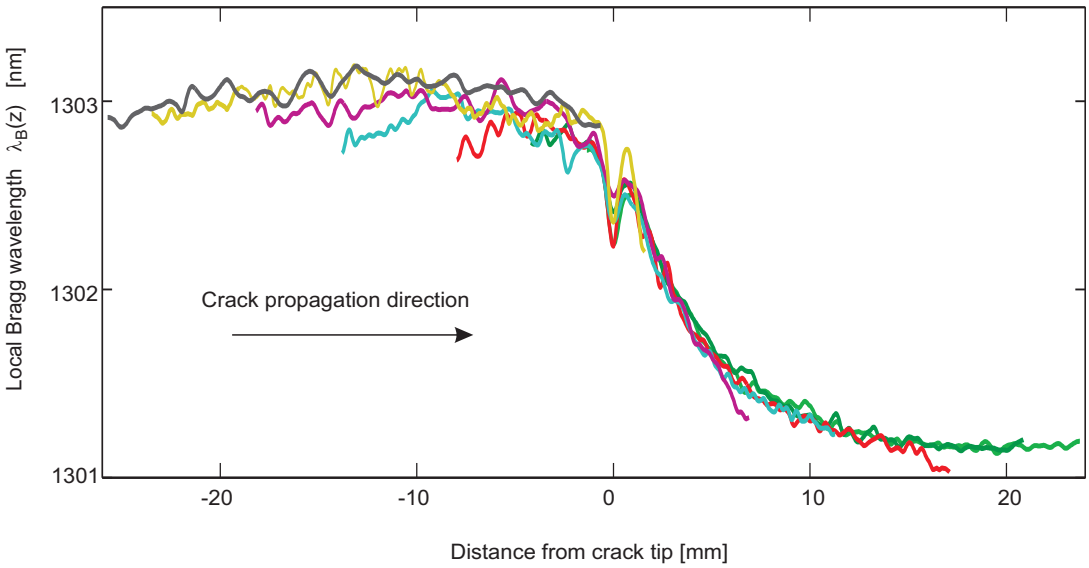

Figure 5.9: The distributions from Figure 5.8 were shifted to have the crack tip coinciding tip.

Figure 5.8 shows measured local Bragg wavelengths (LBW) for the same sample at seven different crack lengths. The crack grew from the left to the right and the arrows indicate the crack tip position for each curve. Ahead of the crack tip (to the right), the LBW decreases and reaches a plateau value after about $15mm$. This plateau value corresponds to the LBW of the unstrained embedded FBG. The crack tip is marked by a characteristic v-shaped dip in the curve as confirmed by FE-modelling. Behind the crack tip (to the left), the LBW decreases slowly. The curvature of this part of the curve indicates the presence of bridging tractions since for a clamped beam, the curve would decrease in a straight line.

Figure 5.9 shows the seven curves from Figure 5.8 where each curve has been shifted to obtain a coinciding crack tip position. It can be seen that the curves superimpose very well ahead of the crack tip which shows that there the strain field is not only self-similar, but independent of the crack length. In the bridging zone behind the crack tip the curves do not superimpose as well. One can also observe that they change slightly their shape. This is due to the change in bending moment as the crack becomes longer and because the fibre bridging zone is changing.

Any of the seven curves in Figure 5.8 could be used as input for the identification of the bridging tractions. However, the best curve was the second last which is marked with a 'x' at the beginning since most of the FBG was in the bridging zone i.e. behind the crack tip. Note that, the v-shaped dip of the crack tip allowed for a precise measurement of the crack length.

5.3.2 Multiplexed sensors

The evolution of the strain as a function of crack length for each sensor of an array with eight FBGs is shown in Figure 5.10 for (a) a monotonic loaded DCB test and (b) a fatigue loaded DCB test. Note that the scale of the crack length is different for the two figures.

In both cases the evolution of the strain is very similar. When the crack approaches an FBG sensor, the strain raises. A v-shaped dip (indicated with an arrow) appears when the crack tip is at the position of the considered FBG in the sample. Behind the crack tip, the evolution of strain depends on the loading condition (monotonic or fatigue) and on the crack length. In the monotonic loading the strain first increases and then decreases linearly. The shape of the curve changes from one FBG to the next for two reasons: i) the bridging changes and ii) the bending moment and thus the curvature of the beam changes. In the case of fatigue, the strain does not decrease which is due to the fact that the test was performed under load control.

The strain distributions for the identification were obtained from these measurements following the data reduction method described in Section 3.2.2 and are shown in Figure 5.11. In comparison with the OLCR measurements, the strain distributions from the multiplexed method have much less noise and extend over a longer distance which improved the identification. However, as pointed out earlier, measurements from different crack lengths were combined to create these distributions with the assumption that the bending moment does not change much for the considered variation of crack length. The calculation of the bending moment for a crack length variation of $\pm 2mm$ revealed a change of $\pm 0.5\%$ for the monotonic tests and of $\pm 3\%$ for the fatigue tests. The difference is due to the fact that load remained constant during crack propagation in the fatigue test (load

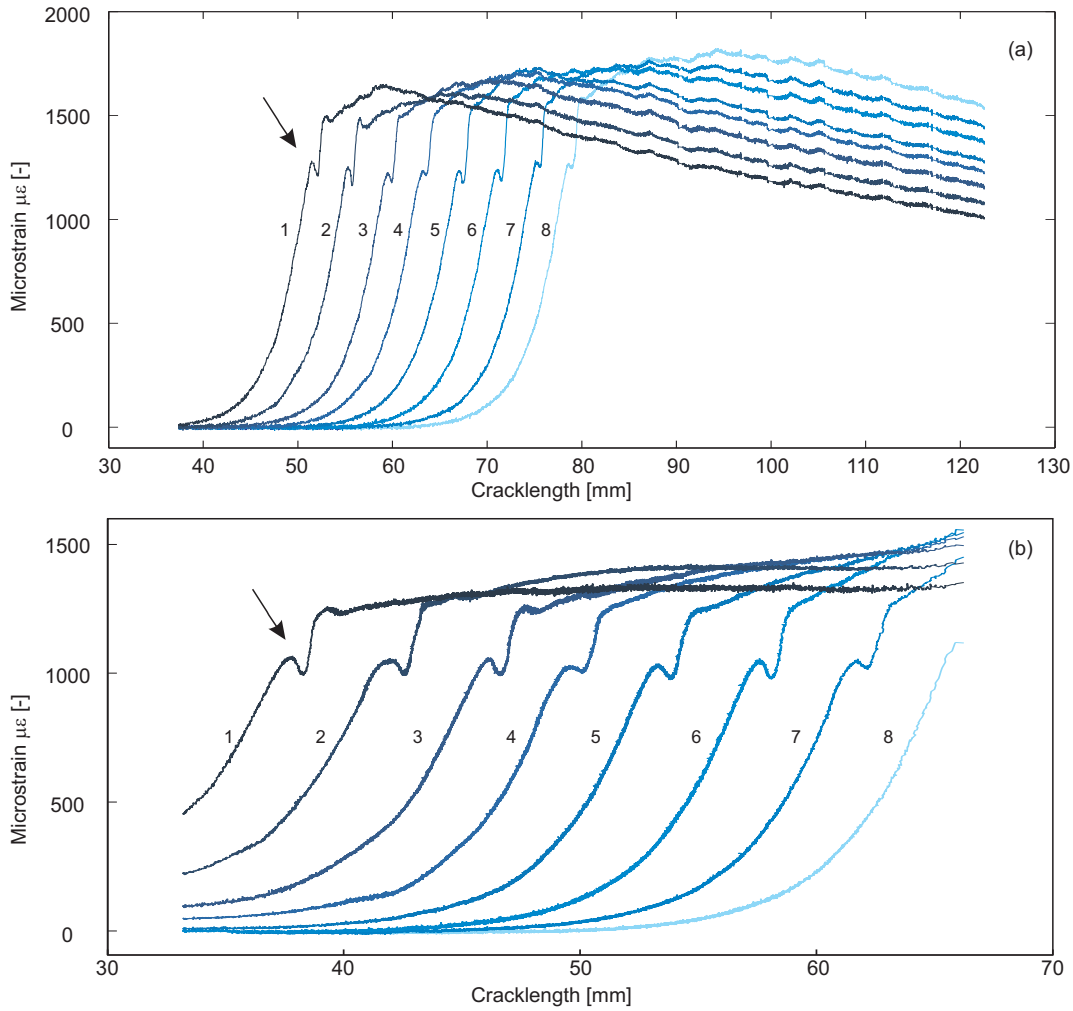

Figure 5.10: Evolution of strain with increasing crack length for (a) monotonic loading and (b) fatigue loading. The arrow indicates the crack tip.

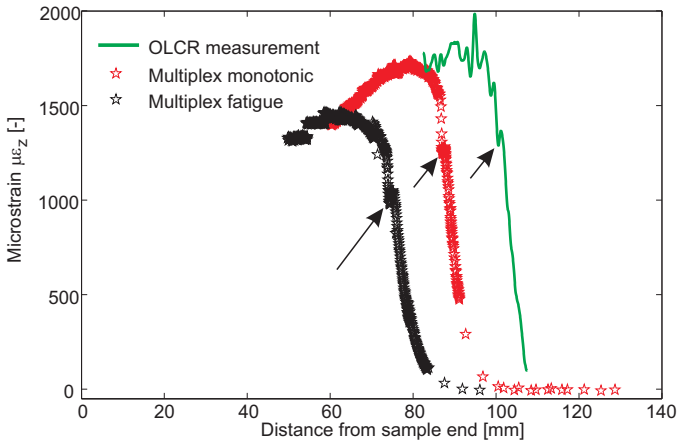

Figure 5.11: Strain distribution measured with the FBG sensors. The crack tips are indicated with arrows.

controlled) whereas it decreased in the monotonic test (displacement controlled) and the considered crack length was longer for the monotonic test which further reduced the relative error. As can be seen in Figure 5.11 this variation of the bending moment led to discontinuities in the strain distribution of the fatigue test.

5.4 Numerical modelling

Two different numerical models were used to analyse the DCB tests. In the first model, the upper part of the DCB specimen was simulated and tractions were applied to the crack surfaces to account for the bridging tractions. This model served to identify the bridging traction distribution. In a second model, the complete DCB sample was simulated. The two arms were connected with a layer of cohesive elements that allowed the crack to propagate. This model was only used to simulate the monotonic loading and allowed to check the identified bridging law.

5.4.1 Identification of bridging tractions

The bridging traction distribution was identified following the method described in section 3.3.1. Based on the findings in Chapter 4 a 2D model with plain

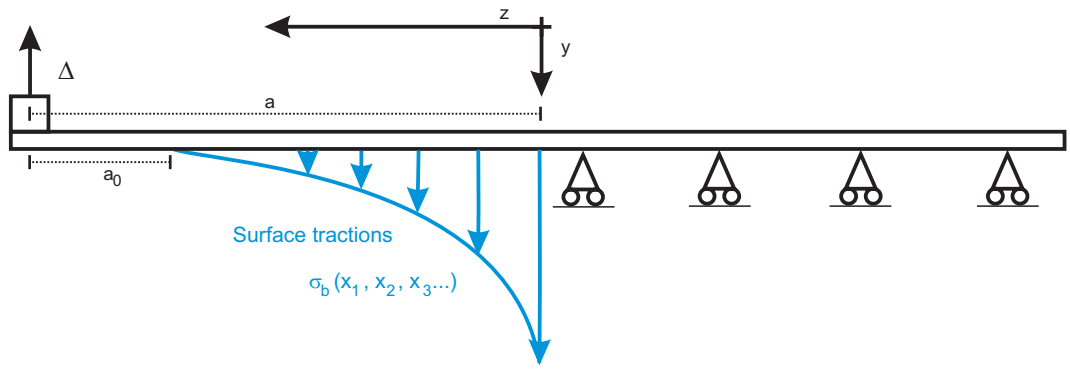

Figure 5.12: Model for identification of the bridging tractions.

strain quadratic elements (Abaqus CPE8R) of the upper half of the DCB sample was created. A $1/\sqrt{r}$ singularity was created at the crack tip by collapsing the neighbouring elements to triangles and shifting the mid-nodes to one quarter of the edge length.

The bridging tractions were simulated by surface tractions applied between the crack tip and the crack initiator a_0 as indicated in Figure 5.12. They were directed in the y-direction (closing direction of the crack) throughout the simulation. This guaranteed that only closing forces were applied. The amplitude of the surface tractions along the crack was determined by an analytical expression defined by parameters $(x_1, x_2, x_3 \ldots)$. The details of the different models are given in the next subsection 5.4.2.

Since this model was used together with the experimentally determined strain distribution, the geometry had to match the one of the experiment as close as possible, namely, the crack length a, the imposed displacement δ, the thickness, the width, and the position of the fibre sensor. A micrograph, as shown in Figure 3.3, was produced for each tested specimen to measure the distance of the fibre sensor to the crack plane.

Figure 5.13 shows the results of the identification. Clearly, the strain distributions from the models with the optimised surface tractions show a very good agreement with the measured curves. For comparison, the strain distribution of the same model as used for the identification of the monotonic bridging tractions but without surface tractions is shown as a dashed line. Note here the large influence of the surface tractions on the strain, especially close to the crack tip.

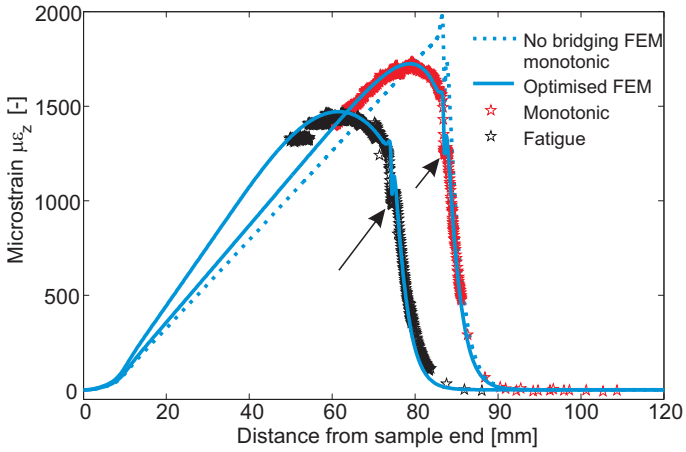

Figure 5.13: Measured and optimised strain distributions for monotonic and fatigue loaded DCB tests. The dashed line shows the strain distribution in a model without surface tractions

5.4.2 Model for bridging distribution

Fibre bridging consists of individual fibres or fibre bundles that connect the two crack surfaces. However, the simulation of individual fibres was not considered a reasonable approach. Instead, a surface traction distribution in the bridging zone was assumed where an analytical curve was used to calculate the amplitude of the traction as a function of position. A priori, this distribution could be of any form, however, some physical considerations helped to chose it:

- The maximum of the bridging tractions occurs at the crack tip or near.
- The amplitude of the bridging tractions is smaller than the tensile strength of the matrix, otherwise the crack would not propagate.
- The tractions decrease to zero at the end of the fully developed bridging zone.
- The bridging zone is limited by the crack tip and the PTFE insert.
- The decrease is monotonic.

Based on these requirements, three different shapes were studied for the optimisation of the bridging tractions: linear, bilinear, and exponential decrease.

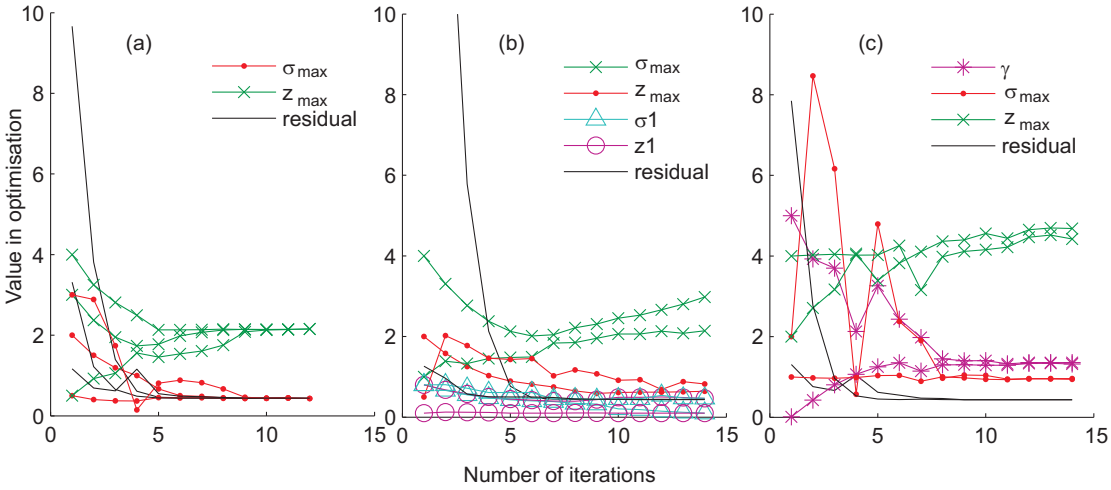

Figure 5.14: Convergence of the different bridging models. (a) linear decrease (b) bilinear decrease (c) exponential decrease. The different values were set to be as close as possible to one in the optimisation the displayed values are only qualitative.

The simplest model was the linear decrease given by:

$$\sigma_b(z) = \sigma_{max} - \frac{\sigma_{max}}{z_{max}} z \quad , \qquad 0 \leq z \leq z_{max} \tag{5.1}$$

where σ_{max} is the maximum bridging traction at the crack tip and z_{max} is the length of the bridging zone. This model showed very good robustness, which means it converged very rapidly and for a wide range of initial values as can be seen in Figure 5.14(a). However, its simple shape was not capable to match at the same time the rapid decrease and long extent of the bridging traction distribution.

A more versatile model was a bilinear distribution given by Equations 5.2. This distribution had two slopes defined by the point (z_1, σ_1) where the slopes change, as well as the maximum bridging traction at the crack tip σ_{max} and the bridging zone length z_{max}.

$$\sigma_b(z) = \sigma_{max} - \frac{\sigma_{max} - \sigma_1}{z_1} z \quad , \qquad 0 \leq z \leq z_1 \tag{5.2a}$$

$$\sigma_b(z) = \sigma_{max} - \frac{\sigma_1}{z_{max} - z_1} z \quad , \qquad z_1 \leq z \leq z_{max} \tag{5.2b}$$

The convergence of such a model is shown in Figure 5.14(b). Compared to the linear model it converged much slower and despite a small residual, there was

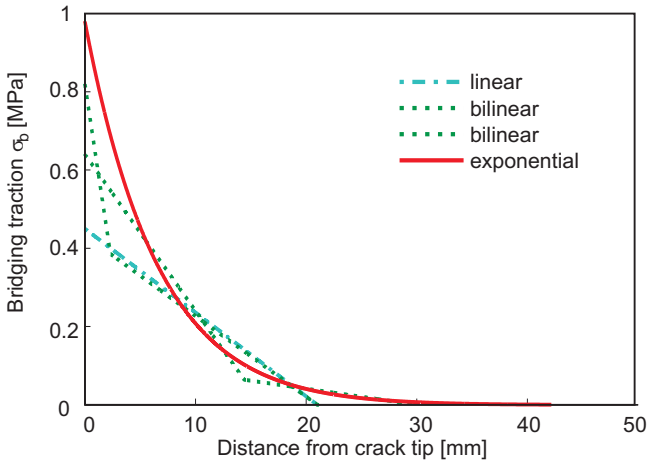

Figure 5.15: Identified bridging traction distribution for different bridging models using OLCR measurements as input for the identification.

no unique solution. The optimisation showed that there were two local minima as can be seen in Figure 5.15. In one case, the initial slope was very steep and the second slope was identical to the one of the linear model. In the other case the initial slope was less steep and the the second linear part extended to about $30mm$.

Clearly, a model which yields several local minima is not a good choice for an optimisation. The bilinear model has shown, however, that the initial decrease is very steep and the extent of the bridging zone quite long. To achieve such a behaviour but with a unique solution, a combination of an exponential and a linear decrease as proposed in literature [3] was used:

$$\sigma_b(z) = e^{-\gamma z}\left(\sigma_{max} - \frac{\sigma_{max}}{z_{max}}z\right) \quad , \qquad 0 \leq z \leq z_{max} \tag{5.3}$$

where γ is a parameter taking into account the non-linearity of the decrease. This model allowed for a distribution with a rapid initial decrease and a long bridging zone at the same time. The convergence was good as can be seen in Figure 5.14(c) except for the length of the bridging zone z_{max}. Since the tractions are tending to zero at the end of the bridging zone, the influence of this parameter on the error vector was not big enough to be precisely determined.

Comparing the bridging traction distributions shown in Figure 5.15 one can see that the linear model results in a distribution that is intermediate between

rapid initial decrease and long extent of the bridging zone. The two solutions for the bilinear model follow either the initial or final part of the exponential model and the exponential model behaves like a combination of the two solutions of the bilinear model but with a unique solution. It was thus considered being best suited to simulate the bridging traction distribution.

5.4.3 Bridging law

The bridging traction distribution $\sigma_b(z)$ as it was identified was not very useful for subsequent analysis. It depends on the length of the crack and the thickness of the sample since these parameters change the curvature of the delaminated cantilever arm. A description of the bridging tractions which is independent of the geometry of the sample is a traction separation law $\sigma_b(\delta)$. This so called *bridging law* gives the bridging tractions as a function of crack opening δ. By integrating the bridging law the ERR which is associated to the fibre bridging is obtained as shown in Equation 3.18.

The bridging law was obtained by two methods: i) by identification using the measured strain distribution and ii) from measurements of the crack opening displacement (COD). In the first method, the displacement along the crack surface of a simulation with optimised surface tractions was extracted. Then, for each opening displacement the corresponding bridging traction was calculated using the identified parameters. The second method consisted in measuring the COD at the end of the bridging zone. Then the ERR was derived with respect to the COD following Equation 3.19 to obtain the bridging law. Figure 5.16 shows the bridging laws obtained from the three different models for the bridging traction distribution. For comparison the bridging law obtained with the COD measurement is shown as well. All the experimental data came from OLCR specimens.

The bridging law based on the exponential model and the COD based bridging law are very similar. It should be noted, however, that the COD measurements are difficult especially for small crack openings. Therefore, the bridging law derived from such measurements is not very accurate at the beginning. In contrast, the bridging tractions close to the crack tip have the strongest influence on the strain

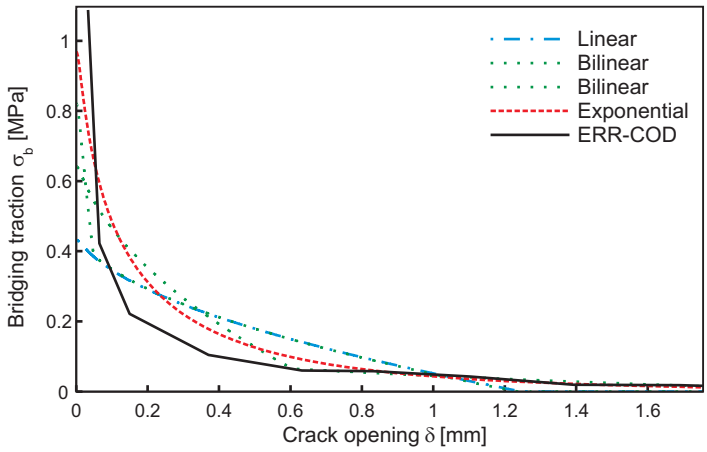

Figure 5.16: Bridging laws identified from OLCR measurements and with different models of bridging distribution.

Model	linear[(a)]	bilinear[(a)]	exponential[(a)]
G^b $[J/m^2]$	200	211/222	230
Test/method	COD-ERR[(a)]	Multiplexed[(b)]	Fatigue[(b)]
G^b $[J/m^2]$	220	350	450

Table 5.1: Energy release rate of the bridging fibres. For (a) OLCR measurements were used and for (b) measurements from multiplexed sensors were used with an exponential model. Both solutions are given for the bilinear model.

distribution measured with the sensor fibres. The identified law is therefore more accurate at the beginning than towards the end.

The energy release rate associated to the fibre bridging G^b was obtained by integrating the bridging law as shown by Equation 3.18. Table 5.1 summarises these results for the different models of the surface traction distribution. Additionally, the ERR calculated from the identified bridging laws of the multiplexed and fatigue samples are reported.

The ERR for the different models are quite similar. However, there is a big difference between results from the OLCR samples and those from the multiplex samples (which were identified with an exponential model). This is due to the difference in loading history. This is, the OLCR samples had to be stopped for the measurements, while the multiplex samples were continuously loaded.

Sample	$\sigma_{max}[MPa]$	$z_{max}[mm]$	$\gamma[-]$	crack length [mm]
OLCR	0.95	45	0.13	106
Multiplex	1.38	43	0.128	90
Fatigue	0.3	40	0.01	75

Table 5.2: Identified parameters for the exponential bridging traction distributions and crack length of the considered sample.

The identified parameters of the exponential surface traction distributions for OLCR, multiplex and fatigue tests are shown in Table 5.2. One can see that the maximum traction at the crack tip σ_{max} is bigger for the multiplex sample than for the OLCR sample. This confirms that the difference in ERR is caused by the relaxation of parts of the bridging tractions in the OLCR samples.

When comparing the multiplex and the fatigue test, one can see that the identified ERR is about 30% higher for the fatigue test. Also, the decrease of the bridging tractions is much slower (small γ) and the maximum traction at the crack tip is lower. Because of the smaller tractions, there might be less fibre breaking and thus a higher number of bridging fibres which cause the higher ERR. However, more experimental results are needed to confirm this hypothesis.

5.4.4 Cohesive element simulation

The identified bridging law from the multiplex sample was used in a numerical model to simulate the load-displacement curve. For this, the bridging law was implemented as material property of a cohesive element layer that connected the two arms of a DCB specimen. Then, the load displacement curves from the simulation and the experiment were compared.

The material behaviour of cohesive elements, the *cohesive law*, was described in Subsection 3.3.2. In the case of a DCB test it had to account for two fracture processes: i) the fracture of the matrix or interface at the crack tip and creation of the new surface with its associated energy release rate G_I^i corresponding to the ERR at the crack initiation when no bridging tractions are present and ii) the fibre bridging with an ERR of G_I^b. To obtain this behaviour, the identified bridging law $\sigma_b(\delta)$ was appended to a cohesive law with a linear decrease of stiffness. For

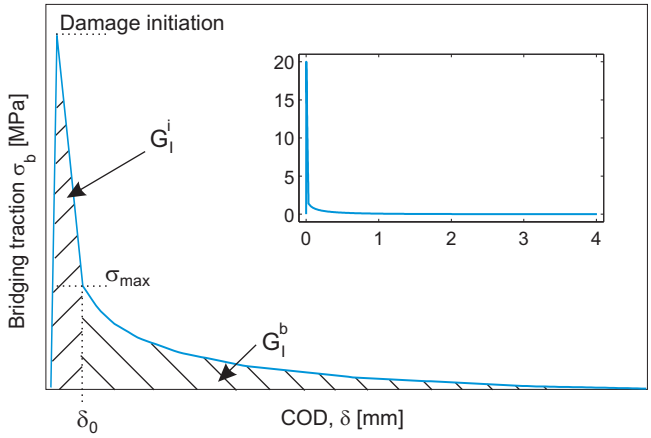

Figure 5.17: Cohesive law for mode I delamination; the insert shows the law to scale.

an exponential decrease only a very small difference resulted. Figure 5.17 shows a schematic of such a cohesive law accounting for the two fracture processes. The insert gives the cohesive law to scale as it was used in the simulations.

While the part of the cohesive law which accounted for the bridging was identified, several parameters in the initial part had to be estimated. Keeping the area under the curve (and thus the ERR) constant at $G_I^i = 350 J/m^2$, the following parameters were chosen: The opening at the end of the initial part δ_0 was taken as $20 \mu m$ corresponding to the thickness of the cohesive element layer. For the damage initiation criterion a value of $\sigma = 20 MPa$ was used. Several other values were tested with almost identical results but a less rapid convergence. The initial cohesive stiffness of the elements was $9000 GPa/mm$. With this value the damage initiated at about one tenth of the opening at the end of the initial part δ_0. The cohesive law was inserted in tabular form using a displacement controlled damage evolution. At least 300 points were used to guarantee the accuracy of the results. Round-off and interpolation errors were observed with less points.

The numerical model consisted of the two arms of the DCB specimen, each discretised with 16000 plane strain eight-node quadratic elements (Abaqus CPE8R), and a $20 \mu m$ thick layer of 6000 linear cohesive elements (Abaqus COH2D4) which was tied to the two arms. The geometry of the arms and the initial crack length were taken from the actual values of the experiments. Then, an opening dis-

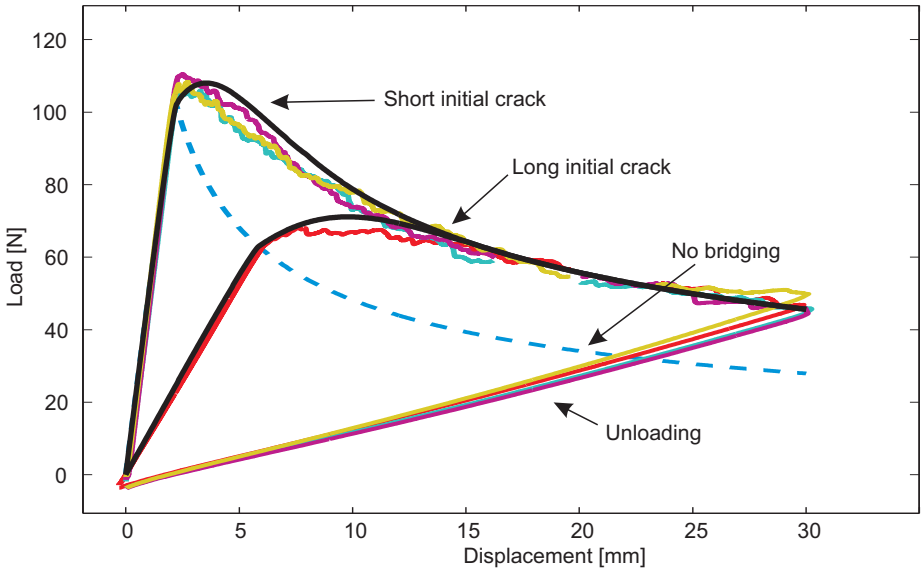

Figure 5.18: Simulated (solid black) and experimental load displacement curves. The load displacement curve of a simulation without fibre bridging is shown as dashed line.

placement of $15mm$ was applied to each of the arms and the model was solved in 500 time steps. The traction separation curve was then extracted from a single cohesive element to verify that it corresponded to the imposed cohesive law.

Figure 5.18 shows the load displacement curves that were extracted from the cohesive element models (thick black lines) for long and short initial crack lengths. The experimental curves from Figure 5.4 (b) are shown for comparison. There is an excellent match between the experiment and the simulation for both, the crack initiation and the crack propagation. The dashed curve indicated with *no bridging* shows the load displacement curve of a model where the cohesive law consisted only of the first (linear) part. This simulation could reproduce the crack initiation, but not the propagation. This shows the importance of the fibre bridging and confirms the correctness of the identified bridging law.

Note that the bridging law was identified at a given crack length. Nevertheless, it can be used to predict the complete load displacement curve. This means that the same cohesive law applies throughout the delamination process and it is independent of the crack length.

5.4.5 Stress intensity factor

Another approach to describe the resistance of a material against fracture is based on the stress intensity factor (SIF) or K. The expression of K depends on the boundary conditions (geometry) of the cracked sample and the loading. When K becomes bigger than a critical value K_c, considered as a material property, the crack propagates. The SIF and the ERR are directly related by [113]:

$$G_i = QK_i^2 \tag{5.4}$$

where K_i is the SIF (i standing for modes I, II and III) and Q is the elastic coefficient defined for orthotropic materials in mode I in plane strain by:

$$Q = \sqrt{\frac{1}{2E_1E_2}}\left[\sqrt{\frac{E_1}{E_2}} + \frac{E_1}{2G} - \nu_{12}\right]^{1/2} \tag{5.5}$$

Because the SIF is derived from the stress field around the crack and the material is supposed linear elastic, the SIF of the same mode from different loads can simply be summed. This is called *principle of superposition*. In the case of the DCB test this means that the SIF from the applied load $K_{I,P}$ can be summed up with the one of the bridging tractions $K_{I,br}$ to obtain the total SIF $K_{I,T}$:

$$K_{I,T} = K_{I,P} - K_{I,br}$$

where the minus is due to the fact that the bridging tractions work in the opposite direction of the loading forces. The obtained $K_{I,T}$ corresponds to the SIF in mode I of a material without fibre bridging.

The stress intensity factor of a DCB specimen subjected to dipole line forces at the crack faces of an orthotropic material was derived by Massabò [47] and is given by the following equation:

$$\begin{aligned} K_{I,P_L} = & \\ & \frac{P_L}{\sqrt{h}}\left\{\frac{\lambda^{-3/8}}{\sqrt{n}}\sqrt{12}\frac{a}{h}\left(1 + Y\lambda^{-1/4}\frac{h}{a}\right) + \sqrt{\frac{2h}{\pi a}} - \right. \\ & \left. - \left[0.815\left(\frac{0.677}{Y}\sqrt{n}\lambda^{1/4}\frac{a}{h}\right)^{0.619}\lambda^{-1/8} + \frac{\sqrt{n}}{\sqrt{12}Y\lambda^{1/8}}\right]^{-1}\right\} \\ & = P_L\phi(a,h) \end{aligned} \tag{5.6}$$

where P_L is the applied line load, a is the distance between the crack tip and the load application point, h is the thickness of one cantilever arm, and Y is given as:

$$Y(\rho) = 0.677 + 0.146(\rho - 1) - 0.0178(\rho - 1)^2 + 0.00242(\rho - 1)^3$$

For plain strain conditions the dimensionless material parameters λ and ρ are derived from the elastic constants of the material as follows:

$$\lambda = \frac{E_3(1 - \nu_{12}\nu_{21})}{E_1(1 - \nu_{23}\nu_{32})},$$
$$\rho = \frac{\sqrt{E_1 E_2}}{2G_{13}\sqrt{(1 - \nu_{12}\nu_{21})(1 - \nu_{23}\nu_{32})}} - \sqrt{\frac{\nu_{13} + \nu_{12}\nu_{23}}{1 - \nu_{12}\nu_{21}} \frac{\nu_{31} + \nu_{32}\nu_{21}}{1 - \nu_{32}\nu_{23}}},$$
$$n = \sqrt{\frac{1 + \rho}{2}}$$

The calculations were applied to the measurements of a multiplexed sample. To determine the SIF due to the applied load, $K_{I,P}$, line load P_L in Equation 5.6 was replaced by the applied load P divided by the width of the sample B and a was the crack length. For the SIF due to the bridging tractions, $K_{I,br}$, the line load P_L was obtained by integrating the bridging tractions over the length of the bridging zone:

$$K_{I,br} = \int_0^{z_{max}} \sigma_b(z)\phi(z, h)\,\mathrm{d}z \tag{5.7}$$

where z was used in stead of a for the distance between the crack tip and the load application point to avoid confusion with the crack length. The bridging traction distribution $\sigma_b(z)$ as obtained from the identification was used.

The total SIF, $K_{I,T}$, was compared at two crack lengths: at crack initiation and at a crack length of $90mm$ which is where the bridging traction distribution was identified. At crack initiation $K_{I,T} = K_{I,P}(a_0) = 2.21\,MPa\sqrt{m}$ was found and for $a = 90mm$ the resulting total SIF was $K_{I,T} = K_{I,P}(a = 90) - K_{I,br} = 2.23\,MPa\sqrt{m}$. This results show that the SIF is constant during crack propagation if one accounts for the bridging tractions. Using Equation 5.4 an ERR of $360J/m^2$ was obtained from the total SIF which corresponds very well to the initiation ERR, G_I^i, found with the compliance based methods.

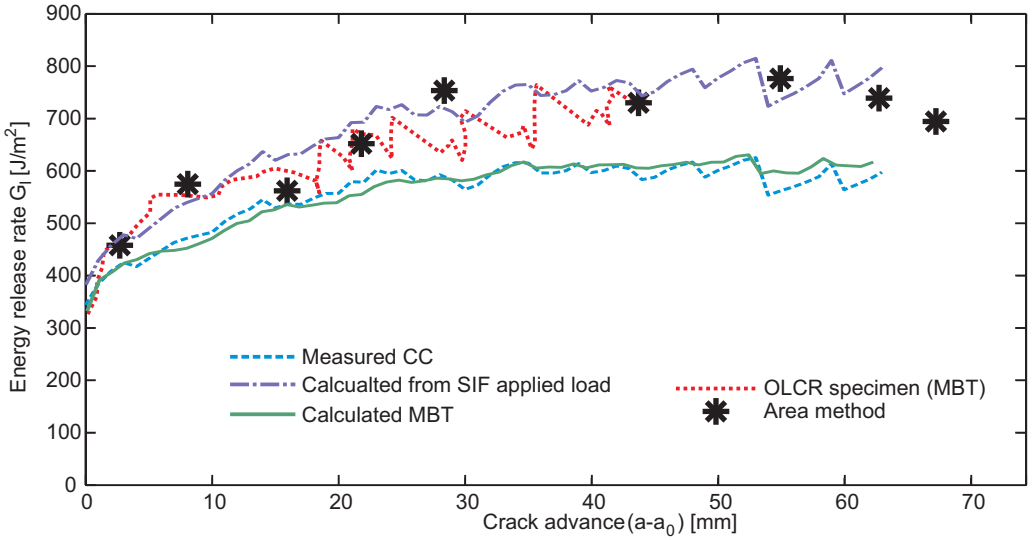

Figure 5.19: Evolution of the ERR with growing crack length calculated with different methods.

5.5 Calculation of the energy release rate

The evolution of the energy release rate during the DCB test was calculated using different methods. The most direct one without hypotheses was the area method, as described in Subsection 3.4.3. A long crack sample without sensor fibre was unloaded and reloaded nine times during the test and the area under the obtained curves was calculated as precisely as possible. The ERR was then calculated with Equation 3.20 and the results are shown in Figure 5.19.

For the compliance method the relationship between the compliance of the DCB specimen and the crack length was determined in two different ways: with the compliance calibration (CC) and with the modified beam theory (MBT). For the CC the fit with Equation 3.15 was used and the expression differentiated with respect to a to obtain the ERR using Equation 3.16. In the case of the MBT, the relationship between the compliance and the crack length is derived from simple beam theory where each arm of the DCB specimen is represented as a cantilever beam. Using the elastic line of the arms, the compliance of the DCB is given as:

$$C = \frac{\delta}{P} = \frac{2}{3}\frac{a^3}{EI} \tag{5.8}$$

with $I = Bh^3/12$ being the moment of inertia and h the thickness of one cantilever beam. Introducing Equation 5.8 into Equation 3.16 the following expressions for the ERR are obtained:

$$G_I = \frac{P^2 a^2}{BEI} \tag{5.9a}$$

$$G_I = \frac{3P\delta}{2ba} \tag{5.9b}$$

$$G_I = \frac{9\delta^2 EI}{4Ba^4} \tag{5.9c}$$

Note that Equation 5.9(a) shows that a load controlled test is unstable since the derivative of the ERR with respect to the crack length is positive (see Equation 3.12), while for the displacement controlled test, expressed by Equation 5.9(c), the derivative is negative and thus the crack propagation is stable.

The beam theory is a simplification and rotations of the beams can occur at the crack front. Therefore a modification of Equation 5.9b is proposed in the standard. For this, the crack length is increased by $|\Delta|$ which is given by the intersection of the x-axis with a linear fit of the cube root of compliance versus crack length such that Equation 5.9(b) becomes:

$$G_I = \frac{3P\delta}{2B\left(a + |\Delta|\right)} \tag{5.10}$$

As can be seen in Figure 5.19 the values obtained using the CC method and the MBT method are very similar. The fact that the OLCR sample has a higher value over the first $20mm$ is due to the longer initial crack length while the propagation value is disturbed by the dwell for the OLCR measurements.

Finally, the ERR was determined with the expression of the SIF of a DCB specimen given in Equation 5.6. The SIF was calculated for each load and corresponding crack length and then transformed into ERR with Equation 5.4.

From the four different methods used to calculate the ERR the area method is the only one that is not using any hypotheses. However, it gives only very few points, it requires unloading and reloading of the specimen during the test, and a very precise measurement of the area and the crack length are required. The results show also an important scatter. Alternatively, the method based on beam theory is very simple to use. However, because it is based on the hypothesis

of cantilever beams, correction factors proposed in the ASTM standard have to be applied to obtain a correct result. Similarly the compliance calibration method is based on an analytical curve fitting the compliance versus crack length curve. Calculating the ERR from the SIF is possible, however, the equations are very complicated and do not take fibre bridging into account. This leads to an overestimation of the ERR.

From the results obtained in Subsection 5.4.5 the evolution of ERR in the bridging fibres and therefore their contribution to the total ERR was determined. For this, Equation 5.7 was evaluated at each crack length and the SIF converted to ERR with Equation 5.4. The bridging traction distribution, $\sigma_b(z)$, was obtained from the identified bridging law and the elastic line of a clamped beam. The length of the bridging zone z_{max} was determined using the maximum opening from the bridging law. Figure 5.20 shows the evolution of the ERR in the bridging fibres for a short and a long initial crack. By subtracting this contribution of the bridging from the ERR calculated with the compliance calibration method, an almost constant ERR is obtained which corresponds to the ERR of the material without bridging. A very similar result was obtained with the direct calculation from the total SIF.

Summary

Mode I delamination was analysed with the DCB test. Due to the embedded FBG sensors, not only load, displacement, and crack length were monitored during the test, but also the strain distribution close to the crack tip. With these measurements, the bridging traction distribution was identified. An exponential model was found to be best suited to describe this distribution analytically.

The stress intensity factor of a DCB test was then calculated taking the fibre bridging into account. For this, the identified bridging traction distribution was used to correct the SIF using the principle of superposition. This analysis showed that the stress intensity factor in a DCB test is constant if one corrects for the bridging tractions.

By combining the bridging traction distribution with the crack opening displacement the bridging law was obtained. The integration of the complete bridg-

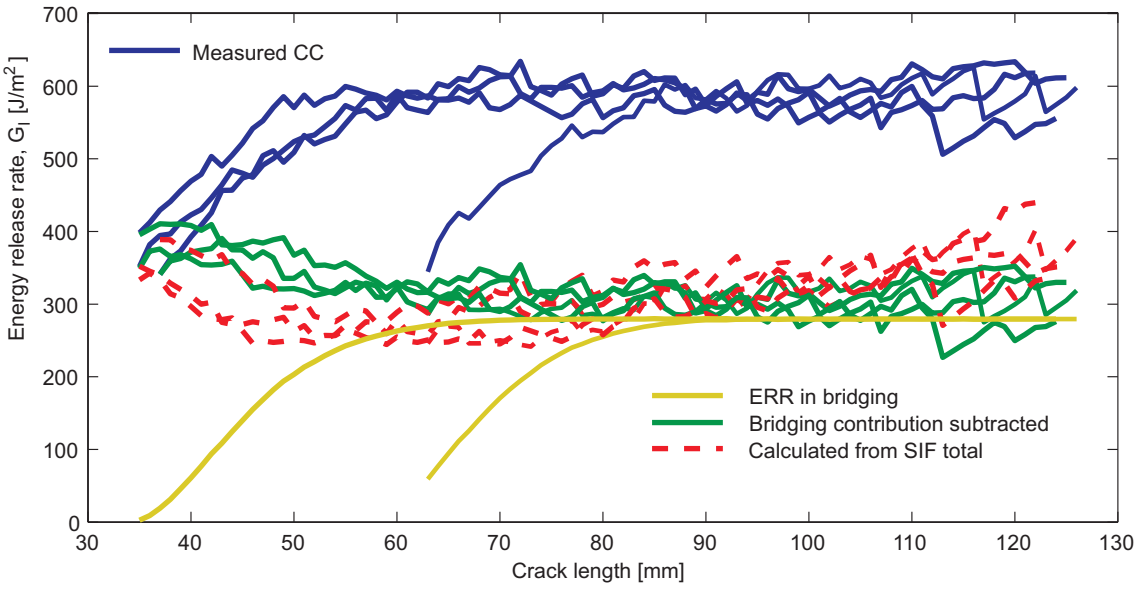

Figure 5.20: Energy release rate as a function of crack length determined with the compliance calibration method and when fibre bridging tractions are taken into account.

ing law gives the ERR due to the bridging fibres. The calculations showed that the energy release rate that is attributed to the bridging fibres corresponds to about half the total ERR for this material. Further, the bridging law was used in a cohesive element model and allowed to reproduce the complete load displacement curve of a DCB test.

Finally, the DCB samples were tested in fatigue and the strain distribution measured with multiplexed FBG sensors. These measurements shed some light on the importance of the bridging fibres in fatigue. The ERR associated to them was found to be about 30% higher than in the monotonic test and they were influencing the crack speed.

Chapter 6

Mode II delamination

Mode II delamination was studied in a similar way as mode I delamination with embedded FBG sensors. However, fibre bridging was not found to be present. Therefore the measured strain distribution was used to identify friction and the energy release rate. In the beginning of the chapter the test set-up is described. Then, the results of the tests, the strain measurements and the numerical simulations are discussed.

6.1 Test set-up

A four point end notched flexure test (4ENF) set-up was used to study mode II delamination of the composite. The advantage of the 4ENF test compared to other mode II tests is the long zone where the crack propagation is stable which allowed for strain measurements with the FBGs. As long as the crack is between the two upper rollers (B) and (D) in Figure 6.1, the propagation is stable. When the crack approaches roller (D) it even stops.

The test set-up was very similar to the one used for a four point bending test. However, due to the end notch, the stiffness was not uniform along the sample. To ensure that all four loading pins were subjected to the same load, the beam holding the two upper pins (B) and (D) could rotate at point (C) around an axis in the width direction of the sample. The spans of the test were chosen symmetric which means that the upper span was half the lower span. The distance between

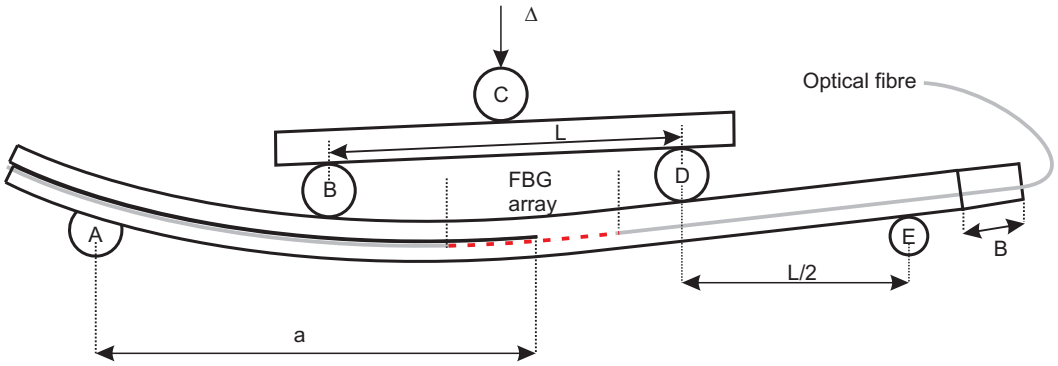

Figure 6.1: Schematic of the 4ENF test set-up. Roller (A) was glued to the surface of the specimen. B is the width of the specimen

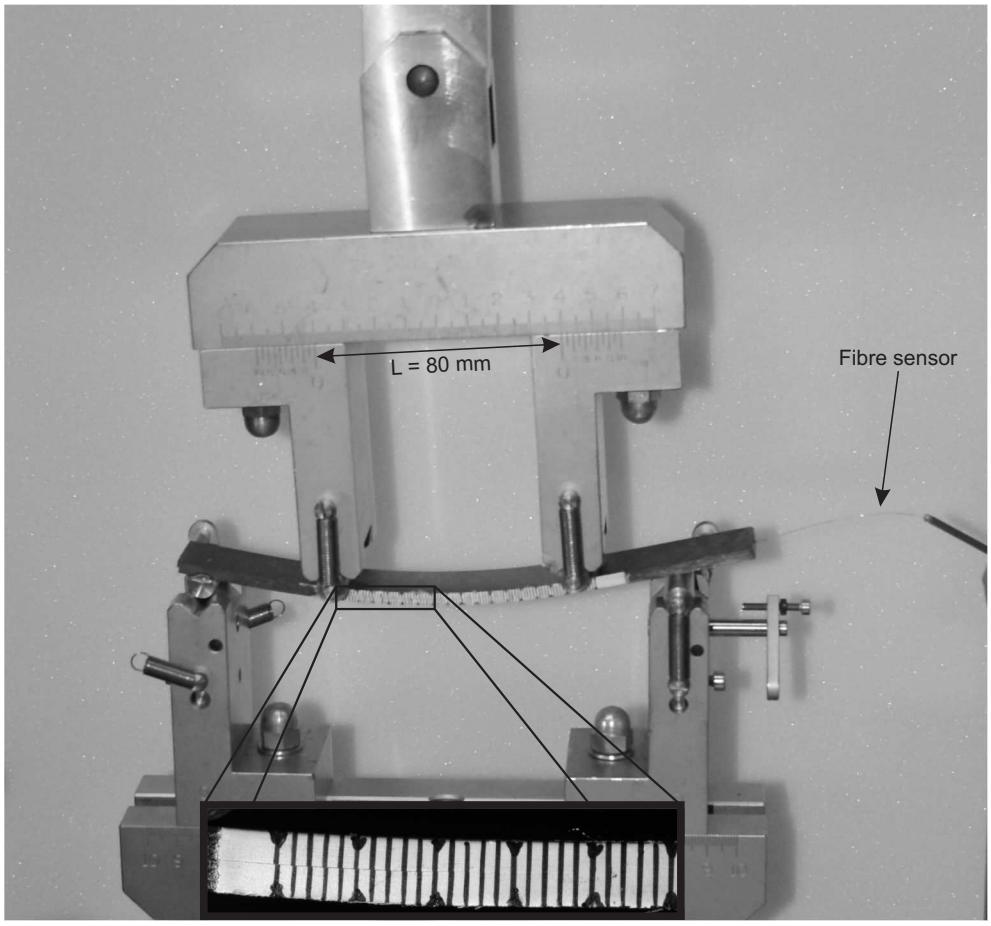

Figure 6.2: Photograph of the 4ENF set-up showing the crack from left to right and a fibre sensor at the right hand side of the specimen.

the upper loading pins L was $80mm$. The sample was placed such that the end of the FBG zone was $10mm$ away from loading pin (D) to avoid its influence.

The crack length was measured from the centre of the lower left pin (A) to the crack tip. The PTFE film which served as crack initiator had a length of $60mm$ so that the initial crack tip was between the loading pins (B) and (D). During the first pilot tests it was observed that the sample was horizontally displaced due to the asymmetric stiffness. Since the crack length is measured with the graduation on the sample itself, such a shift would lead to wrong crack length data. To avoid this, pin (A) was cut two millimetres above the centre and glued to the sample. The loading pin (E) had been reduced to a diameter of $7mm$ to account for the reduced height of the cut pin (A).

As in mode I tests, the sample was loaded with a rate of $0.04mm/s$ until the first crack propagation occurred. This propagation was usually a sudden jump. Then, the sample was unloaded and reloaded at the same rate until the crack had reached loading pin (D) and the load increased. During the whole crack propagation pictures were taken about every two seconds with a CCD camera to monitor crack length. A photograph of the test is shown in Figure 6.2.

Three different types of samples were tested:

- Samples without a fibre sensor.
- Samples with a long FBG interrogated with the OLCR based method (see Subsection 3.2.1).
- Samples with an array of eight multiplexed FBGs (see Subsection 3.2.2).

While the first two samples were continuously loaded, the loading had to be stopped at different crack lengths for the OLCR samples to allow for measurements.

6.2 Mechanical test results

Figure 6.3 shows four load-displacement curves from the 4ENF tests. As for the DCB tests, the crack jumped at the initiation (not shown in the figure) because of the resin rich zone after the PTFE insert and the samples were unloaded and

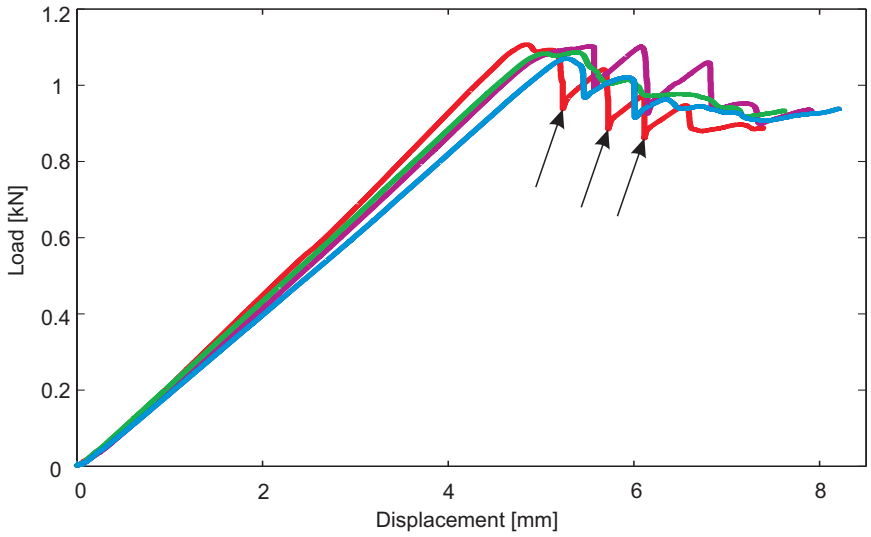

Figure 6.3: Load displacement curves of 4ENF tests. The arrows indicated load drops before OLCR measurements.

reloaded to propagate from a sharp crack tip. The different lengths of the jump caused the variation of the initial slopes.

After crack initiation, the load decreased. Hereby the crack propagation was not always smooth as can be seen by the sudden drops of load leading to a saw-tooth shaped curve which was also observed for continuously loaded samples. The arrows indicate the displacements at which the loading was stopped for the OLCR measurements. During the dwell of one hour the crack continued growing by up to $4mm$ causing a considerable reduction of the load followed by an overshoot upon reloading. When the crack reached the loading pin (D), the load increased which is due to the arrest of the crack caused by the compression of the loading pin.

The load-displacement curves showed a good reproducibility and no difference could be seen between the OLCR samples and the continuously loaded ones, except for the drops of load during the dwell.

6.3 Strain measurements

The strain distribution around the crack tip in a 4ENF sample was measured with FBG sensors which were placed one layer above or below the crack plane. The FBG sensors are sensitive to tension and compression, however, the reflection peak does not change under shear deformation. In the following subsections the results of measurements with the OLCR based method and a multiplexed sensor array with eight short FBGs are discussed.

6.3.1 OLCR based measurements

The loading of the sample was interrupted at different crack lengths to measure the strain distribution with the OLCR based method. Measurements of the local Bragg wavelength at similar crack lengths were done for fibre sensors placed above and below the crack plane and are shown in Figure 6.4. One can see that the LBW is constant before the stress field associated with the crack tip reaches the FBG. When the crack is in the FBG zone, a sudden change of the LBW is observed. This is due to the fact that the fibre sensor is very close to the centre of the beam (and thus the neutral axis) before the crack tip has passed and very close to the surface of the bending arm afterwards. For the sensor fibre placed above the crack plane (solid lines) the LBW increases by about $4nm$ and for the fibre placed below the crack plane (dotted lines) an equal decrease was measured. Note that the results from the two sensors are very similar with respect to a horizontal symmetry plane in the middle.

Several measurements were taken at two different crack lengths. As can be seen, the crack grew by about $1.5mm$ (2% of the track length) between the first and last measurement at a given crack length despite the dwell of one hour before the start of the measurements. This growth of the crack shows that some relaxation must occur at the crack tip causing further damage. Comparing the LBW curves for the two different crack lengths, one can see that they are very similar which means that the stress field around the crack tip in a 4ENF test does not depend on the crack length.

In the LBW measurements of mode I delamination the crack tip was clearly indicated by the v-shaped dip. In mode II, there was no such indication. The

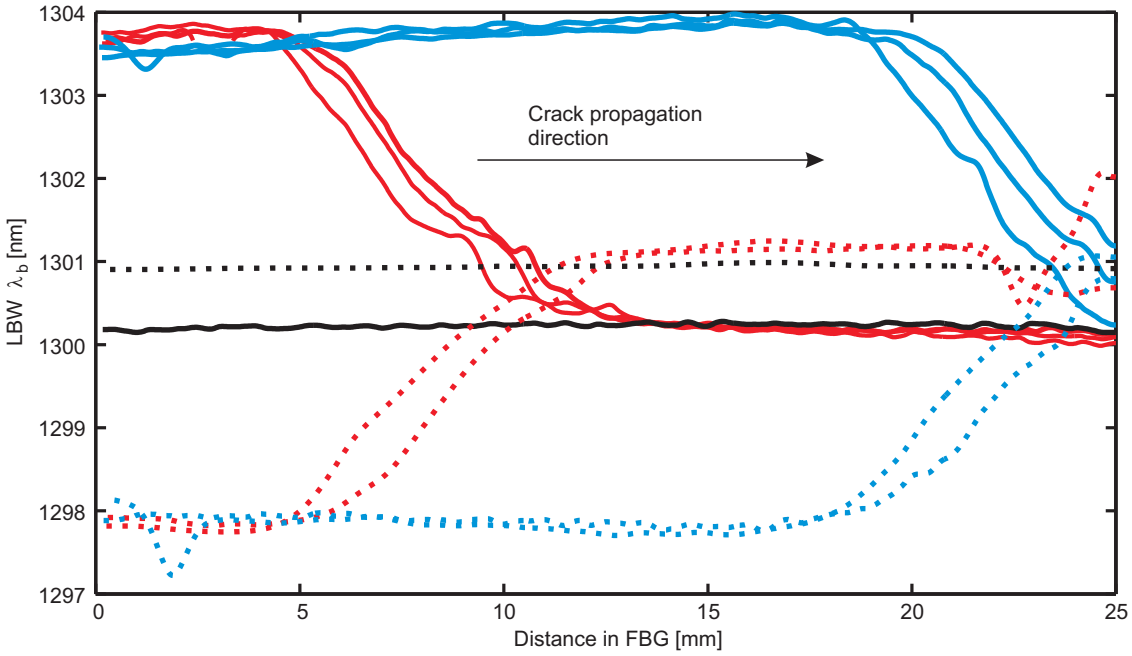

Figure 6.4: Strain distribution measured with the OLCR based method in mode II delamination at different crack lengths. The solid lines stem from a sensor fibre above the crack plane and the dashed from one below.

crack tip position was therefore assumed to be in the middle of the steep part. This assumption was supported by numerical simulations where the crack length was fixed and the mesh was refined around the crack tip with a stress singularity simulated as described in Subsection 5.4.1.

6.3.2 Multiplexed sensors

During the OLCR measurements further crack growth has been observed even after more than an hour of dwell. This shows that the need to stop the loading is a considerable limitation of this method. To allow for continuous loading, a sensor array with eight multiplexed FBGs was used to measure the strain distribution as for mode I delamination. The FBGs were constantly interrogated so that no stops were required. Figure 6.5 shows the evolution of strain for the eight sensors of a fibre that was placed below the crack plane. One can see a slight increase of strain during the first $800s$ of the test. This is due to the bending of the beam

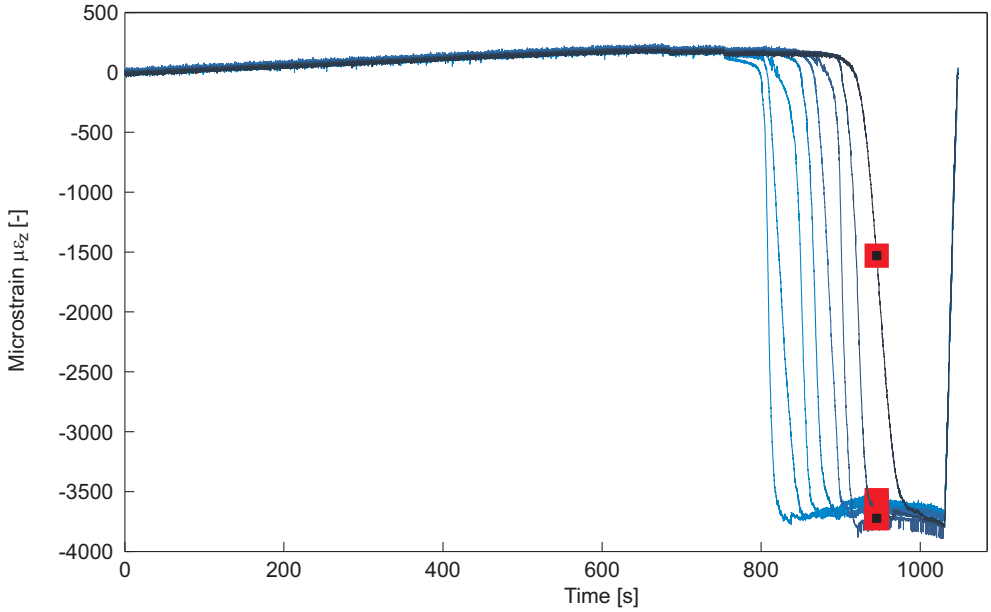

Figure 6.5: Evolution of strain during the 4ENF test. The squares indicate the strains in each of the eight sensors when the crack tip reaches the last FBG of the array.

and the slight off-centre position of the sensor fibre. When the crack tip reaches an FBG there is a sudden drop of strain. The first seven curves have very similar and almost equidistant drops which indicates a constant crack propagation speed. For the last FBG the crack was already influenced by the loading pin and the crack propagation speed was slower and thus the drop less steep.

Using the data reduction method as described in Subsection 3.2.2, the strain as a function of crack length was obtained and the eight curves were shifted to the position of the last FBG. Figure 6.6 shows the obtained strain distribution. The curves superimpose extremely well which shows that the strain distribution around the crack tip does not change during crack propagation. The loading of the sample was continued for a while when the crack tip approached the loading pin causing the load to increase which led to the small decreasing part at the end of each curve (to the left).

Compared to the results from the OLCR measurements, those obtained with the multiplexed sensor were much smoother. However, the height of the drop was the same in both cases since the bending of the beam was very similar. In the

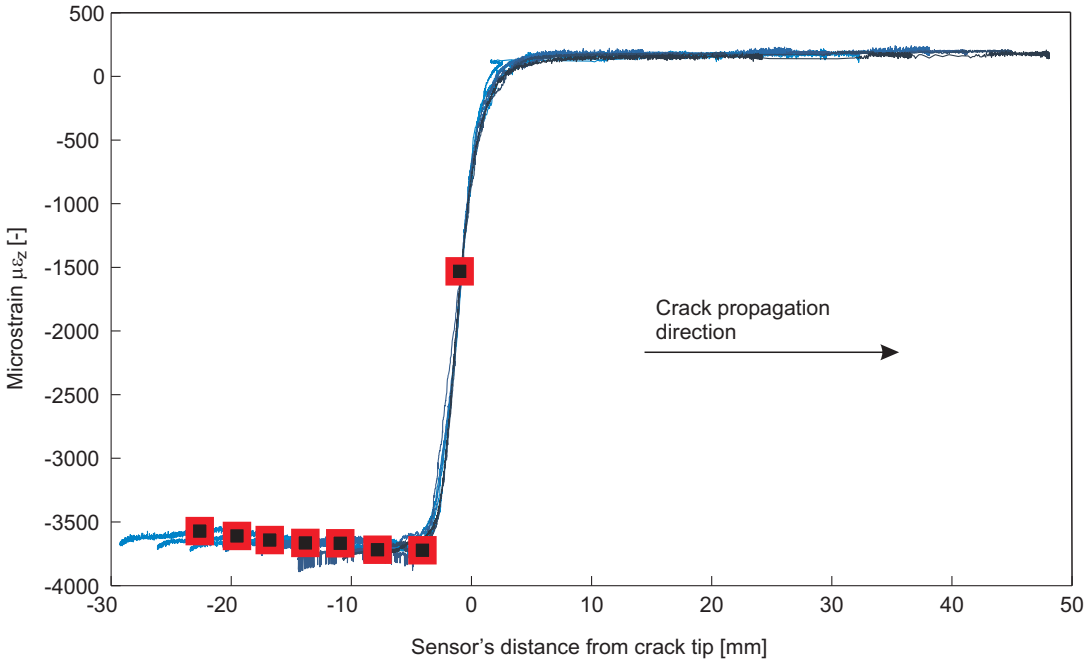

Figure 6.6: The strain distribution measured with each FBG of the array was shifted to the position of the last FBG. The squares are the same as in Figure 6.5 and mark the strains measured by the eight sensors when the crack tip is at the last FBG.

multiplexed measurements the strain distribution did not change from one sensor of the array to the other and the measurements of different crack lengths could be used to obtain a quasi-continuous curve without introducing an error.

6.4 Numerical modelling

The strain distribution measured with the multiplexed sensor was used in a numerical model of the 4ENF test to identify parameters of the delamination test. The first simulations indicated that there was very little or no fibre bridging that could be identified. Therefore, a cohesive element model was created and the cohesive properties were identified. Additionally, the friction between the crack surfaces and between the loading pins and the composite were studied with this model.

A schematic of the numerical model is shown in Figure 6.7. It consisted of two

beams each one with 8700 linear plane strain brick elements (Abaqus CPE4R) linked with a layer of 2800 cohesive elements (Abaqus COH2D4) coloured grey in the figure. From the loading pin (D) to the right hand side of the specimen, the beams were tied together without cohesive elements in between (indicated as tied surfaces). The loading pins (B), (D), and (E) were simulated as analytical surfaces.

The cohesive element had a length of $20\mu m$ and zero thickness. To obtain the zero thickness the coordinates of the nodes of the upper and lower surface were set manually to the same value. In this way the fracture surfaces were in contact to each other from the beginning of the simulation.

For the damage initiation of the cohesive law the maximum stress was used as criterion. To make sure that only shear stresses were introducing damage, the criterion for the other two directions were put to $1000MPa$. For the damage evolution an energy based linear softening was chosen. The cohesive stiffness was chosen to be $98000GPa/mm$ in the normal direction of the cohesive elements and $6000GPa/mm$ in shear. The damage initiation criterion as well as the energy of the damage were parameters in the identification.

The load was introduced by displacing point (C) which was situated $40mm$ above the sample and coupled to the loading pins (B) and (D). Hard contact was defined between the fracture surfaces to avoid interpenetration of the two arms. Additionally, a friction coefficient (penalty formulation) was defined for tangential movements allowing for a maximum of $5\mu m$ of elastic slip. Between the loading pins and the composite the same type of contact was used however, with another friction coefficient.

6.4.1 Identification

The above described numerical model with cohesive elements was used in an identification method as described in Subsection 3.3.1. The parameters which were identified were: the damage initiation value, the area under the cohesive law which corresponds to the ERR in mode II (G_{II}), and the friction coefficient between the loading pins and the composite.

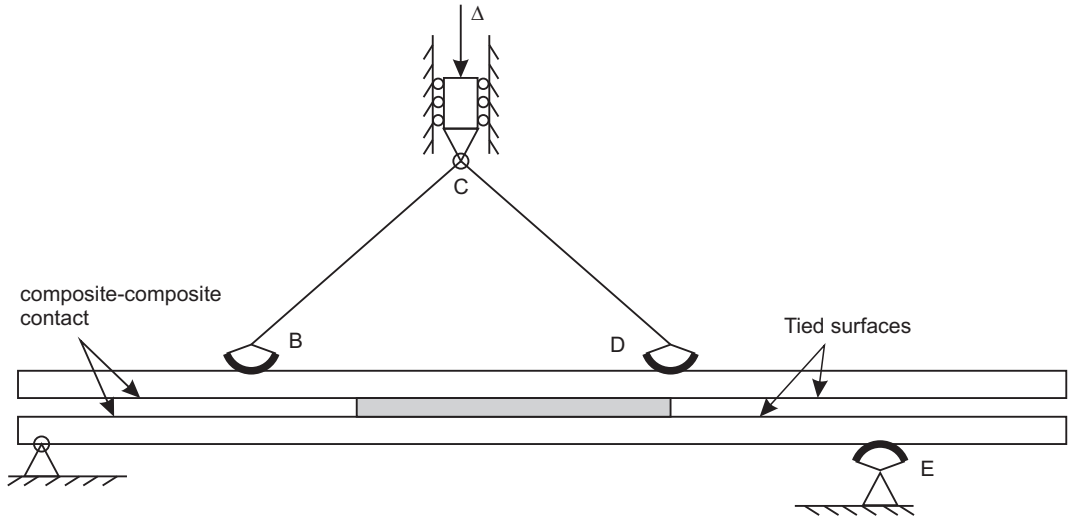

Figure 6.7: Schematic of the numerical model of the 4ENF test. The grey zone indicates the cohesive elements, their thickness was reduced to zero in the input file.

The measured strain distribution and the load from a crack length of $120mm$ were used to calculate the error vector. At this position the crack tip was right above the last FBG of the sensor array. Figure 6.8 shows the experimentally measured strain and the strain extracted from the optimised simulation. The agreement between the two curves is very good. A small difference can be seen in the region of the highest strain which could be due to a short zone of fibre bridging or a non-linear zone near the crack tip caused by matrix damage. Since the drop of strain is characteristic for the crack tip and the two curves coincide very well one can directly conclude that the crack length was correctly predicted by the numerical model.

The optimisation had a good convergence as can be seen in Figure 6.9, especially for G_{II} which was found to be 1070 J/m^2 and for the friction between the pins and the composite $\mu = 0.35$. The damage initiation criterion was identified at $\tau = 38\ MPa$, however, this parameter continued to change slightly without affecting much the residuals. This means that it can not be identified very precisely but also that it is not influencing much the simulations.

After the optimisation the load-displacement curve corresponding to point (C) of the model was extracted. Figure 6.10 shows the simulated curve together

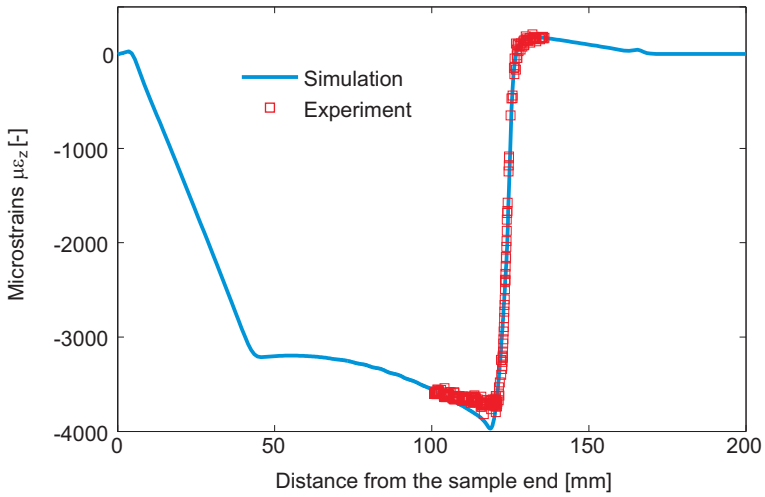

Figure 6.8: Measured and simulated strain in a 4ENF test. The measured curve stems from a multiplexed sample.

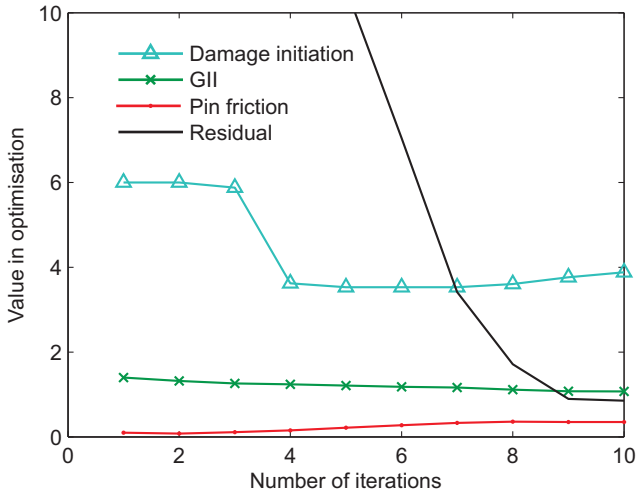

Figure 6.9: Convergence of the optimisation in mode II. Since the different values were set as close as possible to one, the displayed values are only qualitative.

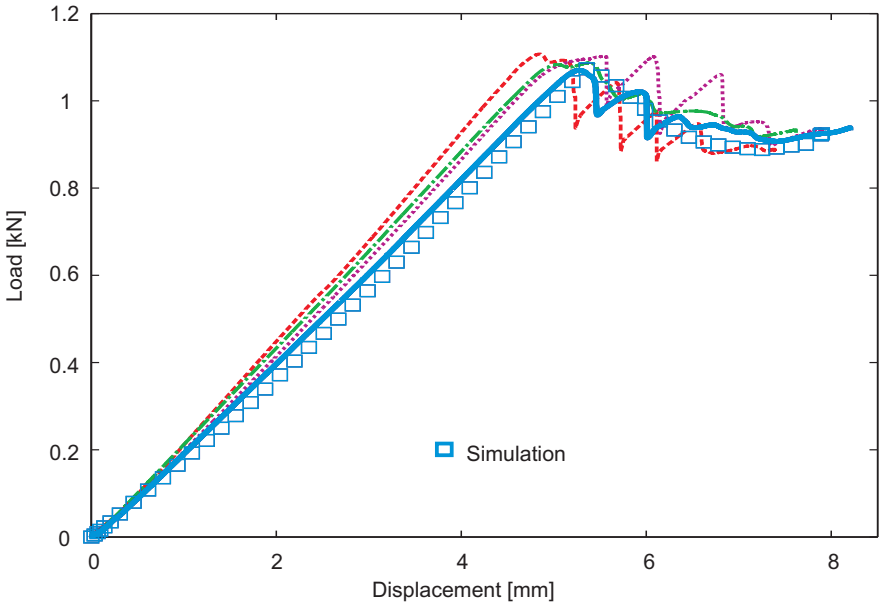

Figure 6.10: The simulation was based on the strain measurements, load, and geometry of the experiment which is reported as solid line.

with the experimental ones from Figure 6.3. The experiment from which the strain measurements were taken for the identification is shown with a solid line. One can see that both, the crack initiation and the propagation are very well reproduced by the cohesive element model.

Note that the experimental strain distribution and load which were used to calculate the error vector were measured at a single crack length. Nevertheless, the simulations, which were carried out by imposing the displacement corresponding to this crack length, were capable to predict the complete load-displacement curve. This shows that the delamination behaviour is independent of crack length.

6.4.2 Friction

One of the reasons why there is still no standard test for mode II delamination is friction. Since the crack surfaces have to be displaced in shear to each other, friction occurs in any pure mode II test. In a 4ENF test friction can occur at two places: i) between the fracture surfaces (composite-composite friction) and

ii) between the loading pins and the composite sample (pin-composite friction). The cohesive element model was used to investigate the influence of the friction on the load-displacement curve and on the strain distribution at the position of the fibre sensor.

When looking at the load-displacement curves reported in the literature for similar materials [61, 65], one can see that in some tests the load decreased after crack initiation while in other experiments the load slightly increased during crack propagation. The reason for an increasing load was suspected to be fibre bridging.

In first simulations no friction was applied and the load was found to be constant in the propagation zone. This result was expected since the expression for G_{II} derived from beam theory [61] is independent of crack length a and is given for a symmetric set-up with the lower span twice the upper span by:

$$G_{II} = \frac{P^2 3}{8B^2EI}\frac{L^2}{4} \tag{6.1}$$

where I is the moment of inertia of the undelaminated beam. From Equation 6.1 it is clear that a constant G_{II} yields a constant load in the crack propagation region. However, the experimental load-displacement curves showed a decreasing load which means that either the ERR decreased with increasing crack length or the simulation was too simplified to capture this behaviour.

In a second model tangential friction was added to both, the composite-composite contact and the pin-composite contact. With this model a decreasing load-displacement curve was obtained. Figure 6.11 shows the results for different friction coefficients of the pin-composite and the composite-composite contact. It becomes clear that the composite-composite friction has no influence on the outcome of the simulation while variations of the pin-composite friction cause important changes.

Considering the load-displacement curves in Figure 6.11(b) one can see that the identification of pin-composite friction, based on load-displacement measurements, is difficult since the curves are close to each other at large displacements (indicated with an arrow). However, while the composite-composite friction does not affect the strain distribution around the crack tip as can be seen in Figure 6.12(a), variations in the pin-composite friction can easily be detected with

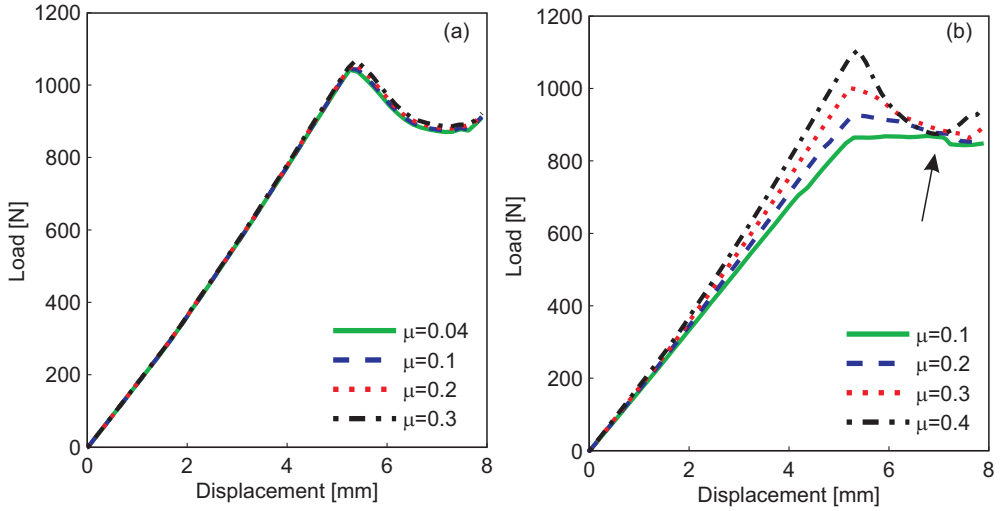

Figure 6.11: Simulated load displacement curves for different frictions.(a) the composite-composite friction is varied ($\mu = 0.35$ for the pin-composite friction) (b) the pin-composite friction is varied($\mu = 0.2$ for the composite-composite friction).

such measurements as shown in 6.12(b). This allowed to identify precisely the pin-composite friction coefficient.

The analysis showed the importance of the pin-composite friction. By its influence on the load-displacement curve, it has also a direct impact on the measured ERR. Indeed, when using the compliance calibration method to measure the ERR, G_{II} was found to decreases from $1300 J/m^2$ to $1000 J/m^2$. The optimisation with the applied friction showed, however, that G_{II} is constant at $1070 J/m^2$. For future work care must be taken to reduce the pin-composite friction and replace simple rollers by ball bearings.

Summary

In this chapter the results of the four point end notched flexure test were discussed. After an initial jump, a stable crack propagation phase was observed and enabled to measure the strain distribution around the crack tip with a long FBG using the OLCR based method and an array of eight multiplexed FBGs. The OLCR measurements showed that the strain distribution in the upper and lower

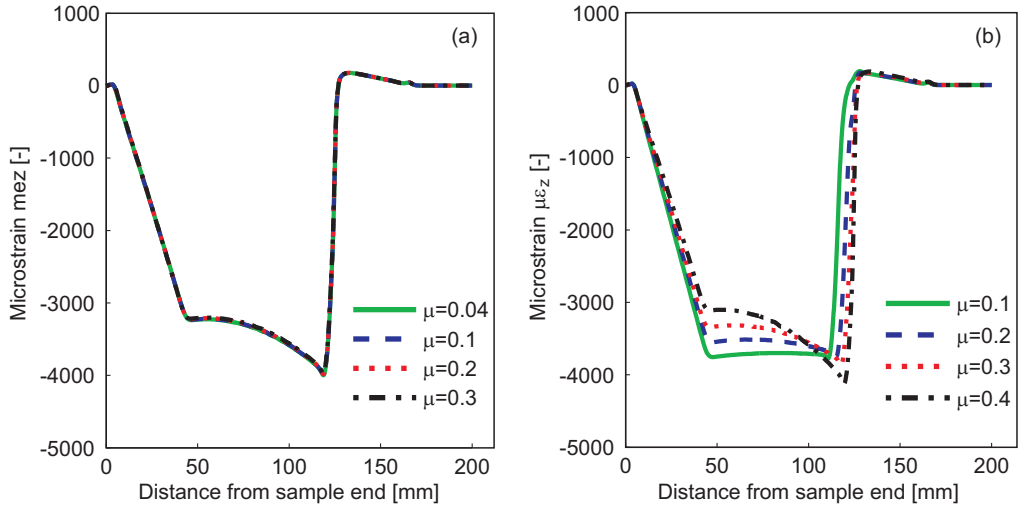

Figure 6.12: Strain distribution with different applied frictions. (a) the composite-composite friction is varied ($\mu = 0.35$ for the pin-composite friction) (b) the pin-composite friction is varied ($\mu = 0.2$ for the composite-composite friction).

part of the delamination beam are very similar and did not change with crack length.

The strain distribution measured with the multiplexed FBGs was used in an optimisation scheme to identify the properties of cohesive elements. Such an optimised model was capable to correctly predict crack initiation and propagation in a load-displacement curve. The friction between the loading pins and the composite surface was found to be of paramount importance. It was responsible for the decreasing load during crack propagation and had a strong influence on the strain distribution.

Chapter 7

Mixed mode I and II delamination

In the previous chapters delamination in pure mode I and II have been investigated. However, in many loading cases the two modes are mixed. It is therefore important to study also the delamination in mixed mode conditions. For this purpose a delamination with 50% mode II contribution was tested. As for the pure modes, the strain distribution in the vicinity of the crack tip was measured with an embedded optical sensor with multiplexed FBGs and the results were used to characterise the bridging tractions with an inverse identification method.

The set-up of the mixed mode bending test is described in the beginning of the chapter, then the test results, the measured strain distribution, and the identification of the bridging tractions are presented.

7.1 Test set-up

The mixed mode bending fixture (MMB) is designed to test samples in combined mode I and mode II delamination. Figure 7.1 shows a schematic of the set-up. By changing the length of the lever arm, c, the sample can be tested with different *mode mixtures*. The mode mixture is defined as G_{II}/G_T where G_{II} is the ERR in pure mode II and G_T is the total energy release rate as measured in the given configuration of the set-up.

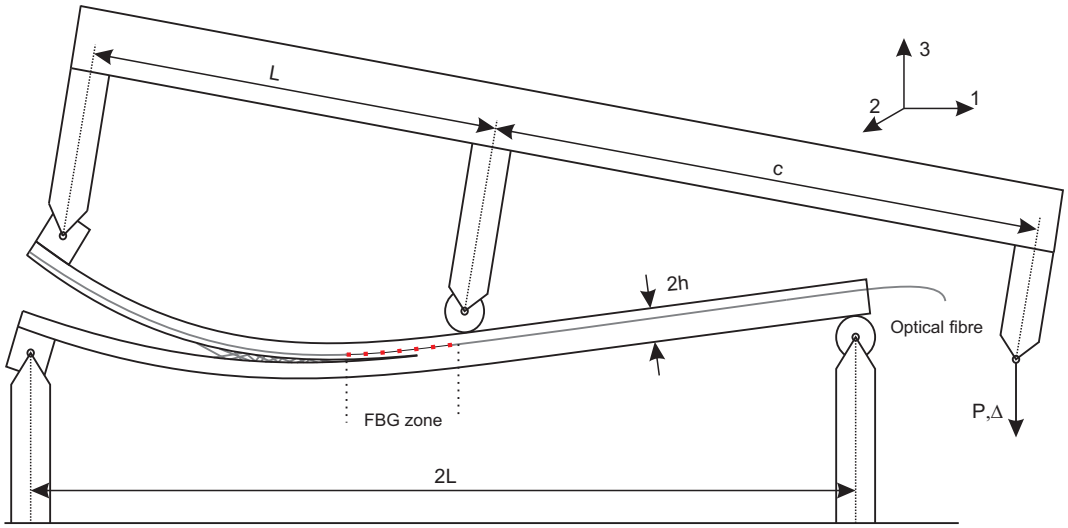

Figure 7.1: Schematic of the set-up of an MMB test. The sensor fibre was placed in the upper arm.

The length of the lever arm, c, is calculated according to:

$$c = \frac{12\beta^2 + 3\alpha + 8\beta\sqrt{3\alpha}}{36\beta^2 - 3\alpha} L \tag{7.1}$$

where

$$\alpha = \frac{1 - \frac{G_{II}}{G_T}}{\frac{G_{II}}{G_T}} \text{ and } \beta = \frac{a + \chi h}{a + 0.42\chi h}$$

and χ is a length correction which takes the rotation of the laminate at the crack tip into account and is given by:

$$\chi = \sqrt{\frac{E_1}{11G_{13}} \left\{ 2 - 2\left(\frac{\Gamma}{1+\Gamma} \right)^2 \right\}} \text{ with } \Gamma = 1.18\frac{\sqrt{E_1 E_2}}{G_{13}}$$

L is half the span of the lower two supports and E_1 and E_2 are the elastic moduli in the two principal directions and G_{13} is the out of plane shear modulus of the composite. Using Equation 7.1 a length of $c = 75.9mm$ was calculated for a 50% mode mixture.

The MMB tests were performed according to ASTM standard D6671 [53] except for L. The standard actually recommends a span of $50mm$ to keep geometric non-linear effects small. However, in this work a span of $L = 90mm$ was chosen so

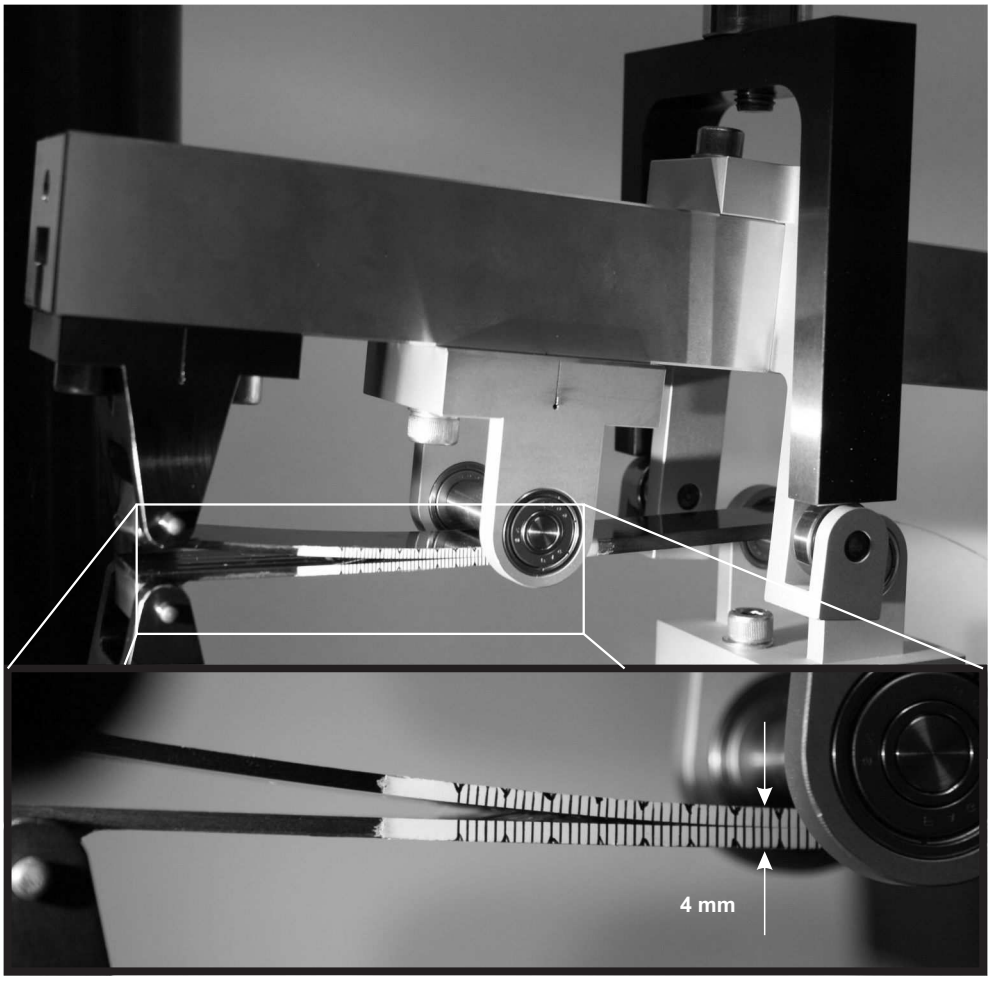

Figure 7.2: Photograph of the MMB test with a zoom on the crack tip showing some fibre bridging.

that the crack could grow sufficiently long to pass the complete FBG zone before being arrested at the upper loading pin. The multiplexed FBGs were placed in a zone from $55mm$ to $80mm$ from the left sample end. The initial crack length was $45mm$ and the tests were performed under displacement control with a loading rate of $0.008mm/s$. A photograph of the test set-up with a zoom on the crack tip is shown in Figure 7.2

7.2 Mechanical test results

Pilot tests have shown that the resin rich zone at the end of the PTFE film which was used to create the initial crack, caused a huge crack jump upon the initiation of the propagation. Clearly, this was undesired since the crack tip passed most of the zone with the embedded FBGs. To avoid the jump, the crack was propagated for approximatively $5mm$ by applying opening moments which resulted in a smooth crack initiation. The pre-cracking was done manually by applying a bending moment to the loading blocks while clamping the sample to arrest the crack at the desired length.

The load-displacement curves of three pre-cracked specimens and a specimen without pre-cracking are shown in Figure 7.3. The sample without pre-crack shows a huge drop in load which is due to the crack jump while the pre-cracked samples all have a smooth crack initiation. The visible crack initiation is marked and one can see that it occurred at similar loads. For the sample with the cross marking, initiation was observed long before the maximum load was reached while for the other two samples these points almost coincided. Since all four specimens were cut from the same composite plate they should behave similarly. The difference in load-displacement curve was therefore suspected to be due to the pre-cracking. However, inspection of the fracture surfaces did not show any difference and a straight crack front was observed in all three cases.

7.3 Energy release rate

According to the ASTM standard [53], the total ERR, G_T, which is measured during an MMB test is the sum of the ERR of mode I and mode II: $G_T = G_I + G_{II}$ where G_I and G_{II} can be calculated by expressions derived from beam theory:

$$G_I = \frac{P^2(3c - L)^2}{16BL^2IE_{1f}}(a + \chi h)^2 \tag{7.2a}$$

$$G_{II} = \frac{3P^2(c + L)^2}{64BL^2IE_{1f}}(a + 0.42\chi h)^2 \tag{7.2b}$$

where χ and c were previously defined in Section 7.1 and E_{1f} is the elastic modulus in fibre direction measured by bending. The weight of the lever can be included

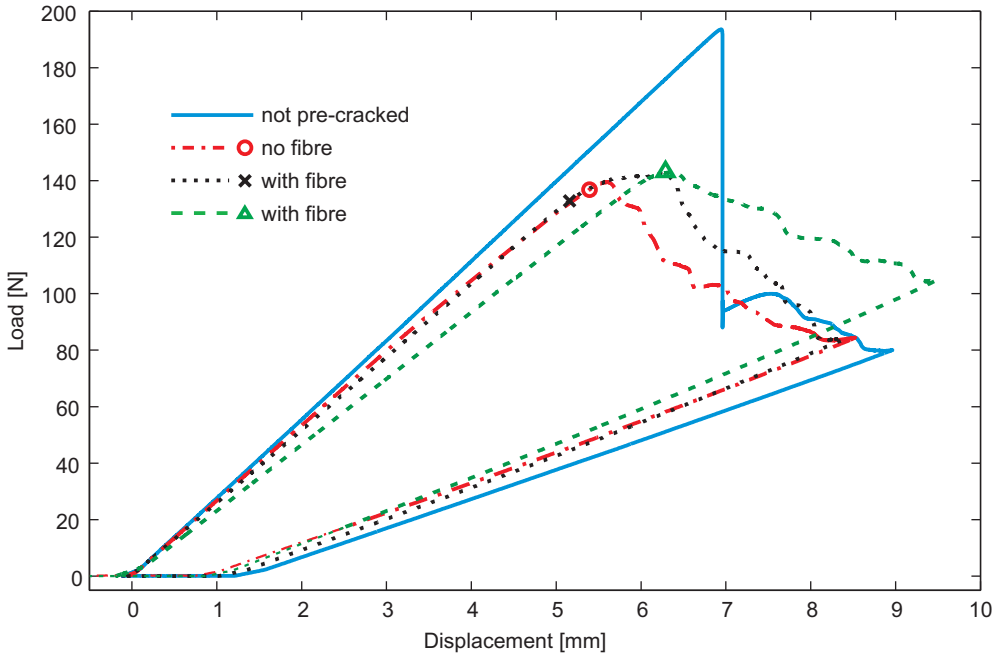

Figure 7.3: Load displacement curves from the MMB tests. The visible crack initiation is marked for the pre-cracked curves.

into the calculations by introducing the position of the centre of gravity and the load corresponding to the weight of the lever in Equations 7.2 as described in the standard. Alternatively, the weight of the lever measured at the load application point when the clamped tip is supported can be added to the measured load.

The evolution of G_T calculated with Equations 7.2 as a function of crack length is shown in Figure 7.4. For comparison, the total ERR was also calculated with the compliance calibration method (Subsection 3.4.1) using the derivative of the second order polynomial which fitted the compliance as a function of crack length.

One can see a wide spread of the initial values which is probably caused by the pre-cracking process. The initiation value seems to be at about $400 J/m^2$, however, more tests are needed to confirm this value. For the ERR obtained with Equations 7.2 the difference between the different samples further increases with growing crack length. A possible explanation for this is that the specimens are not behaving linear elastically as supposed in beam theory because of the large span and bridging fibres. In contrast, when the compliance calibration method is used,

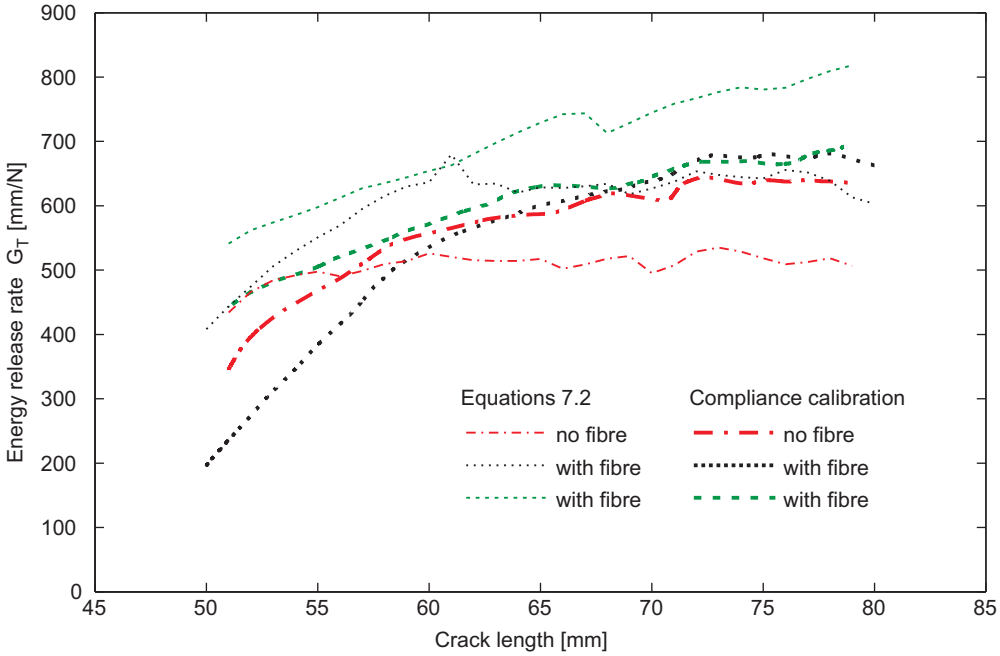

Figure 7.4: Evolution of the ERR for 50% mode mixture. The ERR was obtained with the compliance calibration method (thick lines) and using Equations 7.2 (thin lines).

the same ERR of $660 J/m^2$ is reached for all three samples after a propagation of about $10mm$. This shows that this method is better adapted to study the propagation zone. Note that the observed increase of ERR with growing crack length suggests that fibre bridging plays an important role for the crack resistance in the MMB test as it does in mode I delamination.

7.4 Strain measurements

The strain around the crack tip of the mixed mode delamination was measured with an array of eight multiplexed FBGs. Figure 7.5 shows the strain at each FBG as a function of crack length. Contrary to the strain distribution in mode I tests, there is no clear indication of the crack tip. Numerical simulations have shown that the crack tip is at around $1500\mu\varepsilon$ and in curves 3, 4, and 5 a small dip can actually be seen.

As the crack tip approaches the FBG, the strain rapidely increases since the

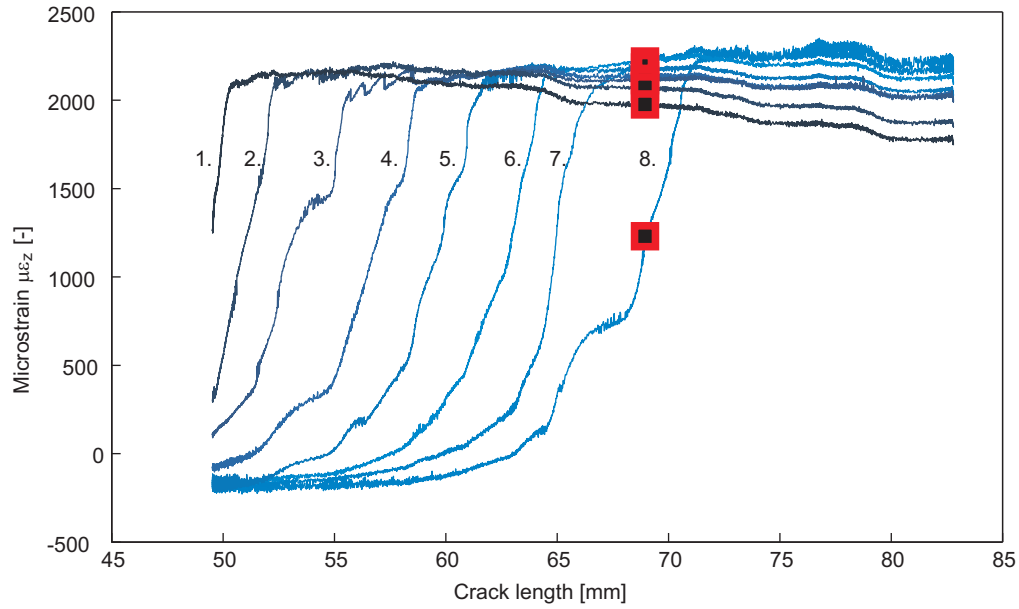

Figure 7.5: Strain versus crack length for a MMB test. The squares mark the strain measured by each FBG when the crack tip is below the last FBG of the array.

position of the fibre sensor changes from close to the neutral axis of the intact specimen to the surface of the delaminated beam. When the crack tip has passed the FBG, an abrupt change is observed and the strain is almost constant.

Following the methodology described in Subsection 3.2.2, the eight curves from Figure 7.5 were shifted to the crack length corresponding to the position of the last FBG in the array. Figure 7.6 shows the obtained strain distribution with squares marking the strain measured by the eight FBGs at the considered crack length of $69mm$. The curves superimpose very well which shows that the strain distribution does not change when the crack advances. A quasi-continuous distribution can therefore be obtained taking the data from the considered crack length and $\pm 2mm$ adjacent crack lengths. This result served later in the inverse identification to calculate the error vector.

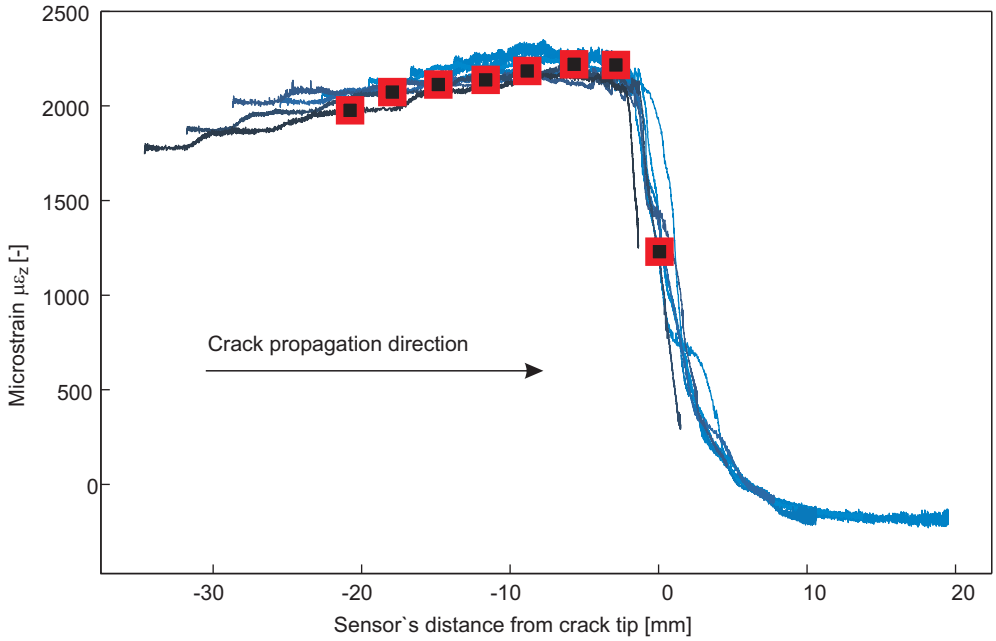

Figure 7.6: Strain distribution measured in the MMB test. The squares are the same as in Figure 7.5.

7.5 Numerical modelling

A 2D plane strain model of the MMB test was created to simulate the strain in the specimen at the position of the fibre sensor. This model consisted of several parts and was used to identify the bridging tractions. The simulated specimen was composed of an upper and lower beam which were tied together ahead of the crack tip as shown in Figure 7.7. Both beams were meshed with 7500 quadratic plane strain brick elements (Abaqus CPE8R) with a refinement at the crack tip. The $1/\sqrt{r}$ stress singularity was obtained by collapsing one edge of the neighbouring elements and shifting the mid-nodes of the adjacent edges to one quarter of the edge length.

The lever was simulated with 2000 quadratic plane strain brick elements (Abaqus CPE8R) with steel properties and a thickness of $40mm$. At point (B) a reference point was coupled to the upper beam and joined to the lever with a multipoint constraint of pin type. The same type of constraints was used to link the loading pin (C) to the lever. For the rollers at point (C) and (E) hard contact

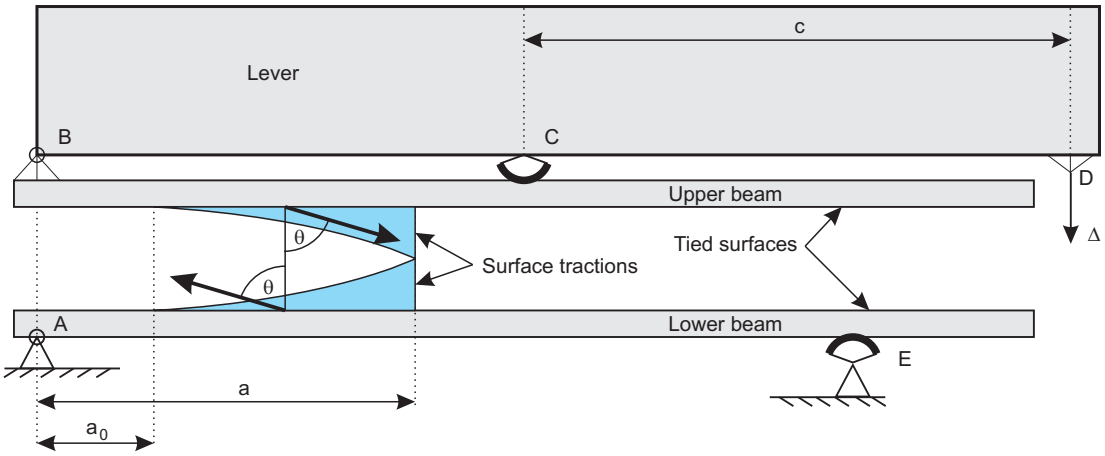

Figure 7.7: Schematic of the numerical model of the MMB test. The upper and lower beams are separated to illustrate the bridging (shaded area), in the simulation they are tied together.

was defined in the normal direction and frictionless contact in shear direction. This assumption is reasonable since contrary to the 4ENF test ball bearings were used for the pins. The sample was loaded by applying a vertical displacement at point (D) which was coupled to the lever and located at $2.5mm$ above the upper beam and at a distance c from the central pin (C).

Fibre bridging was simulated by surface tractions which were applied on both beams between the crack tip and the end of the PTFE insert at a_0. The surface tractions are indicated by arrows and a shaded area in Figure 7.7. The tractions were decreasing from a maximum at the crack tip following the same exponential distribution that was used for bridging in mode I and is given by Equation 5.3. However, the tractions were applied with an angle θ to the normal as defined in Figure 7.7 leading to bridging that opposes at the same time the opening and shear of the crack surfaces. The same surface traction distribution and angle were applied to both beams.

7.5.1 Identification of bridging

The above described model was used in an inverse identification scheme as described in Subsection 3.3.1. The following parameters of the surface traction

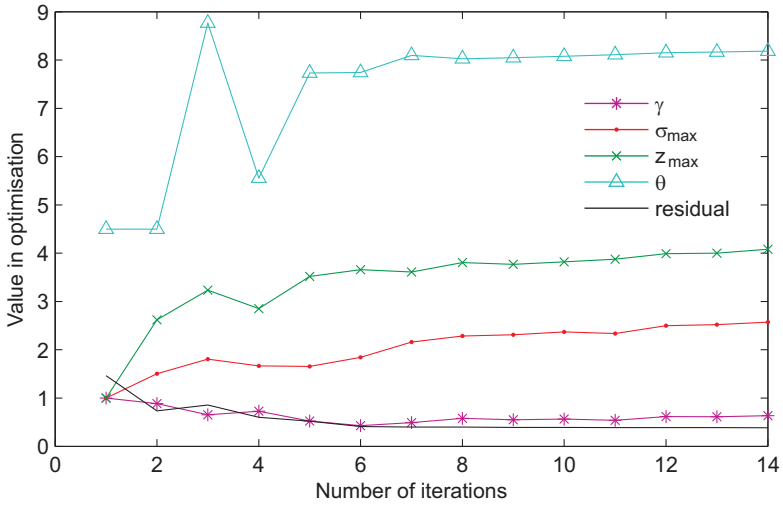

Figure 7.8: Convergence of the bridging identification in the MMB test. The parameters are reported as used in the optimisation, they are therefore only qualitative.

distribution were identified: σ_{max}, z_{max}, γ, and the angle θ defining the direction in which the tractions act. Contrary to the identification in modes I and II, the load was not used to calculate the error vector because the load extracted from the simulation did not take the weight of the lever into account and could therefore not be compared to the experimental data.

The convergence of the optimisation was very good for all parameters as can be seen in Figure 7.8. After the eighth iteration only very small changes occurred and the residual did not further decrease. The identified values were as follows: $\sigma_{max} = 2.5MPa$, $z_{max} = 41mm$, $\gamma = 0.065$, and $\theta = 81^o$. Note that the length of the bridging zone was longer than the total crack advance indicating that it was not yet fully developed within the crack increment considered. With an angle of 81^o the tractions were applied almost horizontally which means that they followed almost the direction of the reinforcing fibres in the undamaged material.

All parameters were found to be in a very similar range as the ones obtained in mode I (see Table 5.2). However, a direct comparison between distributions in the two tests is not possible because the tractions are applied in a different direction and the opening and length of the crack were different.

Figure 7.9 shows the measured quasi-continuous strain (squares) as well as

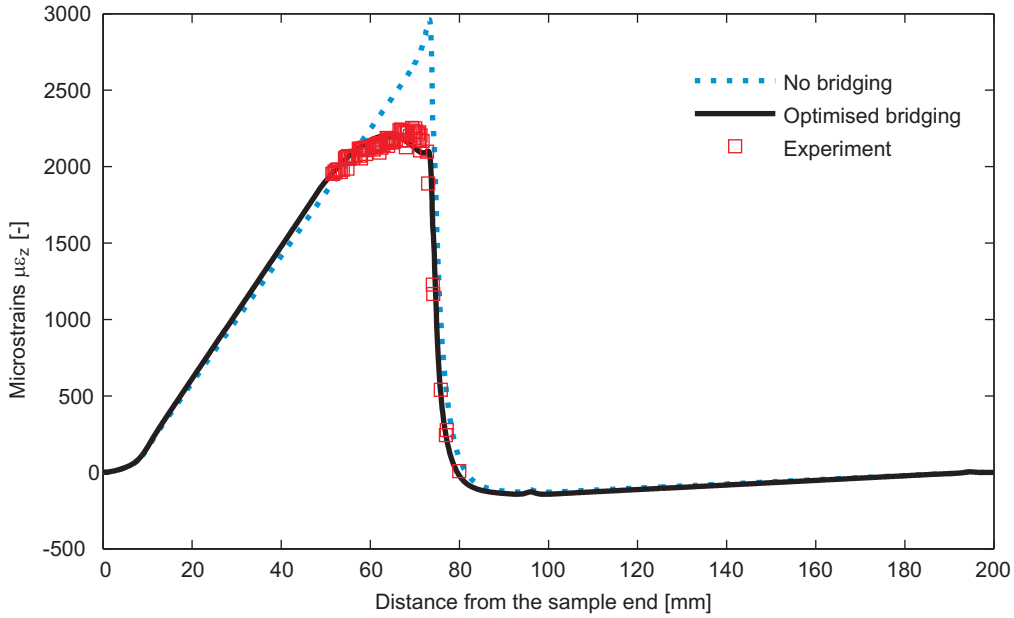

Figure 7.9: Measured and simulated longitudinal strain distribution in an MMB test. The solid and dotted lines stem from simulations.

the strain extracted from a model with optimised surface tractions (solid line). One can see a very good agreement between the measured and simulated strain. For comparison, the strain from a simulation without surface tractions is shown (dotted line). These simulations clearly illustrate the strong influence of the bridging tractions in the MMB test. They decrease the longitudinal strain close to the crack tip by one third.

Summary

In this chapter the results of mixed mode bending tests have been presented. Because of the big jump at crack initiation pre-cracking of the samples was indispensable to achieve a smooth crack propagation. However, this led to an important scatter of the initiation values of the measured ERR. This scatter almost completely disappeared after a crack propagation of about $10mm$ when the ERR was calculated with the compliance calibration method. On the basis of the results in mode I, the increase of ERR with growing crack suggests a strong

influence of fibre bridging. However, further research is required to verify this hypothesis.

The strain distribution around the crack tip was measured with a multiplexed FBG sensor and then used in an inverse identification process to characterise the fibre bridging. The bridging tractions were found to act almost horizontally (against the shear displacement) and reducing strongly the strain in the bridging zone.

Chapter 8

Conclusions

In this work delamination in mode I, mode II, and mixed mode I/II of unidirectionally aligned long carbon fibre reinforced epoxy was studied experimentally and numerically. For this, optical fibre sensors were embedded in several samples for each test set-up. Such sensors are well suited for micromechanical measurements since they are very small and can be placed close to the region of interest without affecting its behaviour. In the present case, they were placed one layer above the crack plane and the longitudinal strains around the crack tip and in the bridging zone were measured. With these measured strain distributions, bridging tractions and friction were determined using an inverse numerical identification method.

8.1 Optical fibre sensors

Even though the fibre sensors are small, their diameter is still fifteen times larger than the one of the reinforcing carbon fibres and they have to be considered as an inclusion. Therefore, the interaction between the sensor fibre and the crack was studied with a numerical simulation where the fibre was explicitly modelled assuming a perfect interface. This analysis has shown that the fibre locally influences the crack, however, this influence is very small and does not affect the delamination behaviour of the sample which was experimentally confirmed by comparing samples with and without embedded fibres. Further, a 3D model showed, that the strain in the centre of the sensor fibre was the same as found

at this position when no fibre was present which confirmed that the fibre sensors measure the correct strain.

In previous work [5] long FBG sensors were interrogated with an OLCR based method to measure the distributed strain. This method has produced good results, however, it has a few drawbacks. Namely, a very low speed which makes it necessary to interrupt the test to take a measurement. During this dwell relaxation and further crack propagation can occur. Also, the interrogator requires a very specialised equipment and is highly sensitive to vibrations.

To improve strain sensing, the multiplex capability of FBGs was exploited. Instead of a single long FBG of $25mm$ an array of eight short sensors was used where each FBG was only $1mm$ long and separated by $3mm$ from its neighbours. Since the strain was almost homogeneous over the length of such an FBG, the reflection peak was not split but simply shifted. The peak shifts of all eight FBGs were measured simultaneously with a commercially available interrogator at a rate of up to $1000Hz$. An OLCR measurement allowed to determine the precise position of each FBG and a point-wise strain distribution at any time of the test was obtained. Using the measured crack length and shifting the eight strain distributions to a common crack tip position, a quasi-continuous strain distribution resulted.

This novel method using multiplexed FBG sensors was compared to results of the OLCR based method. The results from the multiplexed method were similar but showed much less noise. The relatively high acquisition rate allowed for continuous loading of the specimen and even measurements during fatigue tests were performed successfully. The main limitation of this new method is the fact that the obtained strain is only a point-wise measurement. To obtain a quasi-continuous strain distribution around a crack, this latter has to move along the sensor array and measurements from different crack lengths have to be combined.

This work has shown that embedded FBG sensors are well suited to measure strains around delamination cracks. The introduction of multiplexed FBG sensors simplified and accelerated the measurements so that they could be performed in new loading cases like four point bending, mixed mode bending, and fatigue. The measured strains in combination with an inverse identification allowed to determine important test parameters like bridging laws and friction.

8.2 Delamination

Mode I delamination was studied using a DCB test. In these experiments no difference between the samples with and without embedded fibres was found. However, the dwell time which was necessary for the OLCR measurements led to a drop in load of about 5%. The strain distribution was first measured with long FBGs and the OLCR based method. Using an inverse identification procedure the distribution of bridging tractions along the crack surfaces was determined. Different expressions defining the shape of this distribution were compared and an exponential decrease was found to be best suited since it was at the same time simple, versatile and had a unique minimum in the optimisation.

Further DCB tests were performed with samples containing short multiplexed FBG sensors. In these experiments no dwell time was needed and the samples were continuously loaded. The measured strain was similar to the one obtained with the long FBGs showing that these two methods produce equivalent results. However, the energy release rate associated to the bridging fibres was found to be about 50% higher in the continously loaded samples which was attributed to the relaxation of bridging tractions that occured during the dwell of the OLCR samples and which was manifested by the drop of load.

The identified bridging traction distribution was used to calculate the stress intensity factor of the DCB test by applying the principle of superposition. While the external load opens the crack, the bridging tractions close the crack and decrease the SIF. When both, external load and bridging tractions were applied, the calculated total SIF was found independent of crack length. Transforming the SIF to ERR, a value of $360 J/m^2$ was obtained which was very close to the measured initiation value of the DCB test. This showed that the SIF is constant and fibre bridging accounts entirely for the observed increase with crack growth.

By combining the bridging traction distribution with the corresponding crack opening a traction separation law, the so called bridging law, was obtained. The integration of this bridging law resulted in the work needed to overcome the bridging tractions and corresponded to the part of the ERR associated to the bridging fibres. This value was found close to the difference between the ERR at initiation and at propagation and accounted for about half the total ERR. By

implementing the identified bridging law into a cohesive element model the complete load-displacement curve with correct crack initiation load and propagation behaviour could be predicted.

Samples with multiplexed FBG sensors were also tested in load controlled fatigue. As for the monotonic DCB tests, fibre bridging was observed and caused a decrease of crack speed when the bridging zone was developing. The embedded sensors allowed to measure the strain distribution and identify precisely the position of the crack tip throughout the test. The energy release rate associated to the identified bridging tractions was about 30% higher than for the monotonic loading showing that bridging is very importat in fatigue DCB tests.

The analysis of the DCB samples in terms of SIF, ERR and with cohesive elements have shown that fibre bridging accounts for the complete increase of the observed fracture resistance and the simulations have shown that the bridging law is approximatively constant throughout the test.

The 4ENF set-up was used to measure pure mode II delamination. This set-up was chosen because of the stable crack propagation. The measurements from the embedded optical sensors and subsequent inverse identification revealed the importance of friction between the loading pins and the composite. The friction between the fracture surfaces had, however, no influence on the load-displacement curve or strain distribution. Fibre bridging was not observed during this test and a constant ERR three times as high as in mode I delamination was identified with a cohesive element model.

In the mixed mode tests the measured strain distributions showed a strong influence of bridging tractions in the vicinity of the crack tip. The results of the inverse identification indicate that these tractions have a similar amplitude as in mode I and are oriented in the direction of the reinforcing fibres. The initiation ERR was found about 15% higher than in mode I while the propagation value was only marginaly higher.

Overall, the importance of fibre bridging in monotonic and fatigue DCB tests was clearly shown in this work. Calculations of SIF and ERR as well as cohesive element models confirmed that it is responsible for the entire increase of toughness observed upon crack propagation. In mixed mode bending similar values as in mode I tests were obtained for the bridging traction distribution. Although

further research is needed this is a strong indication that fibre bridging is a key parameter in this test as well. In mode II the influence of the pin-composite friction was revealed while the friction between the crack surfaces was of minor importance.

8.3 Future work

Fatigue has to be considered in almost all applications and therefore reliable tests have to be developed to measure delamination properties in fatigue. The results obtained in this work showed that fibre bridging is an important factor which influences the results of such tests. The new method with multiplexed FBG sensors has proven very useful to measure strain in fatigue tests and could be further used to gain more knowledge on the influence of fibre bridging in fatigue.

The tests with the 4ENF set-up have shown the strong influence of the pin-composite friction. Modifications should be applied to the test rig to reduce this friction. As a contribution to the development of a standard test method for pure mode II other set-ups like the end notched flexure or the end notch split test could be investigated with optical fibre sensors as well.

For the mixed mode bending test a lot of work remains to be done. The bridging tractions and their direction of action should be characterised as a function of mode mixture. Once bridging is understood the interaction of the two modes can be studied with numerical models.

Finally, the method which was proposed in this work has shown very useful for micromechanical measurements in composite structures. So far, it was only applied to UD composites and further research is needed to asses the possibility to use optical fibre sensors in cross plies as well. Despite the small diameter of the fibre sensors, a reduction is desirable since it would further decrease the intrusiveness.

Bibliography

[1] Dominick V. Rosato and Donald V. Rosato. *Plastics Engineered Product Design*. Elsevier Advanced Technology, 2003.

[2] P. Robinson and J. M. Hodgkinson. Interlaminar fracture toughness. In J. M. Hodgkinson, editor, *Mechanical testing of advanced composites*. CRC Press ; Woodhead, Boca Raton, FL, 2000.

[3] L. Sorensen, J. Botsis, T. Gmür, and J. Cugnoni. Delamination detection and characterisation of bridging tractions using long FBG optical sensors. *Composites Part A: Applied Science and Manufacturing*, 38(10):2087–2096, 2007.

[4] L. Sorensen, J. Botsis, T. Gmür, and L. Humbert. Bridging tractions in mode I delamination: Measurements and simulations. *Composites Science and Technology*, 68(12):2350–2358, 2008.

[5] L. Sorensen. *The response of embedded FBG sensors to non-uniform strains in CFRP composites during processing and delamination*. PhD thesis, École Polytechnique Fédérale de Lausanne, 2006.

[6] P. Davies, B. R. K. Blackman, and A. J. Brunner. Standard test methods for delamination resistance of composite materials: Current status. *Applied Composite Materials*, 5(6):345–364, 1998.

[7] T.E. Tay. Characterization and analysis of delamination fracture in composites: An overview of developments from 1990 to 2001. *Applied Mechanics Reviews*, 56(1):1–32, 2003.

[8] S. Sridharan. *Delamination Behaviour of Composites*. Woodhead Publishing Limited, Cambridge, 2008.

[9] S. S. Wang. Fracture mechanics for delamination problems in composite materials. *Journal of composite materials*, 17(3):210–223, 1983.

[10] V. Bolotin. Mechanics of delaminations in laminate composite structures. *Mechanics of composite materials*, 37(5-6):367–380, 2001.

[11] J. P. Davim, J. C. Rubio, and A. M. Abrao. A novel approach based on digital image analysis to evaluate the delamination factor after drilling composite laminates. *Composites Science and Technology*, 67(9):1939–1945, 2007.

[12] J. F. Mandell, D. S. Cairns, D. D. Samborsky, R. B. Morehead, and D. J. Haugen. Prediction of delamination in wind turbine blade structural details. *Journal of solar energy engineering*, 125(4):522–530, 2003.

[13] M. D. Gilchrist and N. Svensson. A fractographic analysis of delamination within multidirectional carbon/epoxy laminates. *Composites Science and Technology*, 55(2):195–207, 1995.

[14] P. Wright, X. Fu, I. Sinclair, and S. M. Spearing. Ultra high resolution computed tomography of damage in notched carbon fiber-epoxy composites. *Journal of composite materials*, 42(19):1993–2002, 2008.

[15] E. F. Rybicki and M. F. Kanninen. A finite element calculation of stress intensity factors by a modified crack closure integral. *Engineering Fracture Mechanics*, 9(4):931–938, 1977.

[16] A. Miravete and M.A. Jimenez. Application of the finite element method to prediction of onset of delamination growth. *Applied mechanics reviews*, 55(2):89–106, 2002.

[17] O. Allix, P. Ladeveze, and A. Corigliano. Damage analysis of interlaminar fracture specimens. *Composite Structures*, 31(1):61–74, 1995.

[18] Q. D. Yang and B. Cox. Cohesive models for damage evolution in laminated composites. *International Journal of Fracture*, 133(2):107–137, 2005.

[19] N. Chandra, H. Li, C. Shet, and H. Ghonem. Some issues in the application of cohesive zone models for metal-ceramic interfaces. *International Journal of Solids and Structures*, 39(10):2827–2855, 2002.

[20] G. Alfano. On the influence of the shape of the interface law on the application of cohesive-zone models. *Composites Science and Technology*, 66(6):723–730, 2006.

[21] C. T. Sun and Z. H. Jin. Modeling of composite fracture using cohesive zone and bridging models. *Composites Science and Technology*, 66(10):1297–1302, 2006.

[22] E. Zile and V. Tamuzs. Mode II delamination of a unidirectional carbon fiber/epoxy composite in four-point bend end-notched flexure tests. *Mechanics of composite materials*, 41(5):383–390, 2005.

[23] C. Balzani and W. Wagner. An interface element for the simulation of delamination in unidirectional fiber-reinforced composite laminates. *Engineering Fracture Mechanics*, 75(9):2597–2615, 2008.

[24] M. L. Falk, A. Needleman, and J.R. Rice. A critical evaluation of cohesive zone models of dynamic fracture. *Journal De Physique. IV : JP*, 11(5):Pr543–Pr550, 2001.

[25] A. Turon, J. Costa, P. P. Camanho, and C. G. Davila. Simulation of delamination in composites under high-cycle fatigue. *Composites Part A: Applied Science and Manufacturing*, 38(11):2270–2282, 2007.

[26] A. Turon, P. Camanho, and J. Costa. *Delamination in composites*. VDM, Saarbrücken, 2008.

[27] R. de Borst and J. C. Remmers. Computational modelling of delamination. *Composites Science and Technology*, 66(6):713–722, 2006.

[28] W.S. Johnson and P.D. Mangalgiri. Investigation of fiber bridging in double cantilever beam specimens. *Journal of composites technology and research*, 9(1):10–13, 1987.

[29] G. Bao and Z. Suo. Remarks on crack-bridging concepts. *Applied Mechanics Reviews*, 45(8):355–366, 1992.

[30] Z. Suo and J. W. Hutchinson. Interface crack between two elastic layers. *International journal of fracture*, 43(1):1–18, 1990.

[31] S. M. Spearing and A. G. Evans. The role of fiber bridging in the delamination resistance of fiber-reinforced composites. *Acta Metallurgica et Materialia*, 40(9):2191–2199, 1992.

[32] D. S. Dugdale. Yielding of steel sheets containing slits. *Journal of the Mechanics and Physics of Solids*, 8(2):100–104, 1960.

[33] V. C. Li, C. Chan, and C. K. Y. Leung. Experimental determination of the tension-softening relations for cementitious composites. *Cement and Concrete Research*, 17(3):441–452, 1987.

[34] B.F. Sorensen and T. K. Jacobsen. Large-scale bridging in composites: R-curves and bridging laws. *Composites Part A: Applied Science and Manufacturing*, 29(11):1443–1451, 1998.

[35] S. P. Fernberg and L. A. Berglund. Bridging law and toughness characterisation of CSM and SMC composites. *Composites Science and Technology*, 61(16):2445–2454, 2001.

[36] V. Tamuzs, S. Tarasovs, and U. Vilks. Progressive delamination and fiber bridging modeling in double cantilever beam composite specimens. *Engineering Fracture Mechanics*, 68(5):513–525, 2001.

[37] B. N. Cox and N. Sridhar. A traction law for inclined fiber tows bridging mixed-mode cracks. *Mechanics of Advanced Materials and Structures*, 9(4):299–331, 2002.

[38] J. A. Nairn. Analytical and numerical modeling of R curves for cracks with bridging zones. *International journal of fracture*, 155(2):167–181, 2009.

[39] L. C. Dickinson, G. L. Farley, and M. K. Hinders. Translaminar reinforced composites: A review. *Journal of composites technology and research*, 21(1):3–15, 1999.

[40] D. R. Cartié, M. Troulis, and I. K. Partridge. Delamination of z-pinned carbon fibre reinforced laminates. *Composites Science and Technology*, 66(6):855–861, 2006.

[41] A. P. Mouritz. Review of z-pinned composite laminates. *Composites Part A: Applied Science and Manufacturing*, 38(12):2383–2397, 2007.

[42] P. Robinson and S. Das. Mode I DCB testing of composite laminates reinforced with z-direction pins: a simple model for the investigation of data reduction strategies. *Engineering Fracture Mechanics*, 71(3):345–364, 2004.

[43] A. J. Brunner, B. R. K. Blackman, and P. Davies. A status report on delamination resistance testing of polymer-matrix composites. *Engineering Fracture Mechanics*, 75(9):2779–2794, 2008.

[44] ASTM-Standard-D5528. Standard test method for mode I interlaminar fracture toughness of unidirectional fiber-reinforced polymer matrix composites, 2001.

[45] ISO-15024. Fibre-reinforced plastic composites - determination of mode I interlaminar fracture toughness, G_{IC}, for unidirectionally reinforced materials, 2001.

[46] R. Foote and V. Buchwald. An exact solution for the stress intensity factor for a double cantilever beam. *International journal of fracture*, 29(3):125–134, 1985.

[47] R. Massabò, L. Brandinelli, and B. N. Cox. Mode I weight functions for an orthotropic double cantilever beam. *International Journal of Engineering Science*, 41(13-14):1497–1518, 2003.

[48] A. J. Brunner, N. Murphy, and G. Pinter. Development of a standardized procedure for the characterization of interlaminar delamination propagation in advanced composites under fatigue mode I loading conditions. *Engineering Fracture Mechanics*, 76(18):2678–2689, 2009.

[49] S. Feih, J. Wei, P. Kingshott, and B. F. Sorensen. The influence of fibre sizing on the strength and fracture toughness of glass fibre composites. In *7th International Conference on Deformation and Fracture of Composites (DEF-7)*, pages 245–255, Sheffield, ENGLAND, 2003. Elsevier Sci Ltd.

[50] C. Yan, K. Xiao, L. Ye, and Y. W. Mai. Numerical and experimental studies on the fracture behavior of rubber-toughened epoxy in bulk specimen and laminated composites. *Journal of materials science*, 37(5):921–927, 2002.

[51] A. B. Pereira and A. B. de Morais. Mode I interlaminar fracture of carbon/epoxy multidirectional laminates. *Composites Science and Technology*, 64(13-14):2261–2270, 2004.

[52] F. Ozdil and L. A. Carlsson. Beam analysis of angle-ply laminate dcb specimens. *Composites Science and Technology*, 59(2):305–315, 1999.

[53] ASTM-Standard-D6671. Standard test method for mixed mode I - mode II interlaminar fracture toughness of unidiretional fiber-reinforced polymer matrix composites, 2006.

[54] N. Baral, P. Davies, C. Baley, and B. Bigourdan. Delamination behaviour of very high modulus carbon/epoxy marine composites. *Composites Science and Technology*, 68(3-4):995–1007, 2008.

[55] M. Kenane and M. L. Benzeggagh. Mixed-mode delamination fracture toughness of unidirectional glass/epoxy composites under fatigue loading. *Composites Science and Technology*, 57(5):597–605, 1997.

[56] Y. Meziere, L. Michel, and D. Carronnier. Mixed-mode delamination failure criteria in carbon fibre/composite under quasi-static and cyclic loading. In J. G. Williams and A. Pavan, editors, *European Structural Integrity Society*, volume Volume 27, pages 97–110. Elsevier, 2000.

[57] F. Ozdil and L. A. Carlsson. Beam analysis of angle-ply laminate mixed-mode bending specimens. *Composites Science and Technology*, 59(6):937–945, 1999.

[58] A. B. Pereira and A. B. de Morais. Mixed mode I + II interlaminar fracture of carbon/epoxy laminates. *Composites Part A: Applied Science and Manufacturing*, 39(2):322–333, 2008.

[59] M. König, R. Krüger, K. Kussmaul, M. Von Alberti, and M. Gädke. Characterizing static and fatigue interlaminar fracture behavior of a first generation graphite/epoxy composite. *ASTM Special Technical Publication*, 1242:60–81, 1997.

[60] L. A. Carlsson. On the analysis and design of the end notched flexure (ENF) specimen for mode II testing. *Journal of composite materials*, 20(6):594–604, 1986.

[61] R. H. Martin and B. D. Davidson. Mode II fracture toughness evaluation using four point bend, end notched flexure test. *Plastics, rubber, and composites processing and applications*, 28(8):401–406, 1999.

[62] T.K. O'Brien. *Composite interlaminar shear fracture toughness, G_IIC: Shear measurement or sheer myth?*, volume 7 of *Composite Materials: Fatigue and Fracture, ASTM STP 1330*. 1998.

[63] X. Sun and B. D. Davidson. A direct energy balance approach for determining energy release rates in three and four point bend end notched flexure tests. *International journal of fracture*, 135(1-4):51–72, 2005.

[64] B. R. K. Blackman, A.J. Brunner, and J.G. Williams. Mode II fracture testing of composites: a new look at an old problem. *Engineering fracture mechanics*, 73(16):2443–2455, 2006.

[65] C. Schuecker and B. D. Davidson. Evaluation of the accuracy of the four-point bend end-notched flexure test for mode II delamination toughness determination. *Composites Science and Technology*, 60(11):2137–2146, 2000.

[66] B. D. Davidson, X. Sun, and A. J. Vinciquerra. Influences of friction, geometric nonlinearities, and fixture compliance on experimentally observed toughnesses from three and four-point bend end-notched flexure tests. *Journal of composite materials*, 41(10):1177–1196, 2007.

[67] R.D.S.G. Campilho, M. F. S. F. De Moura, A.M.G. Pinto, and D.A. Ramantani. Interlaminar fracture characterization of a carbon-epoxy composite in pure mode II. *Materials Science Forum*, 636-637:1518–1524, 2010.

[68] K. Hill, Y. Fujii, D. Johnson, and B. Kawasaki. Photosensitivity in optical fiber waveguides: Application to reflection filter fabrication. *Applied physics letters*, 32(10):647–649, 1978.

[69] G. Meltz, W. Morey, and W. Glenn. Formation of Bragg gratings in optical fibers by a transverse holographic method. *Optics letters*, 14(15):823–825, 1989.

[70] S. S. J. Roberts and R. Davidson. Cure and fabrication monitoring of composite materials with fibre-optic sensors. *Composites Science and Technology*, 49(3):265–276, 1993.

[71] V. Antonucci, M. Giordano, A. Cusano, J. Nasser, and L. Nicolais. Real time monitoring of cure and gelification of a thermoset matrix. *Composites Science and Technology*, 66(16):3273–3280, 2006.

[72] M. Mulle, R. Zitoune, F. Collombet, P. Olivier, and Y. H. Grunevald. Thermal expansion of carbon-epoxy laminates measured with embedded FBGs - comparison with other experimental techniques and numerical simulation. *Composites Part A: Applied Science and Manufacturing*, 38(5):1414–1424, 2007.

[73] J. Frieden, J. Cugnoni, J. Botsis, T. Gmür, and D. Coric. High-speed internal strain measurements in composite structures under dynamic load using embedded FBG sensors. *Composite Structures*, 92(8):1905–1912, 2010.

[74] I. McKenzie and N. Karafolas. Fiber optic sensing in space structures: The experience of the european space agency. In M. Voet, editor, *17th International Conference on Optical Fibre Sensors*, volume 5855. Proceedings of SPIE, 2005.

[75] A. D. Kersey, M. A. Davis, H. J. Patrick, M. LeBlanc, K. P. Koo, C. G. Askins, M. A. Putnam, and E. J. Friebele. Fiber grating sensors. *Journal of lightwave technology*, 15(8):1442–1462, 1997.

[76] R. Kashyap. *Fiber Bragg Gratings*. Academic Press, 1999.

[77] R.M. Measures. *Structural Monitoring with fiber optic technology*. Academic Press, 2001.

[78] E. N. Barton, S. L. Ogin, A. M. Thorne, G. T. Reed, and B. H. Le Page. Interaction between optical fibre sensors and matrix cracks in cross-ply GRP laminates–part 1: passive optical fibres. *Composites Science and Technology*, 61(13):1863–1869, 2001.

[79] J. M. A. Silva, J. A. M. Ferreira, and T. C. Devezas. Fatigue damage of carbon-epoxy laminates with embedded optical fibres. *Materials Science and Technology; MST*, 19(6):809–814, 2003.

[80] J. M. A. Silva, T. C. Devezas, A. P. Silva, and J. A. M. Ferreira. Mechanical characterization of composites with embedded optical fibers. *Journal of composite materials*, 39(14):1261–1281, 2005.

[81] K. S. C. Kuang and W.J. Cantwell. Use of conventional optical fibers and fiber Bragg gratings for damage detection in advanced composite structures: A review. *Applied mechanics reviews*, 56(5):493–513, 2003.

[82] N. Takeda, Y. Okabe, J. Kuwahara, S. Kojima, and T. Ogisu. Development of smart composite structures with small-diameter fiber Bragg grating sensors for damage detection: Quantitative evaluation of delamination length in CFRP laminates using lamb wave sensing. *Composites Science and Technology*, 65(15-16):2575–2587, 2005.

[83] S. Minakuchi, Y. Okabe, and N. Takeda. Real-time detection of debonding between honeycomb core and facesheet using a small-diameter FBG sensor embedded in adhesive layer. *The journal of sandwich structures and materials*, 9(1):9–33, 2007.

[84] D. Coric, M. Lai, J. Botsis, A. Luo, and H.G. Limberger. Distributed strain measurements using fiber Bragg gratings in small-diameter optical fiber and low-coherence reflectometry. *Optics express*, 18(25):26484–26491, 2010.

[85] M. LeBlanc. Study of interfacial interaction of an optical fibre embedded in a host material by in situ measurement of fibre end displacement - part 1. theory. *Smart materials and structures*, 14(4):637–646, 2005.

[86] M. J. LeBlanc. Study of interfacial interaction of an optical fibre embedded in a host material by in situ measurement of fibre end displacement - part 2. experiments. *Smart materials and structures*, 14(4):647–657, 2005.

[87] L. G. Melin, K. Levin, S. Nilsson, S. J. P. Palmer, and P. Rae. A study of the displacement field around embedded fibre optic sensors. *Composites Part A: Applied Science and Manufacturing*, 30(11):1267–1275, 1999.

[88] K. Peters, P. Pattis, J. Botsis, and P. Giaccari. Experimental verification of response of embedded optical fiber Bragg grating sensors in non-homogeneous strain fields. *Optics and Lasers in Engineering*, 33(2):107–119, 2000.

[89] H. Y. Ling, K.T. Lau, L. Cheng, and W. Jin. Utilization of embedded optical fibre sensors for delamination characterization in composite laminates using a static strain method. *Smart materials and structures*, 14(6):1377–1386, 2005.

[90] H. Y. Ling, K.T. Lau, L. Cheng, and K.W. Chow. Embedded fibre Bragg grating sensors for non-uniform strain sensing in composite structures. *Measurement science and technology*, 16(12):2415–2424, 2005.

[91] H. Y. Ling, K.T. Lau, L. Cheng, and Z. Su. Mode II fracture behaviour monitoring for composite laminates using embedded fibre Bragg grating sensors. *Composite Structures*, 76(1-2):88–93, 2006.

[92] Y. Okabe, R. Tsuji, and N. Takeda. Application of chirped fiber bragg grating sensors for identification of crack locations in composites. *Composites. Part A, Applied science and manufacturing*, 35(1):59–65, 2004.

[93] S. Yashiro, T. Okabe, and N. Takeda. Damage identification in a holed CFRP laminate using a chirped fiber Bragg grating sensor. *Composites Science and Technology*, 67(2):286–295, 2007.

[94] J. Palaniappan, H. Wang, S. L. Ogin, A. M. Thorne, G. T. Reed, A.D. Crocombe, Y. Rech, and S. C. Tjin. Changes in the reflected spectra of embedded chirped fibre Bragg gratings used to monitor disbonding in bonded composite joints. *Composites science and technology*, 67(13):2847–2853, 2007.

[95] P. Lambelet, P.Y. Fonjallaz, H.G. Limberger, R.P. Salath, Z. Zimmer, and H.H. Hilgen. Bragg grating characterization by optical low-coherence reflectometry. *IEEE Photon. Technol. Lett.*, 5(5):565–567, 1993.

[96] Ph. Giaccari, H.G. Limberger, and R.P. Salathe. Local coupling-coefficient characterization in fiber Bragg gratings. *Optics letters*, 28(8):598–600, 2003.

[97] J. Botsis, L. Humbert, F. Colpo, and P. Giaccari. Embedded fiber bragg grating sensor for internal strain measurements in polymeric materials. *Optics and Lasers in Engineering*, 43(3-5):491–510, 2005.

[98] D. Karalekas, J. Cugnoni, and J. Botsis. Monitoring of process induced strains in a single fibre composite using FBG sensor: A methodological study. *Composites Part A: Applied Science and Manufacturing*, 39(7):1118–1127, 2008.

[99] L. Humbert, F. Colpo, and J. Botsis. An axisymmetric stress analysis in a single fibre composite of finite length under a thermal expansion mismatch. *European Journal of Mechanics - A/Solids*, 28(2):257–265, 2009.

[100] F. Colpo, L. Humbert, and J. Botsis. An experimental numerical study of the response of a long fibre Bragg grating sensor near a crack tip. *Smart materials and structures*, 16(4):1423–1432, 2007.

[101] M. Studer, K. Peters, and J. Botsis. Method for determination of crack bridging parameters using long optical fiber Bragg grating sensors. *Composites. Part B, Engineering*, 34(4):347–359, 2003.

[102] W. Morey, J. R. Dunphy, and G. Meltz. Multiplexing fiber Bragg grating sensors. *Fiber and Integrated Optics*, 10(4):351 – 360, 1991.

[103] T. S. P. Austin, M. M. Singh, P. J. Gregson, and P. M. Powell. Characterisation of fatigue crack growth and related damage mechanisms in FRP-metal hybrid laminates. *Composites Science and Technology*, 68(6):1399–1412, 2008.

[104] P. Giaccari, G. Dunkel, L. Humbert, J. Botsis, H.G. Limberger, and R.P. Salathé. On a direct determination of non-uniform internal strain fields using fibre Bragg gratings. *Smart materials and structures*, 14(1):127–136, 2005.

[105] R. Feced, M. N. Zervas, and M. A. Muriel. Efficient inverse scattering algorithm for the design of nonuniform fiber bragg gratings. *IEEE Journal of Quantum Electronics*, 35(8):1105–1115, 1999.

[106] J. Skaar, L. Wang, and T. Erdogan. On the synthesis of fiber bragg gratings by layer peeling. *IEEE Journal of Quantum Electronics*, 37(2):165–173, 2001.

[107] J. Cugnoni, J. Botsis, and J. Janczak-Rusch. Size and constraining effects in lead-free solder joints. *Advanced engineering materials*, 8(3):184–191, 2006.

[108] A.A. Griffith. The phenomena of rupture and flow in solids. *Philosophical Transactions of the Royal Society*, A221:163–198, 1920.

[109] M.F. Kanninen and C.H. Popelar. *Advanced Fracture Mechanics*. Oxford University Press, 1985.

[110] T.L. Anderson. *Fracture Mechanics*. CRC Press, 1995.

[111] P. Davies and M.L. Benzeggagh. Interlaminar mode-I fracture testing. In K. Friedrich, editor, *Application of Fracture Mechanics to Composite Materials*, volume 6, pages 81–112. Elsevier Science Publishers B.V., Amsterdam, 1989.

[112] C. F. Shih, B. Moran, and T. Nakamura. Energy release rate along a three-dimensional crack front in a thermally stressed body. *International journal of fracture*, 30(2):79–102, 1986.

[113] H. Tada, P.C. Paris, and G.R. Irwin. *The Stress Analysis of Cracks Handbook*. ASME Press, New York, 3 edition, 2000.

Curriculum Vitæ

Samuel Stutz
born on the 31st of August 1982, in Bern, Switzerland
Origin: Sarmenstorf, Switzerland

Education:

2007–2011:	École Polytechnique Fédérale de Lausanne, Switzerland *PhD thesis at the doctoral school of Materials Science*
2002–2007:	École Polytechnique Fédérale de Lausanne, Switzerland *MSc in Materials Science and Engineering*
2005–2006:	Royal Institute of Technology (KTH) Stockholm, Sweden *Exchange year*
1998–2001:	Mathematisch- Naturwissenschaftliches Gymnasium Kirchenfeld, Bern, Switzerland

Working experience:

2006:	Internship at EMPA in Thun, Switzerland *Linking of diamonds with Si-based polymer precursors.*
2004:	Internship at EuropTec in Oftringen, Switzerland *Application of an easy to clean layer on anti-reflex coated glass.*
2007–2010:	École Polytechnique Fédérale de Lausanne, Switzerland *Teaching assistant for the courses* *"Mécanique des structures" (Prof. J. Botsis)* *"Techniques de mesure" (Dr. T.-V. Truong)*

Publications:

2009: J. Rion, S. Stutz, Y. Leterrier, J.-A.E. Månson. Influence of process pressure on local facesheet instability for ultra-light sandwich structures. *Journal of Sandwich Structures and Materials*,11(4):293-311,2009.

2011: S. Stutz, J. Cugnoni, J. Botsis. Studies of mode I delamination in monotonic and fatigue loading using FBG wavelength multiplexing and numerical analysis. *Composites Science and Technology*, 71(4):443-449,2011.

2011: S. Stutz, J. Cugnoni, J. Botsis. Crack - fiber sensor interaction and characterization of the bridging tractions in mode I delamination. *Engineering Fracture Mechanics*, Article in Press.

Presentations:

2008: S. Stutz, J. Botsis, J. Cugnoni, D. Coric. Characterization of Mode I delamination in a CFRP composite using long embedded FBG sensors and inverse identification methods. 5^{th} ESIS TC4 Conference, 7-11 September 2008, Les Diablerets, Switzerland.

2009: S. Stutz, J. Botsis, J. Cugnoni, D. Coric. Investigations into the contribution of bridging tractions to Mode I delamination. DFC10 Conference, 15-17 April 2009, Sheffield, UK.

2010: S. Stutz, J. Cugnoni, J. Botsis, D. Coric. Delamination monitoring and calculation of bridging tractions in mode-I fracture in a polymer composite. ICSS 9 Conference, 14-16 June 2010, at CalTech, USA.

2011: S. Stutz, J. Cugnoni, J. Botsis. Experimental and numerical characterization of modes I & II delamination in unidirectional composites. 5^{th} CompTest Conference, 14-16 February 2011, Lausanne, Switzerland.